Springer Theses
Recognizing Outstanding Ph.D. Research

Jilei Liu

Graphene-Based Composites for Electrochemical Energy Storage

Springer

Springer Theses

Recognizing Outstanding Ph.D. Research

Aims and Scope

The series "Springer Theses" brings together a selection of the very best Ph.D. theses from around the world and across the physical sciences. Nominated and endorsed by two recognized specialists, each published volume has been selected for its scientific excellence and the high impact of its contents for the pertinent field of research. For greater accessibility to non-specialists, the published versions include an extended introduction, as well as a foreword by the student's supervisor explaining the special relevance of the work for the field. As a whole, the series will provide a valuable resource both for newcomers to the research fields described, and for other scientists seeking detailed background information on special questions. Finally, it provides an accredited documentation of the valuable contributions made by today's younger generation of scientists.

Theses are accepted into the series by invited nomination only and must fulfill all of the following criteria

- They must be written in good English.
- The topic should fall within the confines of Chemistry, Physics, Earth Sciences, Engineering and related interdisciplinary fields such as Materials, Nanoscience, Chemical Engineering, Complex Systems and Biophysics.
- The work reported in the thesis must represent a significant scientific advance.
- If the thesis includes previously published material, permission to reproduce this must be gained from the respective copyright holder.
- They must have been examined and passed during the 12 months prior to nomination.
- Each thesis should include a foreword by the supervisor outlining the significance of its content.
- The theses should have a clearly defined structure including an introduction accessible to scientists not expert in that particular field.

More information about this series at http://www.springer.com/series/8790

Jilei Liu

Graphene-Based Composites for Electrochemical Energy Storage

Doctoral Thesis accepted by
the Nanyang Technological University, Singapore

Springer

Author
Dr. Jilei Liu
Division of Physics and Applied Physics,
School of Physical and Mathematical
Sciences
Nanyang Technological University
Singapore
Singapore

Supervisor
Prof. Zexiang Shen
Nanyang Technological University
Singapore
Singapore

ISSN 2190-5053 ISSN 2190-5061 (electronic)
Springer Theses
ISBN 978-981-10-3387-2 ISBN 978-981-10-3388-9 (eBook)
DOI 10.1007/978-981-10-3388-9

Library of Congress Control Number: 2016960286

Printed on acid-free paper

This Springer imprint is published by Springer Nature
The registered company is Springer Nature Singapore Pte Ltd.
The registered company address is: 152 Beach Road, #22-06/08 Gateway East, Singapore 189721, Singapore

Supervisor's Foreword

Achieving secure, clean, and sustainable energy production, storage, and consumption are, perhaps, the greatest technical and social challenges that the world are facing. The key achievement is not only to explore renewable and sustainable energy sources, but also, perhaps even more importantly, to store energy efficiently and deliver on demand. The realization of high-performance electrochemical energy storage devices is no doubt strongly dependent on the achievements of multidisciplinary sciences, including materials sciences, chemical sciences, and physical sciences. Graphene, a single atomic layer of sp^2-bonded carbon atoms, has attracted worldwide interest because of its intrinsic difference from other forms of carbon allotropes. Graphene is particularly suitable for the implementation in electrochemical applications due to its remarkable electrical conductivity, large specific surface area, unique heterogeneous electron transfer and charge carrier rates, and good electrochemical stability.

In this thesis, Dr. Jilei Liu focuses on the synthesis and characterization of various carbon allotropes (e.g., graphene oxide/graphene, graphene foam (GF), and GF/carbon nanotubes (CNTs) hybrids), and their composites for electrochemical energy storage. This thesis is broad sweeping in its scope spanning from materials synthesis to electrochemical analysis to state-of-the-art electrochemical energy storage devices. Major improvements in graphene preparation, electrochemical characterization, and flexible energy storage device design have been obtained: (1) a simple, green and cost-effective electrochemical exfoliation method has been designed for synthesizing high-quality graphene in gram-scale, paving the way for commercial applications of graphene; (2) Three-dimensional graphene foam (GF)/carbon nanotubes (CNTs) hybrid films with good electric and mechanical properties were prepared, opening up new ideas for applications of graphene, especially in flexible energy storage devices; (3) Flexible energy storage devices such as asymmetric supercapacitors and aqueous alkaline nickel/iron batteries have been designed based on GF/CNTs hybrid films. Benefiting from the ultra-light and thin features of the GF/CNTs current collectors, these fabricated cells display high

gravimetric/volumetric energy density/power density and good cycling performance, demonstrating practical significance.

This is exquisite and creative work. The unique experimental procedures and methods, the systematic electrochemical analysis, as well as the creative flexible energy storage device design in this thesis may provide valuable reference for researchers in the field of carbon-based electrochemical energy storage.

Singapore
May 2016

Prof. Zexiang Shen

Parts of this thesis have been published in the following journal articles:

1. **A Flexible Alkaline Rechargeable Ni/Fe Battery Based on Graphene Foam/Carbon Nanotubes Hybrid Film**. Jilei Liu, Minghua Chen, Lili Zhang, Jian Jiang, Yizhong Huang, Jianyi Lin, Hongjin Fan, Zexiang Shen. *Nano Letters* **2014**, 14(12), 7180–7187. Chapter 5, Copyright 2014, Reprinted with permission from American Chemical Society.

2. **High-performance flexible asymmetric supercapacitors based on a new graphene foam/carbon nanotube hybrid film**. Jilei Liu, Lili Zhang, Haobin Wu, Jianyi Lin, Zexiang Shen, Xiongwen Lou. *Energy & Environmental Sciences* **2014**, 7 (11), 3709–3719. Chapter 4, Copyright 2014, Reprinted with permission from The Royal Society of Chemistry.

3. **Three-Dimensional Graphene Foam Supported Fe_3O_4 Lithium Battery Anodes with Long Cycle Life and High Rate Capability**. Jingshan Luo†, Jilei Liu†, Zhiyuan Zeng, Chi Fan Ng, Lingjie Ma, Hua Zhang, Jianyi Lin, Zexiang Shen, Hongjin Fan. *Nano Letters* **2013**, 13 (12), 6136–6143. (†equal contribution) Chapter 3, Copyright 2013, Reprinted with permission from American Chemical Society.

4. **Improved synthesis of graphene flakes from the multiple electrochemical exfoliation of graphite rod**. Jilei Liu, Chee Kok Poh, Da Zhan, Linfei Lai, San Hua Lim, Liang Wang, Xiaoxu Liu, Nanda Gopal Sahoo, Changming Li, Zexiang Shen, Jianyi Lin. *Nano Energy* **2013**, 2 (3), 377–386. Chapter 2, Copyright 2013, Reprinted with permission from Elsevier.

5. **A green approach to the synthesis of high-quality graphene oxide flakes via electrochemical exfoliation of pencil core**. Jilei Liu, Huanping Yang, Saw Giek Zhen, Chee Kok Poh, Alok Chaurasia, Jingshan Luo, Xiangyang Wu, Edwin Kok Lee Yeow, Nanda Gopal Sahoo, Jianyi Lin, Zexiang Shen. *RSC Advances* **2013**, 3 (29), 11745–11750. Chapter 2, Copyright 2013, Reprinted with permission from The Royal Society of Chemistry.

Acknowledgements

My Ph.D. journey, albeit a long one, has been a very fulfilling and rewarding experience. Throughout this whole experience, I have encountered multiple challenges, but thankfully I have also learned from each challenge to be better. This has been a wonderful journey, and I am lucky to have this opportunity.

I would like to express my deepest gratitude to my supervisor Prof. Zexiang Shen for taking me under his wing and for his care, guidance, and support throughout my whole graduate career. His vision, patience, and determination have greatly helped me on this journey and would no doubt serve as valuable life lessons in the future.

I would also like to send my heartfelt gratitude to Prof. Lin Jianyi for his selflessness, patience, and trust he placed in me. His invaluable guidance, unwavering support, and constant encouragement have enabled me to excel in my Ph.D. journey.

I am also very thankful to have the opportunity to work under Prof. (David) Lou Xiongwen and his group who has been as close as family to me. His assistance and guidance have been the pillars of strength for me throughout the period of my studies.

I would also like to express my appreciation to all my group members who have accompanied me on this journey for the past few years. These wonderful people are Yan Jiaxu, Zhan Da, Jiang Liyong, Hu Hailong, Lai Linfei, Yang Huanping, Li Baosheng, Wang Jin, Yin Tingting, Liao Mingyi, Sun Linfeng, Chao Dongliang, Cai Xiaoyi, Wang Huanhuan, Chen Zhen, and Xia Juan.

In addition, I would also like to thank my colleagues Dr. Chen Luwei, Dr. Poh Chee Kok, Dr. Zhang Lili, Dr. Lim San Hua, and Ms. Wang Zhan in Institute of Chemical and Engineering Sciences (ICES, Singapore) for their kindness and help.

Last but not least, and most importantly, I would give my special thanks to my loved ones: my wonderful parents, wife, and younger brother. Words are not sufficient to express my love and appreciation. Thank you for allowing me to pursue my dream, and for constantly supporting and encouraging me when I'm faced with obstacles. Completion of this Ph.D. journey marks the end of a chapter, but opens another in my life. I am looking forward to sharing this new phase of my life with you.

Contents

Chapter 1
Introduction and Literature Background

1.1 Energy Demands and Challenges

Energy is no doubt the engine that promotes human civilization and development. Achieving secure, clean and sustainable energy production, storage, and consumption are, perhaps, the greatest technical and social challenges that the world are facing [1–6]. Generally, energy sources could be divided into two categories based on their intrinsic nature: non-renewable sources and renewable sources. Non-renewable energies include fossil fuels, nature gas, oil and coal, are available in limited quantities on the earth and could not be re-generated within a short span of time. Renewable energies are energies that are inexhaustible, and could be generated repeatedly when required, such as solar, wind, geothermal, tide and biomass. It is projected by the U.S. Energy Information Administration that the world energy consumption will grow from 524 quadrillion British thermal units (Btu) in 2010 to 820 quadrillion Btu in 2040, a 56 percent increase between 2010 and 2040 (reference case) [7].

With rapidly growing energy demands and concerns over energy security and environmental pollution, it is highly desirable to explore renewable and sustainable energy sources. It is anticipated by Russia International Energy Agency that the share of renewable energies in primary energy consumption will rise from 13% in 2011 to 18% in 2035, resulting from rapidly increasing demand for modern renewable society to produce heat, generate power, and make transport fuels [8].

Wind power and solar photovoltaics (PV) are the world's fastest-growing renewable energy. Wind and solar would account for about 19% of global installed power capacity, and reach almost 35% of that of the European Union in 2035 according to the New Policies Scenario [8]. However, unlike dispatchable power generation technologies (fossil fuel-fired, geothermal, hydropower with reservoir and bio-energy), which may be ramped up or down to match demand, the output from wind power and solar PV is only intermittently available and is strongly dependent on the availability of the sources including the time, weather, season and

J. Liu, *Graphene-Based Composites for Electrochemical Energy Storage*,
Springer Theses, DOI 10.1007/978-981-10-3388-9_1

location, while the demands and consumption of electric energy are relatively constant [8]. Wind power and solar PV are also characterized as variable renewable energies because of their typical properties, such as variability, uncertainty, modularity, low operation cost and non-synchronous generation. Although quite attractive, the variable nature of many renewable sources present great challenge for energy storage and transmission. The key achievement lies in exploring renewable and sustainable energy sources, particularly, storing energy efficiently, and delivering on demand. Consequently, large-scale stationary energy storage systems (ESSs) connected to renewable power plants have become key enablers of improving power reliability and quality as well as taking full advantages of high penetration of renewable energy sources [6, 9, 10]. To be highly efficient, energy storage technologies are required to be adapted for various applications types. EESs that are available for large-scale applications by far could be categorized into four types: mechanical, chemical, electrical and electrochemical [6, 9, 11–13]. Although mechanical energy storage via pumped hydroelectricity is dominating current energy storage, electrochemical energy storage in terms of electrochemical capacitors and batteries have by far found their wide applications in powering portable electronics and electrification of the transportation sector because of their desirable characteristics such as high round-trip efficiency, controllable power and energy, long cycle life, environmental-friendly feature and low costs [6, 9, 11]. However, there are several challenges that rooted primarily in materials and technologies for coupling electrochemical energy storage with renewable energy sources such as wind and solar for powering the electric grid. The realization of high performance electrochemical energy storage devices is strongly dependent on the achievements of multidisciplinary sciences, including materials sciences, chemical sciences and physical sciences etc. [6, 9, 14].

1.2 Electrochemical Energy Storage Systems

1.2.1 Electrochemical Capacitors (ECs)

Since the first patent released by General Electric on 1957 [15], electrochemical capacitors (ECs) have attracted considerable attentions due to their promising applications in various areas including power storage and supply, power quality and backup applications etc. [16]. Since ECs have high power capability, efficiency and long life span [16–18] (Fig. 1.1). ECs are energy storage devices that are capable of storing and releasing electric charge in a faster way than electrochemical cells/batteries [17]. Based on different work mechanisms, ECs are classified into two categories: (i) electrochemical double layer capacitors (EDLCs) and (ii) pseudocapacitors [16–20]. The so-called EDLCs are based on electrostatic charge separation at the electrochemical interface between electrode and electrolyte, creating two electrostatic capacitors connected in series. Pseudocapacitors are based on

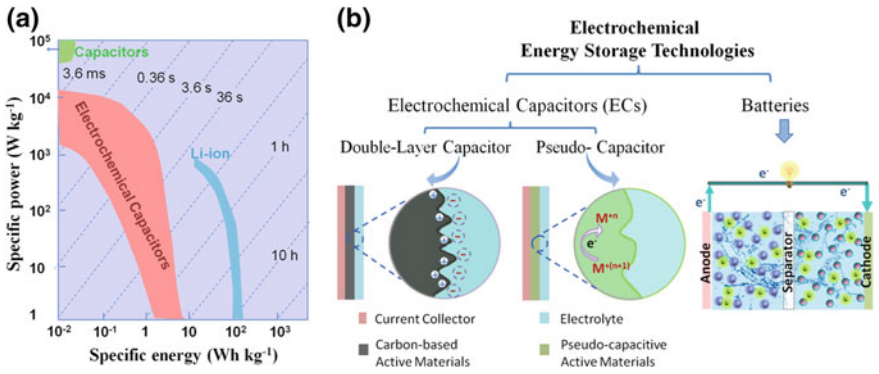

Fig. 1.1 **a** Ragone Plot and **b** Fundamental mechanisms of different energy storage technologies, include double-layer capacitor, pseudocapacitor and batteries

faradaic pseudocapacitance, that associated with electrosorption or surface/near-surface electrochemical redox processes involving in pseudocapacitive materials such as transition metal oxides and conducting polymers [14, 18, 19, 21].

1.2.1.1 Thermodynamic Principles of Electrochemical Capacitors (ECs)

Double Layer Capacitance. Different from traditional electrostatic capacitors, EDLCs store and release energy at the interface between electrolyte and electrode, where two capacitors are formed resulting from the reversible adsorption of solvated ions at the electrode surface, and connected in series by electrolyte [19, 21]. This type of charge storage is electrostatic, potential dependent, physicochemical nature of the electrode surface dependent, and no redox reactions are involved [14, 18, 19, 21]. The current during charge storage/release process is essentially a displacement current resulting from the rearrangement of charges in a Helmoholtz double layer. Therefore, the process is no-faradaic and physical in nature and the response to potential changes is rapid without diffusion limitations [20, 22]. Thus, EDLCs deliver energy very fast and have high power capability (Fig. 1.1a). However, the energy stored in EDLCs is generally lower than that of pseudocapacitors and batteries because the charge stored in EDL capacitors is confined to the surface (Fig. 1.1b). The EDL capacitance could be described as [14, 16, 17, 19, 21, 23]:

$$C_{dl} = \frac{Q}{V} = \frac{\varepsilon_r \varepsilon_o A}{d} \tag{1.1}$$

where C_{dl} is the double layer capacitance (F) of a single electrode, Q is the total charge transferred at potential V, ε_r is electrolyte dielectric constant, ε_o is the vacuum dielectric constant, d is the charge separation distance, and A is electrode surface area.

Considering C is a constant for double layer capacitors, another equation could be derived from (1.1):

$$I = \frac{dQ}{dt} = \frac{d(C_{dl}V)}{dt} = C_{dl}\frac{dV}{dt} + V\frac{dC_{dl}}{dt} = C_{dl}\frac{dV}{dt} \tag{1.2}$$

where I is the response current, t is the charge time.

If the applied voltage V varies with time t in a linear way, i.e. $V = V_0 + vt$ (V_0 is the initial voltage; v is the sweep rate (V/s)), the relationship could be given as:

$$I = C_{dl}v \tag{1.3}$$

It is found from Eq. (1.3) that the current responses linearly with the sweep rate. This feature translates into a well-defined rectangular current (I)-voltage (V) plot or cyclic voltammogram (CV) curve at different sweep rates (Fig. 1.2a). On the other hand, if a constant current is applied to charge or discharge the capacitor, voltage will increase (charging) or decrease (discharging) with a constant rate as predicted by Eq. (1.3). Thus, a triangular charge/discharge curve is expected (Fig. 1.2b).

The energy stored in such a capacitor is given by [14, 16, 17, 19, 21, 25]:

$$E = \int_0^Q V(q)dQ = \int_0^Q \frac{Q}{C}dQ = \frac{1}{2}\frac{Q^2}{C} = \frac{1}{2}CV^2 \tag{1.4}$$

$$Q = \int_0^{\Delta t} Idt = \int_0^q dq \tag{1.5}$$

where V is nominal voltage (volts) and q is the state of charge.

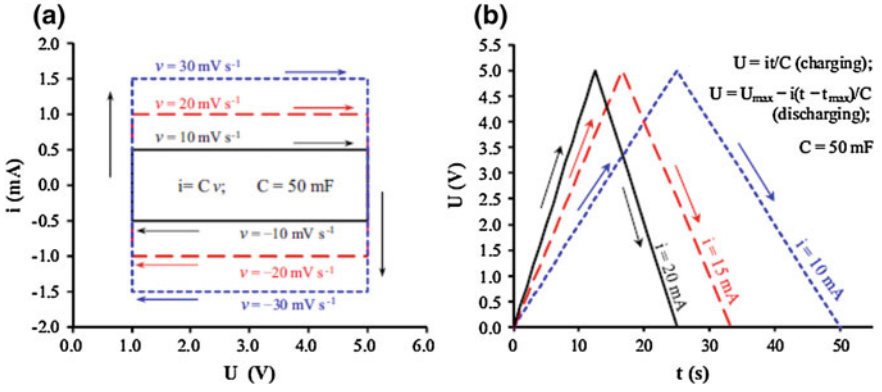

Fig. 1.2 **a** Cyclic Volammogram (CV) curves at different sweep rates, and **b** Galvanostatic Charge/Discharge curves at various currents for a 50 mF capacitor [24]. Reprinted with the permission from Elsevier, Copyright 2013

The power is thus described by the equation:

$$P = \frac{E}{t} = \frac{1}{2}\frac{CV^2}{t} \tag{1.6}$$

Pseudocapacitive Capacitance. Pseudocapacitive processes are, ideally, two-dimensional (2D) or quasi-two-dimensional. The pseudocapactive energy storage is based on fast and reversible faradaic redox process in which a monolayer or quasi-monolayer of electrochemical reactive species could be electrosorbed/electrodesorbed with charge transfer [18, 19, 26, 27]. The charge-discharge mechanism involves the transfer of charges between the surface or near surface of the electrode and the electrolyte but without any bulk phase transformation (Fig. 1.1b). The state of charge/discharge (q) is a function of the electrode potential with the extent of faradaic charge/discharge (Q) passed [19]. The change of charge (Q) with respect to the potential gives rise to the derivative, dQ/dV, corresponds to pseudocapacitance ($C_\emptyset$) [18]. Pseudocapacitance is faradaic in nature, which is different from the EDL capacitance that is associated with the potential-dependent accumulation of electrostatic charge [18, 19]. Pseudocapacitive processes also differ from the ideal Nernstian processes involved in a battery-type materials where faradaic reactions occur at a constant potential [28].

$$C_\emptyset \sim \frac{dQ}{dV} \tag{1.7}$$

There are several faradaic processes that can result in pseudocapacitance according to Conway [18, 19]: (i) under-potential deposition (UPD) (two-dimensional, 2D), (ii) surface redox system, and (iii) intercalation system (quasi-2D) (Fig. 1.3).

Under-potential Deposition. The deposition of metal ions on a different metal surface to form an adsorbed monolayer, which may occur at a potential less negative than their equilibrium potential for the reduction of this metal ion, is called under-potential deposition (UPD) [29, 30]. A well-known case of UPD is the deposition of Pb on Au, where Pb can deposit onto Au more easily that it deposit onto itself due to stronger Pb–Au interaction than the Pb–Pb interaction in the crystal lattice of pure Pb metal [26, 27, 30]. However, UPD is not limited only to metal deposition, but my also include other adsorbed layer, e.g., H from H_3O^+ or H_2O deposit on Pt [27, 29, 31, 32].

Surface Redox System. Redox processes take place when electroactive species are electrochemically adsorbed onto the surface or near surface of the electrode materials with a concomitant faradaic charge transfer. Redox systems exhibiting pseudocapacitance include the electrochemical oxidization/reduction of transition metal oxides (e.g., ruthenium oxide, manganeses oxide) and electrochemical generation of electrically conducting polymer (ECP) (e.g., polyaniline, polypyrrole, and poly-3,4-ethylene dioxythiophene) [14, 18, 21, 33]. The transitional metal oxides (MO_2, M = Ru or Mn) can be oxidized and reduced reversibly through

electrochemical protonation (H^+) or alkali metal cations (C^+=Na^+, K^+,…) intercalation, as described below [34, 35]:

$$MO_2 + H^+ + e^- - \leftrightarrow MOOH \tag{1.8}$$

or

$$MO_2 + C^+ + e^- - \leftrightarrow MOOC \tag{1.9}$$

The charge transfer process during charging and discharging does not lead to chemical transformation, but only forms a reversible functionalized molecular layer on the electrode surface. The potential of the electrode is associates with the coverage of the layer and hence dependent on the charges state. This feature is fundamentally different from redox reactions involved in battery-type electrodes, where phase change occurs at a constant potential.

Electrically conducting polymers (ECPs) can storage and release charges through redox processes in the π-conjugated polymer chains during electrochemical doping/un-doping processes, as shown below [36–38]:

$$[ECP] + nX^- \leftrightarrow [(ECP)^{n+} nX^-] + ne^- \tag{1.10}$$

During oxidization (p-doping) process, the anionic species X^- from the electrolyte are inserted into the polymer backbone. They are released back into the electrolyte upon reduction process. Similar to a battery-type reaction, the insertion/de-insertion of counter ions takes place in the bulk of the electrode, enabling high values of specific capacitance, but also giving rise to the relatively poor cycling performance resulting from volumetric changes of conducting polymers [39]. Hence, the addition of a moderate amount of carbon allotropes (e.g., carbon black, CNTs or graphene) to improve the mechanical properties of the electrodes is extremely important [33, 40, 41].

Intercalation Pseudocapacitance. Intercalation pseudocapacitance arises when the intercalation sorption of electroactive species take place quasi-two-dimensionally accompanied with faradaic charge transfer and without crystallographic phase change. Intercalation systems in pseudocapacitors include the intercalation of Li^+ into hosts such as TiS_2, MoS_2, and V_6O_{13} or the intercalation of H into Pd and Pd-Ag alloys [14, 19, 26, 27]. More recently, MXenes (of the formula $M_{n+1}X_nT_x$, where M is a transitional metal, X is C and/or N, and T_x denotes surface functionalization), are emerging as unique host materials for intercalation pseudocapacitor [42, 43]. Various ions such as Li^+, Na^+, K^+, NH_4^+, and Al^{3+} ions are found to be intercalated into MXenes layers with high volumetric pseudocapacitance [42, 43]. The intercalation/de-intercalation processes, as shown in Eq. (1.11) for two-dimensional titanium carbide ($Ti_3C_2T_x$), accompany with changes in the Ti oxidation state during cycling, ensuring high values of volumetric capacitance [44].

$$Ti_3C_2O_x(OH)_yF_{2-x-y} + \delta e^- + \delta H^+ \leftrightarrow Ti_3C_2O_{x-\delta}(OH)_{y+\delta}F_{2-x-y} \quad (1.11)$$

Although these three mechanisms take place based on different faradaic process and in different types of electrode materials, they exhibit similar thermodynamic feature, i.e., logarithmic relationship between electrode potential and the extent of charge/discharge [14, 19, 45] (Fig. 1.3):

$$E = E^0 + \frac{RT}{nF}\ln\frac{X}{1-X} \quad (1.12)$$

where E is the electrode potential (V), R is the ideal gas constant (8.314 J $mol^{-1}K^{-1}$), T is the temperature (K), n is the number of electrons, F is the Faraday constant (96,485 C mol^{-1}), and X is the occupancy fraction of surface or layer lattice.

If the electrochemical sorption of electroactive species follows an electrochemical Lagmuir isotherm [27, 32]:

$$\frac{X}{1-X} = k \cdot \exp\left(\frac{VF}{RT}\right) \quad (1.13)$$

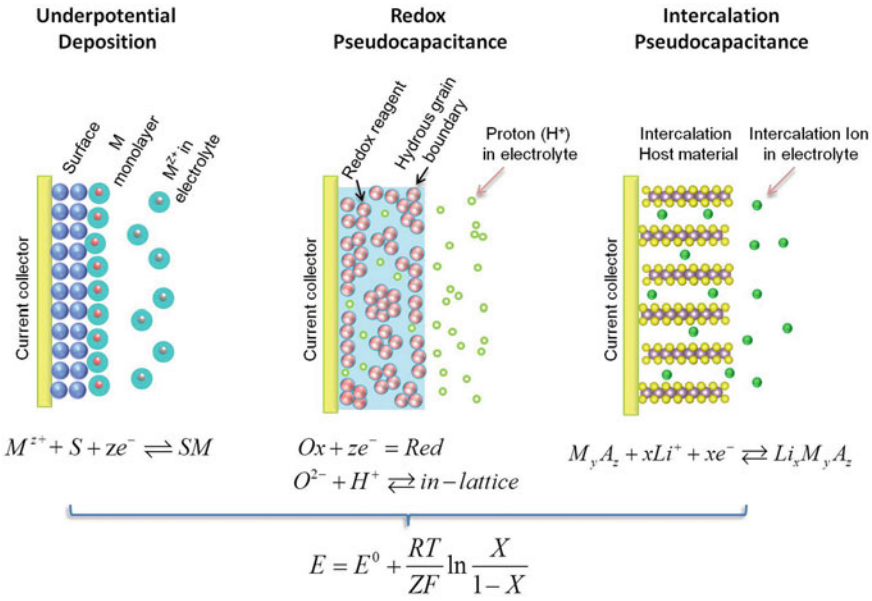

Fig. 1.3 Different faradaic processes that give rise to pseudocapacitance. *Note* X is two-dimensional site occupancy fraction for UPD, $[O_X]/([O_X] + [Red])$ for redox systems and occupancy fraction of layer lattice for intercalation systems, respectively

The pseudocapacitance could be defined as [19]:

$$C_{\emptyset} = q^* \cdot \frac{dX}{dV} \tag{1.14}$$

where q^* is the charge required for completion of monolayer sorption.

Applying Eq. (1.13) into Eq. (1.14) leads to:

$$C_{\emptyset} = \frac{q^* F}{RT} \cdot \frac{k \cdot \exp[\mathrm{VF/RT}]}{(1 + k \cdot \exp[\mathrm{VF/RT}])^2} = \frac{q^* F}{RT} \cdot X \cdot (1 - X) \tag{1.15}$$

It is found that the pseudocapacitance $C_{\emptyset}$ is not constant and has a maximum value at $X = 0.5$. Pseudocapacitor is similar to the EDL capacitor in the way that the stored charge is proportional to the applied potential. The fundamental difference between them lies in that faradaic charge transfer takes place in a pseudocapacitor. Noted that both battery and pseudocapacitor involve faradaic charge transfer. However, for a pseudocapacitor, the electrode potential associated with the electrosorbed electroactive species is a continuous function of the extent of the conversion of the electroactive material, i.e., the degree of utilization of free sites on the electrode surface or within the 2D or quasi-2D material ($\Delta G = \Delta G^o + RT \ln(X/(1 - X))$; While for most of the battery electrodes, the electrode potential is determined at some singular value by the Gibbs energies of pure, well-defined 3D phases and usually also the composition and/or concentration of the solution ($\Delta G = -nFE^o$) [19, 45, 46]. In addition, higher rate capability is always demonstrated for pseudocapacitor than batteries benefiting from the surface/near-surface reaction nature (Figs. 1.2 and 1.3).

1.2.1.2 Kinetic Electrochemical Features of ECs

While thermodynamic aspects of ECs have been introduced above, the practical application of ECs is strongly dependent on their kinetic behaviour. It should be stated that all electrochemical reactions are subjected to polarization effects that would sacrifice working voltage and reversible capacity [14, 19]. Therefore, although electrochemical capacitances could result from various electrochemical processes, they suffer from polarization effects and the ideal complete reversibility is not practical from a kinetic viewpoint. Indeed, there is an internal resistance, known as equivalent series resistance (R_{ESR}), for any electric power sources. Here we try to introduce the kinetic features of ECs from the point of R_{ESR} firstly, and then illustrate electrochemical features of pseudocapacitive via their responses to (i) potentiodynamic sweep (cyclic voltammetry); (ii) constant current (galvanostatic charge/discharge curves), and iii) alternating current (impedance spectroscopy) [14, 19].

Equivalent Series Resistance (R_{ESR})

Just as mentioned above, package electric power sources process intrinsic internal resistance (R_{ESR}), which is an important parameter that determines their power performance (Fig. 1.4a).

For a power source with working voltage (V_w), current (I) flow through the circuit with a load (R_L) on discharge could be given as [24, 47]:

$$I = \frac{V_W}{(R_L + R_{ESR})} \tag{1.16}$$

Accordingly, there is a resistance component in addition to the capacitive component described in Eqs. (1.2) and (1.3). The resistance component is governed as:

$$V_{drop} = IR_{ESR} \tag{1.17}$$

And then, the Eqs. (1.4) and (1.6) are modified, and new derivations are described as:

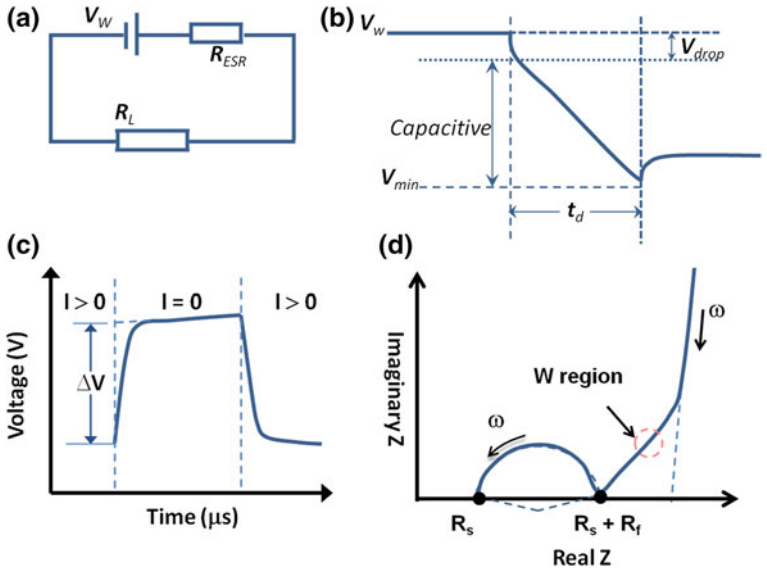

Fig. 1.4 **a** Typical electric circuit that a power source (V_w) with a load of (R_L) and an equivalent series resistance (R_{ESR}). **b** Constant current discharge curves for a EC (where V_w is working voltage, Capacitive is the voltage drop due to discharge of the capacitor (Eq. 1.2), V_{drop} is the voltage drop due to R_{ESR} (Eq. 1.17), V_{min} is the minimum voltage allowed by power system; t_d is the discharge time.). **c** Idealized voltage waveform during current interrupt event. **d** Typical Nyquist Plot for a pseudocapacitor

$$E = \int_0^Q V(q)dQ = \int_0^Q \frac{Q}{C}dQ \tag{1.18}$$

$$P = IV = I\left(V_W - V_{drop}\right) = I^2 R_L = \left(\frac{V_W}{R_L + R_{ESR}}\right)^2 R_L \tag{1.19}$$

From Eq. (1.19), the maximum power, P_{max}, could be derived at $R_L = R_{ESR}$ [48] and given as:

$$P_{max} = \left(\frac{V_W}{R_L + R_{ESR}}\right)^2 R_L = \frac{1}{4}\frac{V_W^2}{R_{ESR}} \tag{1.20}$$

By combing Eqs. (1.6) and (1.20), the shortest discharging time, t_{min}, can be derived and given as [24]:

$$t_{min} = \frac{1}{2}\frac{CV_W^2}{P_{max}} = 2CR_{ESR} \tag{1.21}$$

Determination of Equivalent Series Resistance (R_{ESR})

Several methods can be used to determine R_{ESR}, such as (i) measuring the *iR* drop at the initiation of a constant current discharge, (ii) measuring the bounce back of voltage at the end of a constant current discharge, or (iii) using AC impedance spectroscopy (often at 1000 Hz) [49].

iR drop. The R_{ESR} is usually determined from the galvanostatic discharge tests using *iR* drop for practical packed cell in lab. In this case, R_{ESR} is defined as the voltage change that occurs nearly instantaneously upon the application of current [48]. A change in the form of Eq. (1.17) could define the R_{ESR} as:

$$R_{ESR} = V_{drop}/I \tag{1.22}$$

This method is somewhat subjective because the data cannot be accurately described by an instantaneous drop followed by a perfectly linear discharge. In practical, the discharge curve is smooth with a gradual transitions. Nevertheless, this method does provide useful information for internal resistance of the cell from a first-order approximation. The results calculated from *iR* drop is inversely proportional to cell size [21, 48].

Current Interrupt Steps. The R_{ESR} could also be measured via constant current interrupt steps (<5 s) at a specified voltage. In this case, R_{ESR} is defined as the voltage change that occurs nearly instantaneously upon application of current [48, 49] (Fig. 1.4c):

$$R_{ESR} = \Delta V / \Delta I \tag{1.23}$$

It should be stated that this method is dependent on the methodology used, including the date sampling rate, electrode geometry, etc. [48]. Special caution should be given for porous electrode-based electrochemical systems, where the overestimation of the ohmic voltage change and the R_{ESR} of the cell would be expected via the interrupt method.

Electrochemical Impedance Spectroscopy (EIS). In EIS testing, a sinusoidal voltage perturbation at a well-defined frequency is applied to the cell with the desired state of charge. The resulting variation in current is recorded which provides information about the electrochemical response of the system over a wide range of frequencies (typically 10 kHz–1 Hz or lower) [48, 50, 51]. By fitting the EIS data, the resistance of a cell, such as solution resistance, electrode properties in terms of ohmic resistance and activation polarization resistance, EDL capacitance, and transport or diffusion properties [52–55], could be therefore characterized (Fig. 1.4d).

Typical Nyquist plot (Fig. 1.4d) shows a semicircle in the high-frequency region, followed by a Warburg and linear part in the low frequency region. The first crossover point on the Nuquist plot, R_s, is generally considered as the resistance associated with electrolyte resistance and the external contact resistance. R_f is the charge transfer resistance resulting from the EDL capacitance on the particle surface of the electrode, and/or the faradaic reactions. $R_s + R_f$ is the main contributor to R_{ESR}. It must be emphasized that the interpretation of the EIS data should be based on individual cases, and different experimental configurations will lead to different data interpretation. In the case where pseudocapacitive materials are present, perfect semicircles generally cannot be obtained. Instead, suppressed semicircles in high-frequency region with sloppy linear line in the low-frequency region might be obtained.

Kinetic Electrochemical Features of Pseudocapacitance

(a) **Potentiodynamic sweep-cyclic voltammetry (CV)**

In CV experiments, at various sweep rates (v, V/s or mV/s), ideally, there is no or small potential difference (or hysteresis) between the anodic and cathodic peaks in fast charge storage devices, and the CV curves are symmetric particularly at slow sweep rates for ideal capacitive system (Figs. 1.5a, b) [14, 19].

Sweep rate dependence of peak potential. One typical kinetic feature of pseudocapacitor is the presence of critical sweep rate. That is because, except for air or vacuum dielectric capacitors, all ECs have effective equivalent series resistance (R_{ESR}), which result in polarization effect and deviations from ideal capacitive behaviour. The presence of the charge transfer resistance in pseudocapacitors imposes kinetic limitations. If the surface faradaic processes involved for pseudocapacitors are modulated by an increasing sweep rate (v), the kinetic reversibility is lost gradually [19]. This is manifested by the peak potential, E_p, which remains

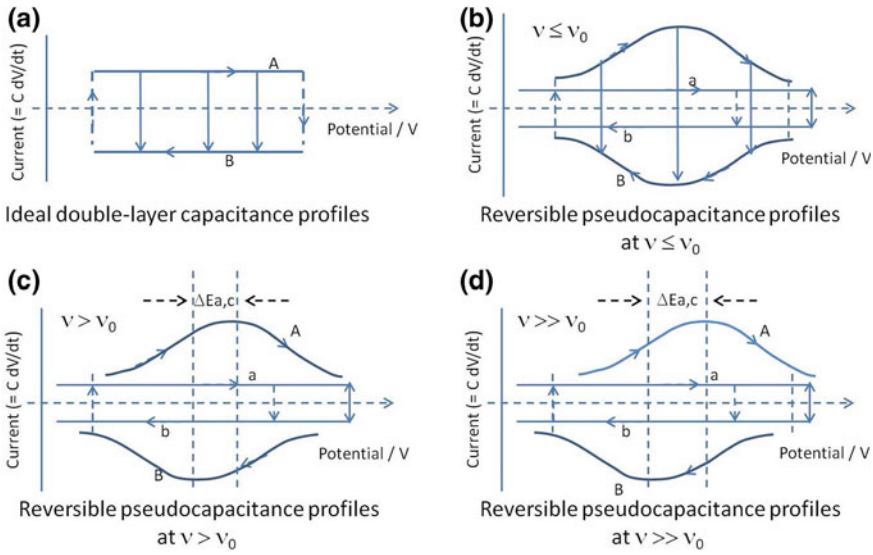

Fig. 1.5 CV profiles of ideal double layer capacitor (**a**) and Reversible pseudocapacitor (**b–d**) with different sweep rate *v*. v_o is the critical sweep rate [19]. Reprinted with the permission from Ref. [19]. Copyright 1991, The Electrochemical Society

independent of *v* until *v* reaches critical sweep rate v_o, and then increase with log *v* [56]. It indicates that there is a critical sweep rate value v_o from which the kinetic behavior is radically different [56]. For example, the cyclic voltammograms would translate into non-mirror images with the increase in the cathodic and anodic peak voltage separation ($\Delta E_{a,c}$) as $v > v_o$, indicating the transition from kinetic reversible process to a kinetic irreversible process (Figs. 1.5c, d) [57, 58]. But the kinetic reversibility could be regained for pseudocapacitor by lowering the sweep rate, since there is no phase change occurs during the change/discharge processes. The presence of kinetic limitation (characterized by the v_o value) determines the effective charge/discharge rates or power performance of ECs.

The cyclic voltammograms of EDLCs are always rectangular in shape with no or slight deviation upon the increase of the sweep rate. On the other hand, the CV curves of pseudocapacitors can be rectangular in shape with or without cathodic/anodic peaks (or wide pumps), depending on the type of electrode materials. Wide-broad redox peaks were generally observed for conductive polymers including polyaniline [59], polypyrrole [60] and PEDOT [61], and transition metal oxides (e.g., MoO_3 [62], V_2O_5 [63], T-Nb_2O_5 [64]). Typical pseudocapacitive electrode materials that exhibit nearly ideal rectangular cyclic voltammograms without distinct redox peaks are hydrous RuO_2 [65, 66] and MnO_2 [35] in aqueous electrolytes. More recently, $Ti_3C_2T_x$ Mxene is also found to produce rectangular-shaped CVs in sulfuric acid, originating from the continuous change in the titanium oxidation sate during charge/discharge process [42, 44]. These results

demonstrate that reversible faradaic reactions can result in similar electrochemical behavior as those of EDL capacitors. This makes the differentiation between EDL type of mechanism and pseudocapacitive mechanism rather difficult, especially for electrode materials that simultaneously possess both charge storage mechanisms. Nevertheless, efforts are made to roughly estimate the contributions from each of the two surface-controlled charge storage processes. Example will be given later.

Sweep rate dependence of response current. Another important and characteristic feature of the kinetic behaviour for pseudocapacitance is the relationship between the response current (i) and sweep rate (v). In cyclic voltammetry experiments, the total current measured under a potential sweep rate is the sum of the diffusion current (i_{diff}) and the current required to charge the double layer at the electrolyte interface/ignite fast faradaic reactions on the exposed electrode surface (i_{cap}) [67]. And it could be expressed as:

$$i(V) = i_{cap} + i_{diff} = av^b \tag{1.24}$$

where v is the sweep rate, and both a and b are adjustable parameters [68–71]. The parameter b-value is determined from the slope of the linear plot of log i versus log v. There are two well-defined conditions in general: b = 0.5 and b = 1. The slope b = 1 is representative of a capacitive contribution that arises from surface redox reactions, thus $i_{cap} = av$. While the slope b = 0.5 is denoted for semi-infinite diffusion-controlled faradaic process [68–70, 72]. The diffusion current (i_{diff}) could be described by the classical Sevick equation [73]:

$$i_{diff} = nFAC^* D^{1/2} v^{1/2} (\alpha nF/RT)^{1/2} \pi^{1/2} \chi(bt) \tag{1.25}$$

where n is the electron transfer number, F is the Faraday constant, A is the apparent surface area of the electrode materials, C^* is the concentration of active species, D is the diffusion coefficient of the rate limiting species, α is the transfer coefficient, R is the molar gas constant, T is the absolute temperature, and the $\chi(bt)$ functional part is the normalized current for a totally irreversible system as indicated by the cyclic voltammetric response.

It is derived from Eqs. (1.24) and (1.25) that the current response to sweep-rate varies depending on whether the reaction process involved is a surface mechanism (capacitive) or a diffusion-controlled mechanism. If the reaction process is controlled by surface mechanism, current varies linearly with v (di/dv = constant = the capacitance); for faradaic process limited by semi-infinite linear diffusion, the current varies with $v^{1/2}$ ($di/dv^{1/2}$ = constant) [67, 74]. Taking into account all cases, a general expression for current at a certain potential could be given [67, 74]:

$$i(V) = i_{cap} + i_{diff} = k_1 v + k_2 v^{1/2} \tag{1.26}$$

or it could be changed as:

$$i(V)/v^{\frac{1}{2}} = k_1 v^{\frac{1}{2}} + k_2 \tag{1.27}$$

The values of k_1 and k_2 could be evaluated from the slop and intercept, respectively, if $i(V)/v^{1/2}$ plotted versus $v^{1/2}$ give a straight line. Consequently, it becomes possible to separate the capacitive contribution from diffusion-controlled intercalation processes, and quantify the current or capacitance fraction related to each of these contributions. This technique has been utilized to evaluate the electrochemical performance of nanostructures materials (Fig. 1.6a, b) [68, 75–78]. It is interestingly found that the contribution fraction of each parts is strongly dependent on materials crystalline [78], structure or morphology [75, 79], particle size [68], electrolyte [76] and sweep rate [77].

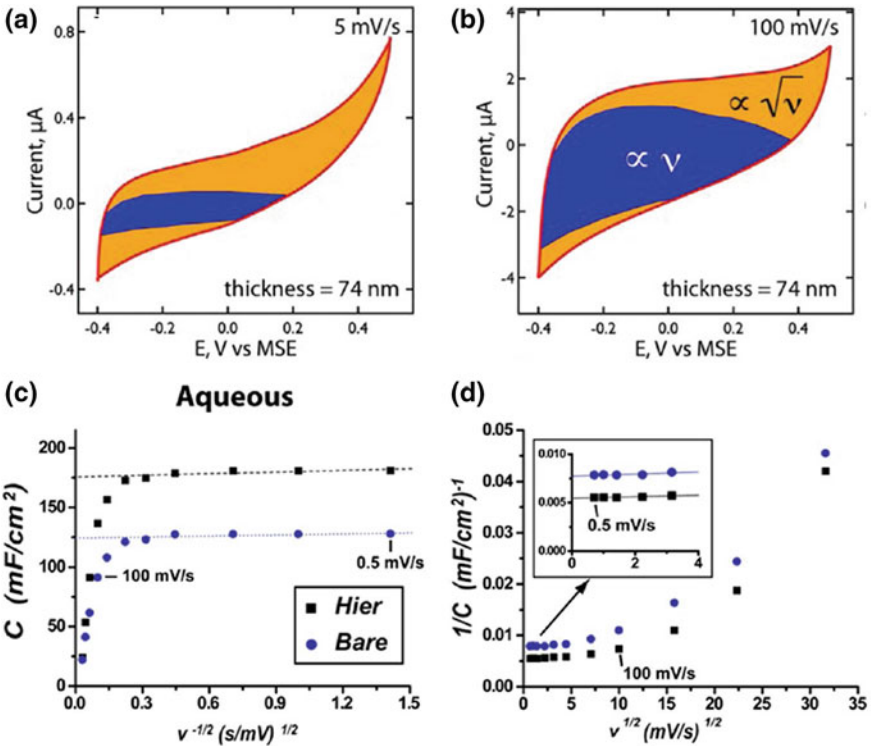

Fig. 1.6 CV curves of Au/MnO_2 core-shell nanowires at sweep rates of 5 mV/s (**a**) and 100 mV/s (**b**): capacitive current ($i \propto v$, *blue part*) was separated from diffusion current ($i \propto v^{1/2}$, *yellow part*) [75]. Reprinted with the permission of American Chemical Society, copyright 2012 (**c**) Typical areal capacitance (C) versus $v^{-1/2}$ plots and (**d**) 1/C versus $v^{1/2}$ plots for bare (*blue circles*) and hierarchical (*black squares*) MnO_2 nanowire arrays in aqueous $LiClO_4$ electrolyte [76]. Reprinted with the permission of American Chemical Society, Copyright 2013

Sweep rate dependence of capacitance. The variation of voltammetric surface charge q^* with the sweep rate v has been described by Trasatti et al. on RuO_2 electrodes via a linear function [80]:

$$q^* = q_s^* + q_d^* \tag{1.28}$$

The maximum charge density q^* is considered to consist of two fractions, q_s^* and q_d^*, representing the charge related to outer (capacitive contribution) surface and inner (diffusion-controlled contribution) surface. The q_s^* that corresponds to outer surface could be obtained at infinite potential sweep rate ($v \to \infty$),

$$q^* \to q_s^* \tag{1.29}$$

The maximum charge density (q_m^*) could be obtained when at the sweep rate ($v \to 0$),

$$q^* \to q_m^* \tag{1.30}$$

Particularly, q^* is expected to be limited by $v^{-1/2}$ if semi-infinite linear diffusion is involved whereas capacitive contributions are independent of the sweep rate, thus Eq. (1.28) could be expressed as:

$$q^*(v) = q_{v\to\infty}^* + q_d^* = q_{v\to\infty}^* + const\left(v^{-1/2}\right)^* \tag{1.31}$$

from which, a basic amount of q_s^* could be collected via the extrapolation of linear diagram of q^* versus $v^{-1/2}$ to $v^{-1/2} = 0$ (Fig. 1.6c).

Generally, q^* decreases as the potential sweep rate increases because of diffusion limitation [80]. Since q_s^* increases linearly with $v^{-1/2}$, it is reasonable to expect that $1/q^*(v)$ decrease linearly with $v^{1/2}$:

$$1/q^*(v) = 1/q_m^* + const\left(v^{1/2}\right)^* \tag{1.32}$$

where q_m^* is the maximum total charge. Extrapolation of liner plot of $1/q^*(v)$ versus $v^{1/2}$ to $v^{1/2} = 0$ gives the basic amount of the maximum total charge q_m^* (Fig. 1.6d).

Consequently, the difference between the total charge (q_m^*) and the surface charge ($q_{v\to\infty}^*$) give the charge associated to diffusion-controlled processes.

$$q_d^* = q_m^* - q_{v\to\infty}^* \tag{1.33}$$

Similarly, the ratio of capacitive contribution and semi-diffusion controlled contribution for the total capacity would be evaluated.

Sweep rate dependence of double-layer capacitance and Pseudocapacitance. The separation of capacitive current/charge from diffusion-controlled current/charge has been well addressed in above via cyclic voltammetry. Capacitive charge storage

consists of contributions from both double-layer capacitive and pseudocapacitve effects.

$$C = C_{dl} + C_{\emptyset} \tag{1.34}$$

Through proper design of experiment, CV can sometimes (not always) be used to differentiate EDL mechanism from fast surface redox reaction, as demonstrated by Dunn, et al. [81]. Mesoporous Nb_2O_5 with crystallographically orientated layered nanocrystalline walls shows typical intercalation pseudocapacitance through fast cation intercalation into layered gaps (van der Waal gaps) of Nb_2O_5. When mesoporous Nb_2O_5 with crystalline walls was used as the electrode, the use of different electrolyte (and thus different cations) determines different charge storage mechanism. When tetrabutylammonium (TBA^+) perchlorate in propylene carbonate is used as the electrolyte, the total charge storage shown in the CV curve (very small response current) (Fig. 1.7a) is based on EDL mechanism only since the bulky TBA^+ cations cannot be intercalated into the layered Nb_2O_5 quickly; whereas in $LiClO_4$ electrolyte, both EDL and intercalation pseudocapacitive processes contribute to the total charge storage (as evidenced by the much larger response current in Fig. 1.7a). The ratio of the EDL capacitance/pseudocapacitance could therefore be estimated from the CV results. A small fraction ($\sim 10\%$) of the total charge storage stems from EDL capacitance while most of the charge is stored through a surface-confined faradaic charge-transfer process. This is further confirmed by broad peaks in the voltages profiles in Fig. 1.7b, which is characteristic of a surface-confined charge-transfer process [81]. It must be emphasized that the method discussed here should be used with great care and it can only provide a rough estimation of the contribution from the EDL process and the surface redox processes. In addition, it is limited to certain types of electrodes only and the method will not work properly if highly porous electrodes containing pores much smaller than the size of the electrolyte ions are present in the system.

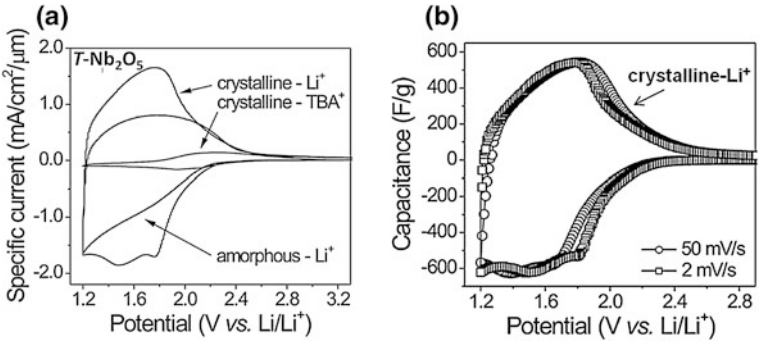

Fig. 1.7 **a** Cyclic Voltammetry (CV) curves of amorphous and crystalline mesoporous T-Nb_2O_5 films in Lithium (Li^+) and tetrabutylammonium (TBA^+) electrolyte at a sweep rate of 10 mV/s [81]. **b** Potential-dependant capacitance calculated from CV curves at sweep rate of 2 and 50 mV/s. Reprinted with the permission of American Chemical Society, Copyright 2010

(b) **Constant current-charge/discharge curve**

As mentioned above, the profile of potential versus capacitance for EDL capacitor is well-defined linear in shape as described by Eq. (1.3) and is illustrated in Fig. 1.8a. For pseudocapacitor, the electrode potential associated with the electrosorbed species is a continuous logarithimic function of the extent of sorption (Eq. 1.12), which is different from the linear function of that of EDL capacitor. In a constant current charge/discharge process, this translates into smooth charge/discharge profiles with small potential hysteresis (Fig. 1.8b). On contrast, a battery electrode shows a potential plateau without a sloping line in potential versus capacity profile (Fig. 1.8c).

(c) **Alternating current-impedance spectroscopy**

EIS is an efficient tool for monitoring changes in ECs and determining their dynamic electrochemical behaviour by applying a sinusoidal voltage perturbation to ECs at a well-defined frequency. The corresponding information regarding the electrochemical response of the system at that frequency is then derived from resulting current response. The equivalent electric circuit diagram is usually used to interpret the experimental data. If the behavior of an EC is purely capacitive, the R_{ESR} is frequency-independent with the real and imaginary components being out of phase by 90°, and the Nyquist plot is a vertical line with a resistive element R being connected in series with the capacitor C [14, 18, 21]. The resistive element represents the resistance from the electrolyte solution and/or from the external contact. However, most practical ECs deviate from purely capacitive behavior because of kinetic limitations, and therefore the equivalent circuit is more complex. The equivalent electric circuit model for EDL capacitor is generally approximated with the EDL capacitance (C_{dl}), being in parallel with a resistor R_f, and an additional resistance (R_s) that corresponds to electrolyte resistance and the external contact resistance. For pseudocapacitive system, faradaic resistance R_f and pseupcapacitance $C_{\emptyset}$ that associates with potential-dependent charge is connected in series, and being in parallel with EDL capacitance (C_{dl}) since pseudocapacitance arises from a potential dependent interfacial faradaic reaction. The practical

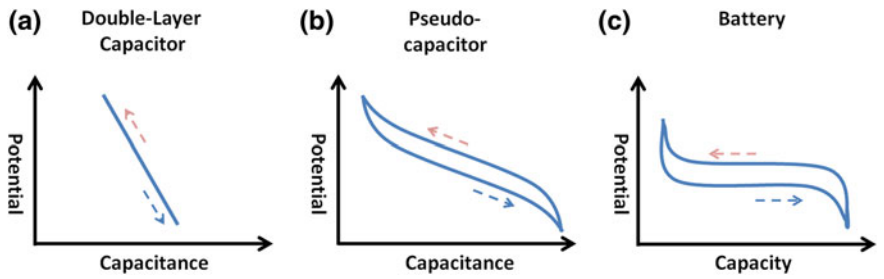

Fig. 1.8 General electrochemical features of double-layer capacitor (**a**), pseudocapacitor (**b**) and battery (**c**)

impedance results for a solid electrode/electrolyte interface often display a frequency dispersion that cannot be described by simple elements such as capacitor, resistor, inductor or Warburg diffusion. Therefore, a constant phase element (CPE) which allows for a distribution of capacitance values is generally introduced in order to provide much better impedance fittings (Fig. 1.9) [82]. The definition of constant phase element in the equivalent circuit is given as [82, 83]:

$$Z_{CPE} = \frac{1}{T(j\omega)^{\alpha}} \tag{1.35}$$

here, Z_{CPE} is the impedance, T is a constant in F cm^{-2} $s^{\alpha-1}$, ω is the frequency, α is an adjustable constant. When $\alpha = 1$, the CPE is regarded to represent an ideal capacitor. It would be a resistor for $\alpha = 0$, and an inductor for $\alpha = -1$. Particularly, the $\alpha = 0.5$ indicates semi-infinite diffusion.

Based on the equivalent electric circuit diagram (Fig. 1.9), it is apparent that the separation of EDL contribution from pseudocapacitive contribution for certain types of electrodes is possible by fitting the AC impedance result appropriately. An example is shown in Fig. 1.10, where the EDL and pseudocapacitive contributions in CeO_2 thin film electrodes are distinguished using AC impedance measurement at different applied potentials [79]. For potential above 3 V, very small EDL capacitance was obtained due to the high electronic resistance of ceria when Ce is in its fully oxidized state. At lower potentials, a sizable fraction of Ce^{4+} reduces to Ce^{3+} and the electronic conductivity increases. The film electrode therefore delivers significant amounts of capacitance. The pseudocapacitve contributions increase

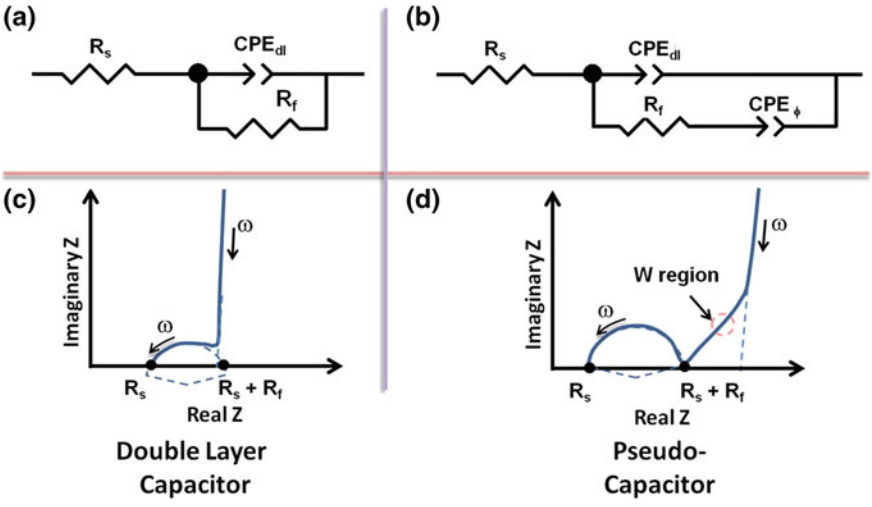

Fig. 1.9 Equivalent circuits for: **a** double-layer capacitor, and **b** Pseudocapacitor. Corresponding electrochemical impedance spectroscopy results are listed in **c**, **d**, respectively [18]. Reprinted with the permission of Springer, Copyright 2003

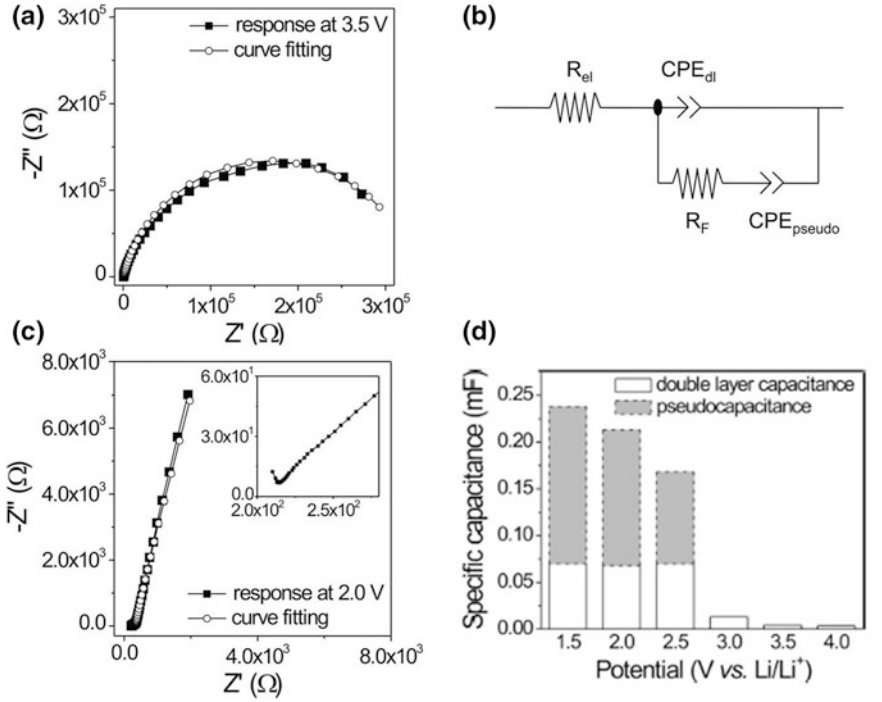

Fig. 1.10 Nyquist plot for KLE-template CeO_2 at the potential 3.5 V (**a**) and 2.0 V (**b**) (vs. Li/Li^+). **c** Equipment circuit model for impedance data fitting. **d** Separation of double layer capacitance and pseudocapacitance based on different applied potentials for CeO_2 films [79]. Reprinted with the permission of American Chemical Society, Copyright 2010

with decreasing voltage while EDL contributions remain almost unchanged for applied potential less than 3 V, suggesting different charge storage mechanisms are involved under different applied potentials [79].

1.2.1.3 Symmetric and Asymmetric Supercapacitors

The well-known reciprocal relation between overall capacitance of the device (C) and that of two individual electrodes (C_1 and C_2) could be given as follows [17, 18]:

$$\frac{1}{C} = \frac{1}{C_1} + \frac{1}{C_2} \tag{1.36}$$

If $C_1 = C_2$ (symmetric combination, for example, two same non-faradaic electrode work against with each other), the measured C would be half the value of individual electrode. This type of system is called as "symmetric capacitor" [18]. If the capacitance of the cell is adjusted further via combining mass of two electrodes, a factor of

"4" would introduce. For example, a single carbon electrode (with high surface area 1000 m^2/g) exhibits the capacitance of 10 $\mu F/cm^2$. This gives rise to a specific capacitance of 100 F/g for one electrode. For a symmetric capacitor, two electrodes with half the total capacitance (Eq. 1.36) and doubled weight results in an 25 F/g active capacitor [17]. The significant differences between single electrode and the complete is of significant importance and should be clarified when an EC is introduced.

If electrode "2" refers to faradaic electrode (or battery-type electrode), corresponding C_2 is essentially infinity. Thus $C \approx C_1$ is approximated according to Eq. (1.36) because of pseudocapacitance $C_2 \gg C_1$, and the full charge stored on C_1 (non-faradaic electrode) is hence available for discharge. This type of system is called as "asymmetric capacitor" [18].

The maximum energy stored in such a capacitor is given by [14, 16, 17, 19, 21, 25]:

$$E = \frac{1}{2} C V_w^2 \tag{1.37}$$

where V is nominal voltage (volts).

The maximum power is described by the equation:

$$P_{max} = \frac{1}{4} \frac{V_W^2}{R_{ESR}} \tag{1.20}$$

where R_{ESR} is equivalent series resistance (Ω). For the packed cells, the R_{ESR} is typically determined via measuring the IR drop, the bounce back of voltage, or using AC impedance spectroscopy [21, 84].

1.2.1.4 Summary for Double-Layer Capacitance and Pseudocapacitance

See Table 1.1.

Table 1.1 Separation of double-layer capacitance and pseudocapacitance

	Double-layer capacitance	Pseudocapacitance or supercapacitor
Mechanism	No-faradaic involved	Faradaic involved
Capacitance-voltage	Capacitance constant (potential-independent)	Capacitance not constant (potential-dependent)
Phase angle-frequency	90° phase angle	Phase angle function of frequency, but some embodiments have transmission-line behaviour
Kinetic aspect	High-power operation	Kinetic limitations for high charge/discharge rates
Reversible	Indefinitely reversible	Highly reversible
Electrode material	Carbon allotropes	Transition metal oxides/hydroxides, conducting polymers, MXenes etc.

1.2.2 Lithium-Ion Battery

1.2.2.1 Thermodynamic Aspects of Battery

Similar to ECs, the energy and power features of battery follow directly from the thermodynamic principles for electrochemical reactions, which can be given as [46]:

$$\Delta G = \Delta H - T\Delta S \quad \text{and} \quad \Delta G^{\circ} = \Delta H^{\circ} - T\Delta S^{\circ} \tag{1.38}$$

where ΔG is the Gibbs free energy, ΔH is the enthalpy, ΔS is the entropy and T is the absolute temperature.

It is noted that ΔG represent the net useful energy resulting from a given reaction, and it would be in terms of electrical energy for a battery/cell and expressed as follow:

$$\Delta G = -nFE \quad \text{and} \quad \Delta G^{\circ} = -nFE^{\circ} \tag{1.39}$$

where n is the electron transfer number, F is the Faraday constant, E is the cell electromotive force (EMF). The cell EMF is determined at some singular value by the Gibbs energies of pure, well-defined phases and is unique for each redox reaction couple. This is totally different from the continuous logarithmic-dependent electrode potential of ECs.

The free energy for bulk chemical reactions is given according to van't Hoff isotherm [46, 85, 86]:

$$\Delta G = \Delta G^{\circ} + RT\ln(A_P/A_R) \tag{1.40}$$

Nernst equation for electrochemical reactions could be derived by combining Eqs. (1.39) and (1.40) [46, 85, 86]:

$$E = E^{\circ} + (RT/nF)\ln(A_R/A_P) \tag{1.41}$$

here, R is the gas constant, T is the absolute temperature, A_P is the activity of products and A_R is the activity of reactants.

The relationship between the current flow and the extent of reaction could be expressed as follows:

$$I = -nF\frac{m}{MW}/t \tag{1.42}$$

where I is the current flow, n is the number of electron involved in the reaction, m is the weight of active materials, MW is the molecular weight of active materials, and t is the time of current flow.

Based on these, the total charge (Q) could be given as [85–87]:

$$Q = \int_0^{\Delta t} Idt = \int_o^Q dq \tag{1.43}$$

where q represents the state of charge. Q is the cell capacity that depending on I. In addition, changes in electrode volume, electrode decomposition and electrode-electrolyte chemical reactions result from charge/discharge cycling would cause an irreversible loss of capacity. Therefore, the Coulomb efficiency is one of important metric for a battery/cell, which can be described as follows [85]:

$$Coulom\ efficiency = 100 \times Q_{dis}/Q_{ch} \tag{1.44}$$

The densities of stored energy and power are given as:

$$Energy\ density = \int_0^{\Delta t} IV(t)dt = \int_o^Q V(q)dq \tag{1.45}$$

$$Power\ density = V(q)I(q) \tag{1.46}$$

where Δt is the time required for complete discharge at a constant current $I_{dis} = dq/dt$. Based on Eqs. (1.43) and (1.45), it is apparent that the stored energy is strongly dependent on the average ($V(q)$) and the capacity (Q).

The electrochemical potential difference between anode (μ_a) and cathode (μ_c) gives rise to the open-circuit voltage (V_{oc}) of a cell [86]:

$$V_{oc} = (\mu_a - \mu_c)/e \tag{1.47}$$

In practical batteries, the open-circuit voltage is also limited by the "working window" of the electrolyte. The electrolytes for practical rechargeable battery systems are crystalline solid, glass, polymer, or liquid. The working window is determined by the energy gap between the lowest unoccupied molecular orbital (LUMO) and the higher occupied molecular orbital (HOMO) for a liquid electrolyte (Fig. 1.11) or the bottom of the conduction band and top of the valence band for a solid electrolyte [85, 88]. For a thermodynamically stable cell, the electrochemical potentials of anode μ_a and cathode μ_c of a charged cell should be matched the LUMO and HOMO of the electrolyte for achieving maximum $V(q)$ of a stable and safe cell. That is because electrolyte would be reduced when the μ_a of anode is above its LUMO and would be oxidized when the μ_c of cathode is below its HOMO. Alternatively, the solid-electrolyte interphase (SEI) passivation layer that is electronically insulating but permeable to the working ion would form to stabilize a mismatched electrode system [85, 87].

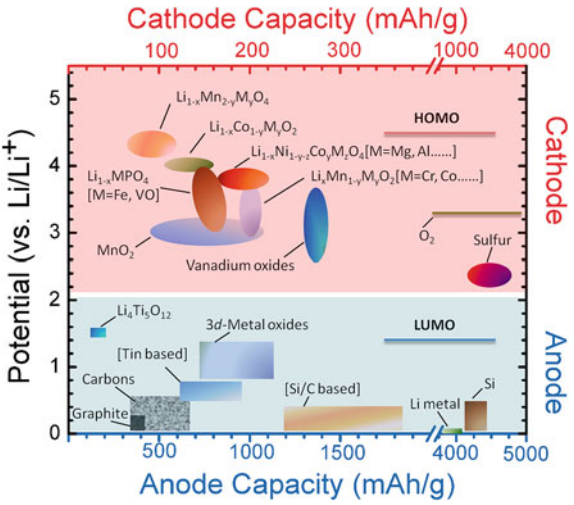

Fig. 1.11 Voltage and capacity ranges for some cathode and anode materials

1.2.2.2 Kinetic Aspects of Battery

During discharge, the voltage drop off (electrode polarization) would occur when current flow across the battery. This results from kinetic limitations of reactions, in which an internal resistance R_b reduce the output voltage V_{dis} of a cell relative to the open-circuit voltage V_{oc} by a polarization $\eta = I_{dis}R_b$ [46, 85]. The polarization, η, is thus given as:

$$\eta(q, I_{dis}) = V_{oc} - V_{dis} \tag{1.48}$$

Reversely, the presence of R_b would increases the voltage required to reverse the chemical reaction upon charge by an overpotential $\eta(q, I_{ch})$ [86]:

$$V_{ch} = V_{oc} + \eta(q, I_{ch}) \tag{1.49}$$

Generally, there are three different kinetic effects for polarization: (i) activation polarization, (ii) ohmic polarization, and (iii) concentration polarization (Fig. 1.12a) [46, 89, 90].

Activation polarization arises from kinetics hindrances of the electrochemical redox (or charge-transfer) reactions taking place at the electrode/electrolyte interfaces of anode and cathode. For a charge-transfer-controlled battery reaction, the current flow i, could be given as [46]:

$$i = i_0 \exp(\alpha F\eta/\mathrm{RT}) - \exp((1-\alpha)F\eta/\mathrm{RT}) \tag{1.50}$$

where η is the polarization, α is the transfer coefficient. $i_0 = k_0 FA$ is the exchange current density (k_0 is the reaction rate constant for the electrode reaction, and A is the activity product of the reactants).

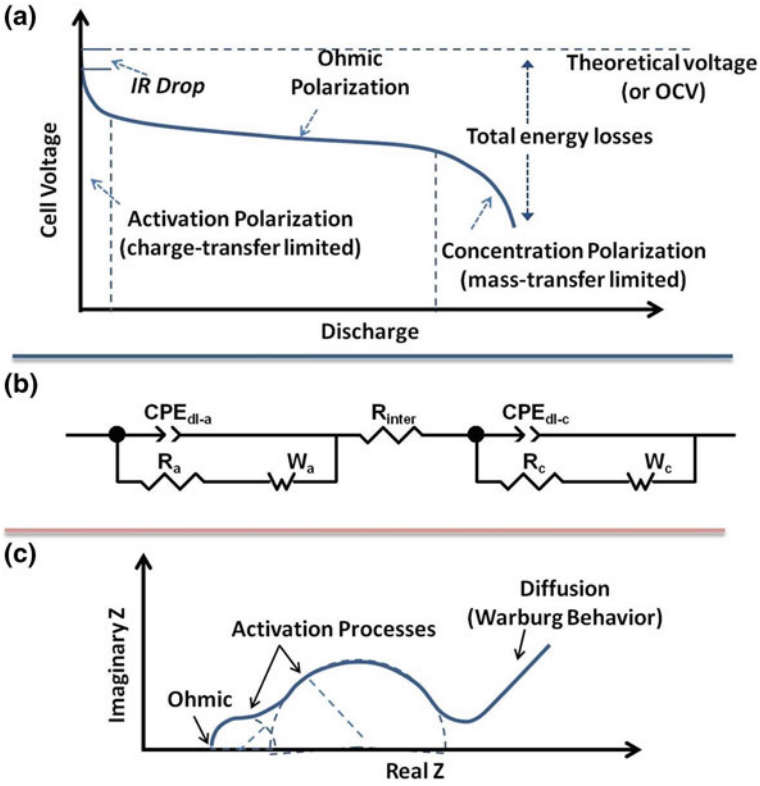

Fig. 1.12 **a** Typical discharge curve of a battery, showing different types of polarization. **b** Simple battery circuit diagram, **c** Corresponding Nyquist plot for an idealize battery system, where characteristic behaviors of activation, ohmic, and concentration polarizations are distinguished. W_a and W_c are the Warburg impedances of diffusion process for anode and cathode, respectively. R_a and R_c are the resistances of the anode reactions and cathode reactions. R_{inter} is the internal resistance of battery. $CPE_{dl\text{-}a}$ and $CPE_{dl\text{-}c}$ are the constant phase elements for anode and cathode, respectively [46]. Reprinted with the permission of American Chemical Society, Copyright 2004

Derived from Eq. (1.50), the activation polarization following the Tafel equation was given as:

$$\eta(q, I_{dis}) = a - b\log(i/i_0) \tag{1.51}$$

Ohmic polarization consists of the resistance of individual cell components (electrodes, electrolyte, the conductive additive, binder, current collectors, terminals) and the contact resistance among various individual components. Ohm' Law is obeyed for ohmic resistance R:

$$\eta(q, I_{dis}) = IR \tag{1.52}$$

Concentration polarization results from mass transport limitations during cell operation, in which the availability of the active species at the electrode/electrolyte interface changes and becomes diffusion-limited. The concentration polarization for diffusion-controlled process can be expressed as

$$\eta(q, I_{dis}) = (RT/n)\ln(C/C_0) \tag{1.53}$$

where C is the concentration at the electrode/electrolyte interface, and C_0 is the concentration in the bulk of the solution.

In reality, the influence of the current rate on the cell voltage is controlled by all three types of polarizations. Similar to that of ECs, EIS is often used to access the kinetic behavior of a battery during the charge/discharge process. It is possible to distinguish different types of polarization by proper fitting of the impedance plot. The equivalent circuit model and the corresponding Nyquist diagram is shown in Fig. 1.12b, c. The activation polarization is often reflected by two semicircles or arcs in Nyquist plot [91, 92]. The first semicircle or arc at higher frequency is associated with the contact resistance between the electrode material and the metallic substrate coupled with a double layer capacitance [91], while the second semicircle or arc at lower frequency is associated with the charge transfer resistance between the electrode materials and the active species from the electrolyte coupled with a CPE element. In anode where there is a SEI layer, the contribution of the SEI resistance will come into the picture as well. Ohmic polarization has no capacitive character and is independent of frequency. It is represented as battery internal resistance R_{int}. The concentration effect is encapsulated as the Warburg element W. It reveals typical diffusion-controlled processes in the low frequency featured by 45° Warburg region, which is associated with the diffusion of the active species inside the solid electrode. A good battery cell should have small R_{int}, R_a, R_c and short Warburg region.

1.2.3 Electrochemical Capacitor Versus Battery

In this section, the properties and differences of electrochemical capacitors and batteries are summarized in terms of electrochemical behavior and thermodynamic behaviour.

1.2.3.1 Thermodynamic Behavior

See Table 1.2.

Table 1.2 Comparative thermodynamic behavior of electrochemical capacitor and ideal battery [19, 28, 45]

Electrochemical capacitor		Battery
Double layer capacitor	Pseudocapacitor	
Free energies ΔG of the electroactive materials **change continuously** with the extent of charge/discharge		Free energies ΔG of the electroactive phases involved are **unique** and **single-valued** during discharge/charge process $\Delta G \cong Constant = -nFE$
$G = 1/2CV^2$	$\Delta G = \Delta G^o + RT\ln(X/(1-X))$	
Potential varies continuously with ***time***	Potential varies continuously with ***the state of charge/discharge***	Potential on discharge/charge is ***single-valued***
Behavior is ***capacitative***		Behavior is ***non-capacitative***
High degree of ***reversibility***		***Irreversibility***

1.2.3.2 Electrochemical Properties

See Table 1.3.

Table 1.3 Comparative electrochemical characteristics of electrochemical capacitor and battery [14, 19, 45]

Electrochemical capacitor		Battery
Double layer capacitor	Pseudocapacitor	
Potential is thermodynamically related to the state of charge (Q) directly in a continuous manner	***Potential*** is thermodynamically related to the state of charge through log[X/1 − X] factor in a continuous manner	***Electromotive force (EMF)*** is ideally constant with the degree of charge/discharge, except for nonthermodynamic incidental effects, or phase changes during discharge
Free energies vary with extent of charge field in a continuous manner	***Free energies*** vary with degree of conversion in a continuous manner	***Free energies*** of components are single-valued
Galvanostatic discharge exhibits linear decline of potential with time	***Galvanostatic discharge*** exhibits a "transition" from linear decline of potential to a more or less constant potential	***Galvanostatic discharge*** arises at a more or less constant potential (except for intercalation Li batteries)
The linear modulation of potential exhibits more or less ***constant*** charge/discharge current profile (with some dependence on materials)		The linear modulation of potential displays irreversible i versus V profile with ***non-constant currents***
The cyclic voltammetry curves are ***mirror images***	The cyclic voltammetry curves are ***mirror images until v reaches to*** v_o	The charge/discharge profiles and cyclic voltammetry are ***not mirror images***

Table 1.4 Overall comparison of electrochemical capacitor and ideal battery [45]. Reprinted with the permission of Springer Sci. Bus. Media, Copyright 1999

Electrochemical capacitor		Battery
Double layer capacitor	Pseudocapacitor	
Galvanostatic discharge exhibits linear decline of potential with time (good intrinsic stage-of-charge indication)	***Galvanostatic discharge*** exhibits a "transition" from linear decline of potential to a more or less constant potential (relatively good intrinsic stage-of-charge indication)	***Galvanostatic discharge*** arises at a more or less constant potential (poor intrinsic stage-of-charge indication) (except for intercalation Li batteries)
Relatively poor energy density	***Moderate*** energy density	***Moderate or good*** energy density (depending on active materials and battery types)
Good power density	***Moderate*** power density	***Moderate or poor*** power density
Excellent cyclability	***Moderate cyclability***	***Poorer cycle life*** (due to irreversibility of redox and phase-changes in 3D dimensions)
Internal iR drop (related to *high specific area* of electrodes and electrolyte and their surface chemistry)		***Internal iR drop*** (due to surface chemistry of *electrolyte and active materials*)
No or little activation polarization (but C may be Temperature-dependent)		***Significant*** Temperature-dependent activation polarization
Long life time (except for corrosion of current collector, etc.)	***Moderate life time*** (due to degradation of active materials)	***Poorer life time*** (due to degradation and reconstruction of active materials)

1.2.3.3 Overall Comparison of Electrochemical Capacitor and Battery Characteristics

See Table 1.4.

1.3 Introduction to Graphene

Graphene, a single atomic layer of sp^2-bonded carbon atoms in hexagonal lattice, has attracted unprecedented interest owing to its intrinsic difference from other forms of carbon allotropes (Fig. 1.13) [93]. It exhibits excellent mechanical [94], electrical [95], thermal [96], and optical properties [97], and is particularly suitable for the implementation in electrochemical applications because of extraordinary electrical conductivity (64 mS cm^{-1}) [98], large specific surface area (theoretical

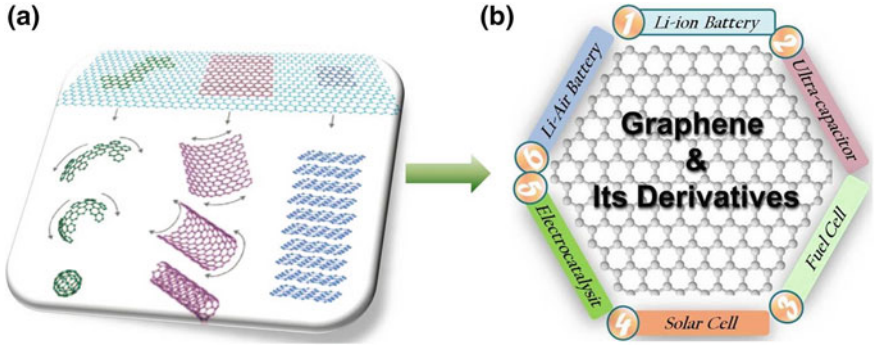

Fig. 1.13 **a** Graphene: the parent of all graphite forms and **b** their applications in Both Energy Conversion and Storage Devices [102]. Reprinted with the permission of WILEY-VCH Verlag GmbH & Co. KGaA, Weinheim, Copyright 2009

surface area $\sim 2630\ m^2\ g^{-1}$) [99], unique heterogeneous electron transfer and charge carrier rates, and good electrochemical stability [100]. Graphene/Graphene-based composites have been used as effective counter electrodes for dye-sensitized solar cells, photo-catalysts for water splitting, electrocatalysts for oxygen reduction/hydrogen evolution in fuel cells, high-performance electrodes in super-capacitors, ions (Li^+, Na^+, Al^{3+}, etc.) batteries, lithium-sulfur batteries and lithium-O_2 batteries [101]. The synthesis of graphene in both high quality and quantity in a green and economical way is therefore highly desirable.

1.3.1 Various Approaches Leading to Graphene Oxide/Graphene

Since the first fabrication of single-sheet graphene through micromechanical cleavage of bulk graphite was reported [103], a number of methods have been proposed for generating graphene with high quality and low cost, which can be classified into two categories: bottom-up approach and top-down approach (Fig. 1.14) [104]. Bottom approaches, based on the catalytic decomposition of hydrocarbon gases, can provide large sized graphene with high crystal nature via epitaxial growth [105] or Chemical Vapour Deposition [106] although their high cost and low production. Top-down approaches, consisting of the intercalation of additional elements between graphite layers to form graphite intercalation compound (GIC), and then followed by the exfoliation of GIC either by physical, chemical or electrochemical methods, have received intense interest due to their scalability and low production cost [107–110].

Chemical exfoliation of graphene based on Brodie, Staudenmaier and Hummers methods, which involves the oxidation of graphite with strong acids and oxidants, and subsequent chemical or thermal reduction, is particularly favorable due to

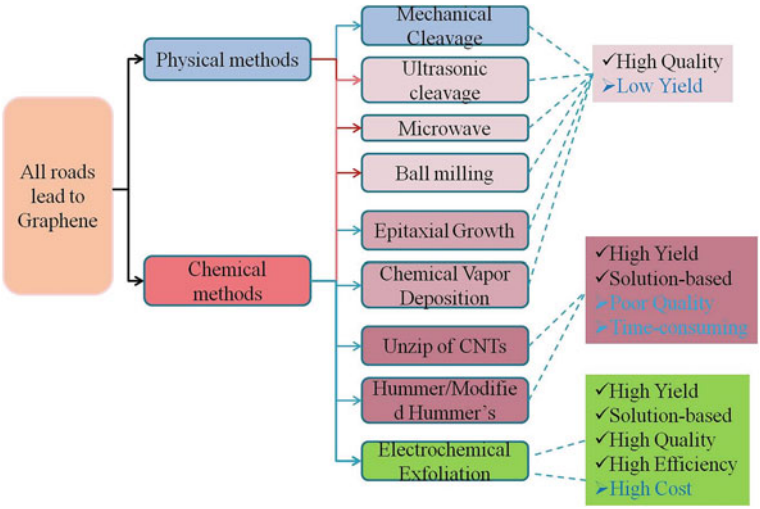

Fig. 1.14 All roads lead to Graphene or Graphene oxide (GO)

easy-processing and scalability [107]. Unfortunately, the use of strong acids and oxidants severely damages the sp^2-bonded of graphene and deteriorates its performance in various applications even though these damages could be recovered partially by subsequent reduction process [108].

Ultrasonic cleavage was also used to prepare graphene [109, 111]. However, the success of ultrasonic cleavage is strongly dependent on the proper choice of solvents and surfactants as well as the sonication frequency amplitude and time, which thus impedes its practical applications [110]. Graphene sheets can also be generated by unrolling carbon nanotubes (CNTs) via simultaneous intercalation of NH_3-solvated Li^+ into interlayer space of MWCNTs [112], or use strong oxidizing agents $KMnO_4$ to cut MWCNTs along the longitudinal direction [113].

Microwave-assisted heating technique was also adopted for the synthesis of water-soluble graphene due to the strong microwave absorption ability of graphitic materials [114]. Recently, electrochemical exfoliation of graphite and HOPG has been reported to be an effective way to prepare graphene and attracted increasing attentions [115–117].

1.3.2 Graphene for Soft Energy Storage Devices

The electrochemistry of graphene has been investigated intensively with respect to surface chemistry and structure, heterogeneous charge transfer rate constants on redox species, electrochemical operating window, and electrocatalysis of molecules recently [118, 119]. Particularly, the sharp proliferation of portable,

ultrathin/lightweight and wearable electronics, such as roll-up displays, touch screens, implantable medical devices, conformable health-monitoring electronic skin, wearable sensors and active radio-frequency identification tags (RFID), have promoted increasing demand for new power sources with high energy/power density, low cost, environmentally-friendly, as well as ultrathin, lightweight and flexible features [120–123]. One key challenge for soft energy storage devices lies in the development of deformable and high energy density electrodes with multiple merits via selecting and designing both current collector and electrode active materials [121, 123]. Soft electrodes are generally made from various functional organic and/or inorganic materials building on flexible conductive substrates without binders and conductive additives. Various soft electrodes have been prepared from paper-like carbonaceous electrode support, such as carbon nanotubes network (CNTs) [33, 124], graphene paper [120, 122], carbon cloth [125, 126], and other conductive paper (e.g., cellulose, textile, etc.) [123, 127]. Among them, electrodes based on CNTs network and/or graphene paper supports have attracted more attentions because of lightweight, good electric conductivity [95], large surface area [99], and good physical/chemical stability [100]. Graphene foam (GF), a 3-D interconnected network of chemical vapour deposition-grown graphene, has proven to be effective scaffold for soft energy storage devices [122]. Various soft electrodes based on GF, including GF/Fe_3O_4 [128], GF/$LiFePO_4$ [122, 129] and GF/MnO_2 [130], have been prepared and exhibit enhanced electrochemical performance.

Although significant process has been made until now, the synthesis of high-quality graphene via an economic and environmentally-friendly way remains extremely challengeable. In addition, the exploring of graphene-based composites for their practical applications in flexible energy storage devices including supercapacitors and rechargeable batteries is highly-desirable and meaningful. These issues and challenges were addressed to some extent in this thesis. Briefly, in Chap. 2, a novel electrochemical exfoliation method that is green, efficient and economic was proposed for the gram-scaled synthesis of high quality graphene. The underlying mechanism was elucidated, the synthesis conditions were optimized, and the electrochemical performance of resultant samples was evaluated. Chap. 3 is focused on the design of flexible graphene foam (GF)/Fe_3O_4 hybrid electrode for lithium-ion battery via atomic layer deposition approach. In Chap. 4, a novel carbon-based hybrid structure, named GF/carbon nanotubes (CNTs) hybrid films, was designed via a facile chemical vapor deposition (CVD) approach. This hybrid structure extends the 2D plane of Graphene into 3D directions without sacrificing electric conductivity and mechanical integrity. These features makes GF/CNTs hybrid films to be ideal electrode supports for deposition of large amounts of electrochemically active materials per unit area. To demonstrate the concept, asymmetric supercapacitors that are flexible was successfully fabricated based on GF/CNT supports. In Chap. 5, a new concept was proposed for designing flexible Nickel/Iron battery based on GF/CNTs hybrid films. The assembled prototypes display enhanced electrochemical performance and bridge the gap between supercapacitors and batteries, demonstrating great practical significance.

References

1. Y.S. Meng, M. Elena Arroyo-de Dompablo, Recent advances in first principles computational research of cathode materials for lithium-ion batteries. Acc. Chem. Res. **46**, 1171–1180 (2013)
2. K. Naoi, W. Naoi, S. Aoyagi, J.-I. Miyamoto, T. Kamino, New generation "nanohybrid supercapacitor". Acc. Chem. Res. **46**, 1075–1083 (2013)
3. J.M. Tarascon, M. Armand, Issues and challenges facing rechargeable lithium batteries. Nature **414**, 359–367 (2001)
4. I. Hadjipaschalis, A. Poullikkas, V. Efthimiou, Overview of current and future energy storage technologies for electric power applications. Renew. Sustain. Energy Rev. **13**, 1513–1522 (2009)
5. S.M.G. Mousavi, M. Nikdel, Various battery models for various simulation studies and applications. Renew. Sustain. Energy Rev. **32**, 477–485 (2014)
6. B. Dunn, H. Kamath, J.-M. Tarascon, Electrical energy storage for the grid: a battery of choices. Science **334**, 928–935 (2011)
7. U.S.E.I. Administration, *International Energy Outlook* (2013), p. EIA-0484
8. I.E. Agency, *World Energy Outlook* (International Energy Agency, Russia 2013)
9. Z. Yang, J. Zhang, M.C.W. Kintner-Meyer, X. Lu, D. Choi, J.P. Lemmon, J. Liu, Electrochemical energy storage for green grid. Chem. Rev. **111**, 3577–3613 (2011)
10. H. Kim, J. Hong, K.-Y. Park, H. Kim, S.-W. Kim, K. Kang, Aqueous rechargeable Li and Na ion batteries. Chem. Rev. (2014)
11. G.L. Soloveichik, Battery technologies for large-scale stationary energy storage, in *Annual Review of Chemical and Biomolecular Engineering*, ed. by J.M. Prausnitz, vol. 22011, pp. 503–527
12. E.S. Association, Energy Storage Association, 2014. http://energystorage.org/
13. I.Z.J.I. San Martin, J.J. San Martin, V. Aperribay, P. Eguia, *European Association for the Development of Renewable Energies* (Environment and Power Quality 2011)
14. V. Augustyn, P. Simon, B. Dunn, Pseudocapacitive oxide materials for high-rate electrochemical energy storage. Energy Environ. Sci. **7**, 1597–1614 (2014)
15. H.E. Becker, U.S. Patent US2800616, 1957
16. P.J. Hall, M. Mirzaeian, S.I. Fletcher, F.B. Sillars, A.J.R. Rennie, G.O. Shitta-Bey, G. Wilson, A. Cruden, R. Carter, Energy storage in electrochemical capacitors: designing functional materials to improve performance. Energy Environ. Sci. **3**, 1238–1251 (2010)
17. R. Kotz, M. Carlen, Principles and applications of electrochemical capacitors. Electrochim. Acta **45**, 2483–2498 (2000)
18. B.E. Conway, W.G. Pell, Double-layer and pseudocapacitance types of electrochemical capacitors and their applications to the development of hybrid devices. J. Solid State Electrochem. **7**, 637–644 (2003)
19. B.E. Conway, Transition from supercapacitor to battery behavior in electrochemical energy-storage. J. Electrochem. Soc. **138**, 1539–1548 (1991)
20. P. Simon, Y. Gogotsi, B. Dunn, Where do batteries end and supercapacitors begin? Science **343**, 1210–1211 (2014)
21. M.D. Stoller, R.S. Ruoff, Best practice methods for determining an electrode material's performance for ultracapacitors. Energy Environ. Sci. **3**, 1294–1301 (2010)
22. A.K. Shukla, S. Sampath, K. Vijayamohanan, Electrochemical supercapacitors: energy storage beyond batteries. Curr. Sci. **79**, 1656–1661 (2000)
23. D.C. Grahame, The electrical double layer and the theory of electrocapillarity. Chem. Rev. **41**, 441–501 (1947)
24. G.Z. Chen, Understanding supercapacitors based on nano-hybrid materials with interfacial conjugation. Progr. Nat. Sci. –Mater. Int. **23**, 245–255 (2013)
25. P. Simon, Y. Gogotsi, Capacitive energy storage in nanostructured carbon-electrolyte systems. Acc. Chem. Res. **46**, 1094–1103 (2013)

26. B.E. Conway, 2-Dimensional and quasi-2-dimensional isotherms for Li intercalation and UPD processes at surfaces. Electrochim. Acta **38**, 1249–1258 (1993)
27. B.E. Conway, Electrochemical surface science—the study of monolayers of ad-atoms and solvent molecules at charged metal interfaces. Prog. Surf. Sci. **16**, 1–137 (1984)
28. J.S. Wang, L.A. University of California, *Pseudocapacitive Effects in Nanostructured Transition Metal Oxide Materials* (University of California, Los Angeles, 2008)
29. F.G. Will, C.A. Knorr, Untersuchung des aufbaues und abbaues von wasserstoffbelegungen und sauerstoffbelegungen an platin mit einer neuen instationaren methode. Zeitschrift Fur Elektrochemie **64**, 258–269 (1960)
30. K. Engelsmann, W.J. Lorenz, E. Schmidt, Underpotential deposition of lead on polycrystalline and single-crystal gold surfaces. 1. Thermodynamics. J. Electroanal. Chem. **114**, 1–10 (1980)
31. S. Hadzijordanov, H. Angersteinkozlowska, B.E. Conway, Surface oxidation and H deposition at ruthenium electrodes—resolution of component processes in potential-sweep experiments. J. Electroanal. Chem. **60**, 359–362 (1975)
32. B.E. Conway, Electrochemical oxide film formation at noble metals as a surface-chemical process. Prog. Surf. Sci. **49**, 331–452 (1995)
33. J.L. Liu, J. Sun, L.A. Gao, A promising way to enhance the electrochemical behavior of flexible single-walled carbon nanotube/polyaniline composite films. J. Phys. Chem. C **114**, 19614–19620 (2010)
34. J.P. Zheng, T.R. Jow, A new charge storage mechanism for electrochemical capacitors. J. Electrochem. Soc. **142**, L6–L8 (1995)
35. M. Toupin, T. Brousse, D. Belanger, Charge storage mechanism of MnO2 electrode used in aqueous electrochemical capacitor. Chem. Mater. **16**, 3184–3190 (2004)
36. J. Tanguy, M. Hoclet, Analysis of the redox mechanism of conducting polymers derived from impedance, cyclic voltammetry and electrochemical voltage spectroscopy. Synth. Met. **43**, 2995–2999 (1991)
37. K. Doblhofer, C. Zhong, The mechanism of electrochemical charge - transfer reactions on conducting polymer films. Synth. Met. **43**, 2865–2870 (1991)
38. F. Béguin, V. Presser, A. Balducci, E. Frackowiak, Carbons and electrolytes for advanced supercapacitors. Adv. Mater. **26**, 2219–2251 (2014)
39. G. Lota, K. Fic, E. Frackowiak, Carbon nanotubes and their composites in electrochemical applications. Energy Environ. Sci. **4**, 1592–1605 (2011)
40. V. Khomenko, E. Frackowiak, F. Béguin, Determination of the specific capacitance of conducting polymer/nanotubes composite electrodes using different cell configurations. Electrochim. Acta **50**, 2499–2506 (2005)
41. C. Xu, J. Sun, L. Gao, Synthesis of novel hierarchical graphene/polypyrrole nanosheet composites and their superior electrochemical performance. J. Mater. Chem. **21**, 11253–11258 (2011)
42. M. Ghidiu, M.R. Lukatskaya, M.-Q. Zhao, Y. Gogotsi, M.W. Barsoum, Conductive two-dimensional titanium carbide/clay/with high volumetric capacitance. Nature **516**, 78–81 (2014)
43. M.R. Lukatskaya, O. Mashtalir, C.E. Ren, Y. Dall'Agnese, P. Rozier, P.L. Taberna, M. Naguib, P. Simon, M.W. Barsoum, Y. Gogotsi, Cation intercalation and high volumetric capacitance of two-dimensional titanium carbide. Science **341**, 1502–1505 (2013)
44. M.R. Lukatskaya, S.-M. Bak, X. Yu, X.-Q. Yang, M.W. Barsoum, Y. Gogotsi, Probing the mechanism of high capacitance in 2D titanium carbide using in situ X-Ray absorption spectroscopy. Adv. Energy Mater. **5** (2015)
45. B.E. Conway, *Electrochemical Supercapacitors-Scientific Fundamentals and Technological Applications* (Springer Science + Business Media, New York, 1999)
46. M. Winter, R.J. Brodd, What are batteries, fuel cells, and supercapacitors? Chem. Rev. **104**, 4245–4269 (2004)
47. M. Technologies, 10073627, 1–12, (2009)

48. A. Chu, P. Braatz, Comparison of commercial supercapacitors and high-power lithium-ion batteries for power-assist applications in hybrid electric vehicles I. Initial characterization. J. Power Sources **112**, 236–246 (2002)
49. A. Burke, *Institute of Transportation Studies* (University of California, Davis, 2009
50. K.R. Cooper, M. Smith, Electrical test methods for on-line fuel cell ohmic resistance measurement. J. Power Sources **160**, 1088–1095 (2006)
51. Autolab, Part 2-Measurement. http://www.ecochemie.nl/Applications/2011
52. T.E. Springer, T.A. Zawodzinski, M.S. Wilson, S. Gottesfeld, Characterization of polymer electrolyte fuel cells using AC impedance spectroscopy. J. Electrochem. Soc. **143**, 587–599 (1996)
53. M.C. Lefebvre, R.B. Martin, P.G. Pickup, Characterization of ionic conductivity profiles within proton exchange membrane fuel cell gas diffusion electrodes by impedance spectroscopy. Electrochem. Solid State Lett. **2**, 259–261 (1999)
54. Q.Z. Guo, M. Cayetano, Y.M. Tsou, E.S. De Castro, R.E. White, Study of ionic conductivity profiles of the air cathode of a PEMFC by AC impedance spectroscopy. J. Electrochem. Soc. **150**, A1440–A1449 (2003)
55. R. Makharia, M.F. Mathias, D.R. Baker, Measurement of catalyst layer electrolyte resistance in PEFCs using electrochemical impedance spectroscopy. J. Electrochem. Soc. **152**, A970–A977 (2005)
56. H. Angersteinkozlowska, B.E. Conway, Evaluation of rate constants and reversibility parameters for surface-reactions by the potential-sweep method. J. Electroanal. Chem. **95**, 1–28 (1979)
57. H. Angersteinkozlowska, J. Klinger, B.E. Conway, Computer-simulation of kinetic-behavior of surface-reactions driven by a linear potential sweep. 2. Sequential reactions of adsorbed species. J. Electroanal. Chem. **75**, 61–75 (1977)
58. H. Angersteinkozlowska, J. Klinger, B.E. Conway, Computer-simulation of kinetic-behavior of surface-reactions driven by a linear potential sweep. 1. Model 1-electron reaction with a single adsorbed species. J. Electroanal. Chem. **75**, 45–60 (1977)
59. Y.G. Wang, H.Q. Li, Y.Y. Xia, Ordered whiskerlike polyaniline grown on the surface of mesoporous carbon and its electrochemical capacitance performance. Adv. Mater. **18**, 2619–2623 (2006)
60. B. Yan, J. Yang, Y. Li, R. Qian, Cyclic voltammetry of polypyrrole in anhydrous acetonitrile. Synth. Met. **58**, 17–27 (1993)
61. Z. Feng, D. Mo, W. Zhou, Q. Zhou, J. Xu, B. Lu, S. Zhen, Z. Wang, X. Ma, Electrosynthesis and electrochemical capacitive behavior of a new nitrogen PEDOT analogue-based polymer electrode. New J. Chem. **40**, 2304–2314 (2016)
62. Q. Mahmood, W.S. Kim, H.S. Park, Structure and compositional control of MoO3 hybrids assembled by nanoribbons for improved pseudocapacitor rate and cycle performance. Nanoscale **4**, 7855–7860 (2012)
63. L. Li, S. Peng, H.B. Wu, L. Yu, S. Madhavi, X.W. Lou, A flexible quasi-solid-state asymmetric electrochemical capacitor based on hierarchical porous V2O5 nanosheets on carbon nanofibers. Adv. Energy Mater. **5** (2015)
64. L. Kong, C. Zhang, J. Wang, W. Qiao, L. Ling, D. Long, Free-standing T-Nb2O5/graphene composite papers with ultrahigh gravimetric/volumetric capacitance for Li-Ion intercalation pseudocapacitor. ACS Nano **9**, 11200–11208 (2015)
65. S. Trasatti, G. Buzzanca, Ruthenium dioxide—new interesting electrode material—solid state structure and electrochemical behaviour. J. Electroanal. Chem. **29**, A1–000 (1971)
66. D. Galizzio, F. Tantardi, S. Trasatti, Ruthenium dioxide—new electrode material. 1. Behavior in acid solutions of inert electrolytes. J. Appl. Electrochem. **4**, 57–67 (1974)
67. D.M. MacArthur, The proton diffusion coefficient for the nickel hydroxide electrode. J. Electrochem. Soc. **117**, 729–733 (1970)
68. J. Wang, J. Polleux, J. Lim, B. Dunn, Pseudocapacitive contributions to electrochemical energy storage in TiO2 (anatase) nanoparticles. J. Phys. Chem. C **111**, 14925–14931 (2007)

69. M. Sathiya, A.S. Prakash, K. Ramesha, J.M. Tarascon, A.K. Shukla, V2O5-anchored carbon nanotubes for enhanced electrochemical energy storage. J. Am. Chem. Soc. **133**, 16291–16299 (2011)
70. J. Come, P.L. Taberna, S. Hamelet, C. Masquelier, P. Simon, Electrochemical kinetic study of LiFePO4 using cavity microelectrode. J. Electrochem. Soc. **158**, A1090–A1093 (2011)
71. H. Lindstrom, S. Sodergren, A. Solbrand, H. Rensmo, J. Hjelm, A. Hagfeldt, S.E. Lindquist, Li + ion insertion in TiO2 (anatase). 2. Voltammetry on nanoporous films. J. Phys. Chem. B **101**, 7717–7722 (1997)
72. V. Augustyn, J. Come, M.A. Lowe, J.W. Kim, P.-L. Taberna, S.H. Tolbert, H.D. Abruna, P. Simon, B. Dunn, High-rate electrochemical energy storage through Li + intercalation pseudocapacitance. Nat. Mater. **12**, 518–522 (2013)
73. L.R. Faulkner, A.J. Bard, *Electrochemical Method: Fundamentals and Applications*, 2nd edn. (Wiley, New York, 2001)
74. T.C. Liu, W.G. Pell, B.E. Conway, S.L. Roberson, Behavior of molybdenum nitrides as materials for electrochemical capacitors—comparison with ruthenium oxide. J. Electrochem. Soc. **145**, 1882–1888 (1998)
75. W. Yan, J.Y. Kim, W. Xing, K.C. Donavan, T. Ayvazian, R.M. Penner, Lithographically patterned gold/manganese dioxide core/shell nanowires for high capacity, high rate, and high cyclability hybrid electrical energy storage. Chem. Mater. **24**, 2382–2390 (2012)
76. J. Duay, S.A. Sherrill, Z. Gui, E. Gillette, S.B. Lee, Self-limiting electrodeposition of hierarchical MnO2 and M(OH)(2)/MnO2 nanofibril/nanowires: mechanism and supercapacitor properties. ACS Nano **7**, 1200–1214 (2013)
77. K. Zhu, Q. Wang, J.-H. Kim, A.A. Pesaran, A.J. Frank, Pseudocapacitive lithium-ion storage in oriented anatase TiO2 nanotube arrays. J. Phys. Chem. C **116**, 11895–11899 (2012)
78. T. Brezesinski, J. Wang, S.H. Tolbert, B. Dunn, Ordered mesoporous alpha-MoO3 with iso-oriented nanocrystalline walls for thin-film pseudocapacitors. Nat. Mater. **9**, 146–151 (2010)
79. T. Brezesinski, J. Wang, R. Senter, K. Brezesinski, B. Dunn, S.H. Tolbert, On the correlation between mechanical flexibility, nanoscale structure, and charge storage in periodic mesoporous CeO2 thin films. ACS Nano **4**, 967–977 (2010)
80. S. Ardizzone, G. Fregonara, S. Trasatti, Inner and outer active surface of RuO2 electrodes. Electrochim. Acta **35**, 263–267 (1990)
81. K. Brezesinski, J. Wang, J. Haetge, C. Reitz, S.O. Steinmueller, S.H. Tolbert, B.M. Smarsly, B. Dunn, T. Brezesinski, Pseudocapacitive contributions to charge storage in highly ordered mesoporous group V transition metal oxides with iso-oriented layered nanocrystalline domains. J. Am. Chem. Soc. **132**, 6982–6990 (2010)
82. J.-B. Jorcin, M.E. Orazem, N. Pébère, B. Tribollet, CPE analysis by local electrochemical impedance spectroscopy. Electrochim. Acta **51**, 1473–1479 (2006)
83. R.H. Nilson, M.T. Brumbach, B.C. Bunker, Modeling the electrochemical impedance spectra of electroactive pseudocapacitor materials. J. Electrochem. Soc. **158**, A678–A688 (2011)
84. S. Zhao, F. Wu, L. Yang, L. Gao, A.F. Burke, A measurement method for determination of dc internal resistance of batteries and supercapacitors. Electrochem. Commun. **12**, 242–245 (2010)
85. J.B. Goodenough, Evolution of strategies for modern rechargeable batteries. Acc. Chem. Res. **46**, 1053–1061 (2013)
86. J.B. Goodenough, K.-S. Park, The Li-Ion rechargeable battery: a perspective. J. Am. Chem. Soc. **135**, 1167–1176 (2013)
87. J.B. Goodenough, Electrochemical energy storage in a sustainable modern society. Energy Environ. Sci. **7**, 14–18 (2014)
88. R. Fong, U. Vonsacken, J.R. Dahn, Studies of lithium intercalation into carbons using nonaqueous electrochemical-cells. J. Electrochem. Soc. **137**, 2009–2013 (1990)
89. C.H. Hamann, A. Hamnett, W. Vielstich, *Electrochemistry*, 2nd edn. (Wiley-VCH, Weinheim, 2007) (updated edn. 2007)

90. A. Nyman, T.G. Zavalis, R. Elger, M. Behm, G. Lindbergh, Analysis of the polarization in a Li-Ion battery cell by numerical simulations. J. Electrochem. Soc. **157**, A1236–A1246 (2010)
91. M. Gaberscek, J. Moskon, B. Erjavec, R. Dominko, J. Jamnik, The importance of interphase contacts in Li Ion electrodes: the meaning of the high-frequency impedance arc. Electrochem. Solid-State Lett. **11**, A170–A174 (2008)
92. M. Doyle, J.P. Meyers, J. Newman, Computer simulations of the impedance response of lithium rechargeable batteries. J. Electrochem. Soc. **147**, 99–110 (2000)
93. A.K. Geim, Graphene: status and prospects. Science **324**, 1530–1534 (2009)
94. C. Lee, X.D. Wei, J.W. Kysar, J. Hone, Measurement of the elastic properties and intrinsic strength of monolayer graphene. Science **321**, 385–388 (2008)
95. K.I. Bolotin, K.J. Sikes, Z. Jiang, M. Klima, G. Fudenberg, J. Hone, P. Kim, H.L. Stormer, Ultrahigh electron mobility in suspended graphene. Solid State Commun. **146**, 351–355 (2008)
96. A.A. Balandin, S. Ghosh, W.Z. Bao, I. Calizo, D. Teweldebrhan, F. Miao, C.N. Lau, Superior thermal conductivity of single-layer graphene. Nano Lett. **8**, 902–907 (2008)
97. S. Bae, H. Kim, Y. Lee, X.F. Xu, J.S. Park, Y. Zheng, J. Balakrishnan, T. Lei, H.R. Kim, Y. I. Song, Y.J. Kim, K.S. Kim, B. Ozyilmaz, J.H. Ahn, B.H. Hong, S. Iijima, Roll-to-roll production of 30-inch graphene films for transparent electrodes. Nat. Nanotechnol. **5**, 574–578 (2010)
98. X. Wang, L. Zhi, K. Muellen, Transparent, conductive graphene electrodes for dye-sensitized solar cells. Nano Lett. **8**, 323–327 (2008)
99. M. Pumera, Electrochemistry of graphene: new horizons for sensing and energy storage. Chem. Rec. **9**, 211–223 (2009)
100. D.A.C. Brownson, D.K. Kampouris, C.E. Banks, An overview of graphene in energy production and storage applications. J. Power Sources **196**, 4873–4885 (2011)
101. Y.Q. Sun, Q.O. Wu, G.Q. Shi, Graphene based new energy materials. Energy Environ. Sci. **4**, 1113–1132 (2011)
102. C.N.R. Rao, A.K. Sood, K.S. Subrahmanyam, A. Govindaraj, Graphene: the new two-dimensional nanomaterial. Angew. Chem.-Int. Edit. **48**, 7752–7777 (2009)
103. K.S. Novoselov, A.K. Geim, S.V. Morozov, D. Jiang, Y. Zhang, S.V. Dubonos, I.V. Grigorieva, A.A. Firsov, Electric field effect in atomically thin carbon films. Science **306**, 666–669 (2004)
104. M. Pumera, Graphene-based nanomaterials and their electrochemistry. Chem. Soc. Rev. **39**, 4146–4157 (2010)
105. K.V. Emtsev, A. Bostwick, K. Horn, J. Jobst, G.L. Kellogg, L. Ley, J.L. McChesney, T. Ohta, S.A. Reshanov, J. Rohrl, E. Rotenberg, A.K. Schmid, D. Waldmann, H.B. Weber, T. Seyller, Towards wafer-size graphene layers by atmospheric pressure graphitization of silicon carbide. Nat. Mater. **8**, 203–207 (2009)
106. X.S. Li, W.W. Cai, J.H. An, S. Kim, J. Nah, D.X. Yang, R. Piner, A. Velamakanni, I. Jung, E. Tutuc, S.K. Banerjee, L. Colombo, R.S. Ruoff, Large-area synthesis of high-quality and uniform graphene films on copper foils. Science **324**, 1312–1314 (2009)
107. S. Park, R.S. Ruoff, Chemical methods for the production of graphenes. Nat. Nanotechnol. **4**, 217–224 (2009)
108. C.Y. Su, Y.P. Xu, W.J. Zhang, J.W. Zhao, A.P. Liu, X.H. Tang, C.H. Tsai, Y.Z. Huang, L. J. Li, Highly efficient restoration of graphitic structure in graphene oxide using alcohol vapors. ACS Nano **4**, 5285–5292 (2010)
109. Y. Hernandez, V. Nicolosi, M. Lotya, F.M. Blighe, Z.Y. Sun, S. De, I.T. McGovern, B. Holland, M. Byrne, Y.K. Gun'ko, J.J. Boland, P. Niraj, G. Duesberg, S. Krishnamurthy, R. Goodhue, J. Hutchison, V. Scardaci, A.C. Ferrari, J.N. Coleman, High-yield production of graphene by liquid-phase exfoliation of graphite. Nat. Nanotechnol. **3**, 563–568 (2008)

110. J.N. Coleman, Liquid-phase exfoliation of nanotubes and graphene. Adv. Funct. Mater. **19**, 3680–3695 (2009)
111. X. Cui, C.Z. Zhang, R. Hao, Y.L. Hou, Liquid-phase exfoliation, functionalization and applications of graphene. Nanoscale **3**, 2118–2126 (2011)
112. A.G. Cano-Marquez, F.J. Rodriguez-Macias, J. Campos-Delgado, C.G. Espinosa-Gonzalez, F. Tristan-Lopez, D. Ramirez-Gonzalez, D.A. Cullen, D.J. Smith, M. Terrones, Y.I. Vega-Cantu, Ex-MWNTs: graphene sheets and ribbons produced by lithium intercalation and exfoliation of carbon nanotubes. Nano Lett. **9**, 1527–1533 (2009)
113. D.V. Kosynkin, A.L. Higginbotham, A. Sinitskii, J.R. Lomeda, A. Dimiev, B.K. Price, J.M. Tour, Longitudinal unzipping of carbon nanotubes to form graphene nanoribbons. Nature **458**, U872–U875 (2009)
114. Z. Li, Y.G. Yao, Z.Y. Lin, K.S. Moon, W. Lin, C.P. Wong, Ultrafast, dry microwave synthesis of graphene sheets. J. Mater. Chem. **20**, 4781–4783 (2010)
115. J. Lu, J.X. Yang, J.Z. Wang, A.L. Lim, S. Wang, K.P. Loh, One-pot synthesis of fluorescent carbon nanoribbons, nanoparticles, and graphene by the exfoliation of graphite in ionic liquids. ACS Nano **3**, 2367–2375 (2009)
116. C.Y. Su, A.Y. Lu, Y.P. Xu, F.R. Chen, A.N. Khlobystov, L.J. Li, High-quality thin graphene films from fast electrochemical exfoliation. ACS Nano **5**, 2332–2339 (2011)
117. J.Z. Wang, K.K. Manga, Q.L. Bao, K.P. Loh, High-yield synthesis of few-layer graphene flakes through electrochemical expansion of graphite in propylene carbonate electrolyte. J. Am. Chem. Soc. **133**, 8888–8891 (2011)
118. J.B. Hou, Y.Y. Shao, M.W. Ellis, R.B. Moore, B.L. Yi, Graphene-based electrochemical energy conversion and storage: fuel cells, supercapacitors and lithium ion batteries. Phys. Chem. Chem. Phys. **13**, 15384–15402 (2011)
119. C. Xu, B. Xu, Y. Gu, Z. Xiong, J. Sun, X.S. Zhao, Graphene-based electrodes for electrochemical energy storage. Energy Environ. Sci. **6**, 1388–1414 (2013)
120. H. Gwon, H.-S. Kim, K.U. Lee, D.-H. Seo, Y.C. Park, Y.-S. Lee, B.T. Ahn, K. Kang, Flexible energy storage devices based on graphene paper. Energy Environ. Sci. **4**, 1277–1283 (2011)
121. G. Zhou, F. Li, H.-M. Cheng, Progress in flexible lithium batteries and future prospects. Energy Environ. Sci. **7**, 1307–1338 (2014)
122. N. Li, Z. Chen, W. Ren, F. Li, H.-M. Cheng, Flexible graphene-based lithium ion batteries with ultrafast charge and discharge rates. Proc. Natl. Acad. Sci. **109**, 17360–17365 (2012)
123. V.L. Pushparaj, M.M. Shaijumon, A. Kumar, S. Murugesan, L. Ci, R. Vajtai, R.J. Linhardt, O. Nalamasu, P.M. Ajayan, Flexible energy storage devices based on nanocomposite paper. Proc. Natl. Acad. Sci. U.S.A. **104**, 13574–13577 (2007)
124. C. Ban, Z. Wu, D.T. Gillaspie, L. Chen, Y. Yan, J.L. Blackburn, A.C. Dillon Nanostructured Fe3O4/SWNT Electrode: binder-free and high-rate Li-Ion anode. Adv. Mater. **22**, E145 (2010)
125. B. Liu, J. Zhang, X. Wang, G. Chen, D. Chen, C. Zhou, G. Shen, Hierarchical three-dimensional ZnCo2O4 nanowire arrays/carbon cloth anodes for a novel class of high-performance flexible lithium-ion batteries. Nano Lett. **12**, 3005–3011 (2012)
126. B. Liu, X. Wang, B. Liu, Q. Wang, D. Tan, W. Song, X. Hou, D. Chen, G. Shen, Advanced rechargeable lithium-ion batteries based on bendable ZnCo2O4-urchins-on-carbon-fibers electrodes. Nano Res. **6**, 525–534 (2013)
127. L. Hu, N. Liu, M. Eskilsson, G. Zheng, J. McDonough, L. Wagberg, Y. Cui, Silicon-conductive nanopaper for Li-ion batteries. Nano Energy **2**, 138–145 (2013)
128. J. Luo, J. Liu, Z. Zeng, C.F. Ng, L. Ma, H. Zhang, J. Lin, Z. Shen, H.J. Fan, Three-dimensional graphene foam supported Fe3O4 lithium battery anodes with long cycle life and high rate capability. Nano Lett. **13**, 6136–6143 (2013)

129. H. Ji, L. Zhang, M.T. Pettes, H. Li, S. Chen, L. Shi, R. Piner, R.S. Ruoff, Ultrathin graphite foam: a three-dimensional conductive network for battery electrodes. Nano Lett. **12**, 2446–2451 (2012)
130. X. Dong, X. Wang, J. Wang, H. Song, X. Li, L. Wang, M.B. Chan-Park, C.M. Li, P. Chen, Synthesis of a MnO2–graphene foam hybrid with controlled MnO2 particle shape and its use as a supercapacitor electrode. Carbon **50**, 4865–4870 (2012)

Chapter 2
Electrochemical Exfoliation Synthesis of Graphene

The synthesis of graphene in both high quality and quantity *via* economic ways is highly desirable and meaningful for practical applications. Here a facile, environmentally-friendly and cost-effective multiple electrochemical exfoliation approach has been developed for the synthesis of high quality graphene flakes with high yield by using graphite rod from spent zinc-carbon/pencil core as carbon source. Various protonic acid (i.e H_2SO_4, H_3PO_4 or $H_2C_2O_4$) aqueous solution were chosen as electrolyte. The unique cell configuration enables multiple exfoliation process to improve both the quality and yield of graphene sheets. After nitrogen doping, the exfoliated graphene flakes process good electrocatalytic activity, stability and toxicity tolerance for alkaline solution-based oxygen reduction reaction.

2.1 Introduction

Since the first fabrication of single-sheet graphene through micromechanical cleavage of bulk graphite was reported [1], numbers of methods have been developed for generating graphene with high quality and low cost. Micromechanical cleavage [1], chemical vapor deposition (CVD) [2, 3] and epitaxial growth [4] produce graphene with high crystal quality but they are impractical for commercial applications due to low production rate and relatively high cost. Chemical exfoliation of graphene based on Brodie, Staudenmaier and Hummers methods, which involves the oxidation of graphite with oxidants and strong acids, and the subsequent chemical or thermal reduction, is advantageous in terms of low cost and controllable solution-processing [5]. However, this method employs some hazardous chemicals (e.g., H_2SO_4-$KMnO_4$, hydrazine) which are environmentally harmful and the production process is time-consuming [6]. Recently, electrochemical exfoliation of various carbon precursors, including graphite rods, carbon papers or HOPG, has been demonstrated to be an effective approach for generating graphene. Using

J. Liu, *Graphene-Based Composites for Electrochemical Energy Storage*,
Springer Theses, DOI 10.1007/978-981-10-3388-9_2

graphite rods as electrodes and ionic-liquid/water solution as electrolyte, Ionic liquid functionalized graphene sheets have been prepared *via* a one-step electrochemical approach [7]. Lu et al. [8] performed a detailed study and proposed a mechanism for the electrochemical exfoliation of graphite in ionic liquid solution, which involves (i) anodic oxidation of water, (ii) hydroxylation or oxidation of graphite edge planes, (iii) intercalation by ionic liquid anions between graphite layers, forming the graphite-intercalation-compounds (GICs), and (iv) oxidative cleavage and precipitation of the GICs. Inspired by the electrochemical reactions between graphite anode and organic carbonates in lithium ion batteries, Wang et al. [9] successfully prepared graphene flakes with few-layer *via* electrochemical exfoliation of graphite in propylene carbonate (electrolyte). The solvation nature of the bulky organic ions or molecules facilitate the intercalation process and the expansion of graphene layers. However, the organic compounds are sensitive to moisture and oxygen and the reactions always take a long reaction time. All these impede their practical applications. In the past few decades metal chlorides, strong protonic acids and other inorganic reagents have been the most promising "invaders" for graphite intercalation [10]. The expansion of graphite sheets in these intercalated compounds was realized by violent releasing of gases via fast heating. Very recently electric power has been used to drive the expansion and exfoliation of sulfate-intercalated graphite. In an electrochemical cell using protonic acid aqueous solution as electrolyte Su et al. [11] applied a relatively high (10 V) voltage to graphite anode for the synthesis of graphene sheets. Among many different electrolytes examined, including HBr, HCl, HNO_3, and H_2SO_4, only H_2SO_4 exhibits ideal exfoliation efficiency from natural graphite flake or highly oriented pyrolytic graphite. In Su's paper the anode (graphite) and cathode (Pt) were placed parallel with a separation of a few cm away. Similarly almost all the reported electrochemical cells for graphite exfoliation are in the parallel configuration.

Herein an improved synthesis of high-quality graphene is demonstrated in a vertical cell configuration *via* multiple electrochemical exfoliation of graphite rod [12]. Unlike previous reports, the unique cell configuration adopted here enables multiple exfoliation processes to improve both the quality and yield of graphene sheets. The mechanism of multiple electrochemical exfoliation of spent graphite rod was discussed in detail, the experiment conditions were optimized, and the structure and electrocatalytic activity of the resultant sample were investigated.

2.2 Experiment and Characterization

2.2.1 Material Synthesis

Synthesis of Graphene Flakes. Graphene flakes were prepared *via* multiple electrochemical exfoliation (MEE) approach. Briefly, graphite rod from spent Zinc-Carbon dry cells was utilized as positive electrode and the carbon source.

The anode (graphite rod) and cathode (platinum wire) were placed at the bottom and top of the electrochemical cell, respectively, with protonic acid (e.g. H_2SO_4, H_3PO_4 or $H_2C_2O_4$) aqueous solution as electrolyte. The electrochemical exfoliation process was ignited upon the application of a certain voltage across the electrodes. The water soluble graphene flakes were ultrasonicated, washed, dried and collected. Control experiments were also conducted *via* conventional (parallel) electrochemical configuration.

Synthesis of Nitrogen-doped Graphene Flakes. The as-prepared graphene flakes were annealed at 800 °C for 1 h under the flow of Ar/NH_3 (95/5, v/v, 400 sccm), to achieve the N-doped graphene.

2.2.2 Material Characterization

Structure and Morphology Characterization. The morphology was investigated *via* Scanning Electron Microscopy (SEM), Transmission Electron Microscopy (TEM, JEM-2010, 200 kV), Optical Microscopy and Atomic Force Microscopy (AFM, Nanoscope V, diDimension). Fourier transform infrared spectroscopy (FTIR) (Perkin Elmer 2000 FTIR spectrometer), Thermogravimetric Analysis (TGA) and X-ray photoelectron spectroscopy (XPS) [VG ESCALAB 250 spectrometer (Thermo Electron, Altrincham, U.K.), using an Al $K\propto$ X-ray source (1486 eV)] were used to shed more light on chemical composition information.

Electrochemical Performance Evaluation. Rotating disk electrode (RDE) and Cyclic voltammerty (CV) measurements were conducted in a standard three-electrode system (platinum foil-counter electrode, Ag/AgCl electrode-the reference electrode, Graphene-working electrode). The working electrode was prepared as follows [13]: (i) 10 mg of N-doped graphene was ultrasonically dispersed into1 ml of 2-propanl containing Nafion solution (5 wt%, dupont); (ii) 10 μl of the catalyst ink was coated on the glassy carbon disk (5 mm in diameter) and dried at 80 °C for 15 min. As-prepared graphene, pt-loaded carbon catalyst (Pt/C 20% on Vulcan XC-72R, E-TEK division, PeMEAS Fuel Cell Technology) with the same amount, and the bare glassy carbon electrode were tested for comparison. Methanol toxicity test was conducted at a constant potential −0.5 V (vs. Ag/AgCl). The voltammertic stability tests were performed in O_2-saturated 0.1 M KOH within the potential window of −1.0–0.2 V (vs. Ag/AgCl) for 20,000 cycles. The sweep rate is 100 mV/s. All measurements were carried out at room temperature. All potentials presented in the graphs and in the discussion were calibrated with reference to the reversible hydrogen electrode (RHE), which is independent of pH value. The number of electron transferred (n) was calculated based on Koutecky-Levich equation.

2.3 Results and Discussions

2.3.1 The Synthesis of Graphene Flakes

Different from conventional parallel two-electrode electrochemical cell, in our design graphite rod obtained from spent Zn–C primary battery (anode) and platinum wire (cathode) were placed vertically at the bottom and top of the electrochemical cell, respectively. The graphite rod was surrounded with a plastic tube and only the top surface of it was exposed to the electrolyte solution. A constant current of 0.1A was applied across the two electrodes. The potential of 6–8 V could drive the anions into the intercalation space and make the exfoliation to proceed. Comparative experiment was also conducted *via* conventional method. An apparent colour change for the aqueous electrolyte solution from transparent to dark was observed in vertical cell after only few minutes. This response time is much shorter than that of conventional method, indicating the exfoliation process in the vertical configuration is more efficient. In the same reaction time period, significantly larger quantity of graphene sheets were collected, benefiting from the multiple electrochemical exfoliation feature in our design. More details about the underlying mechanism will be discussed later.

The morphological and structural properties of the resultant samples were investigated by TEM, AFM and Optical microscopy. TEM and optical images reveal that the as-prepared products consist of a large amount of exfoliated graphene with lateral size ranging from 1 to few μm (Fig. 2.1a, c and d). The exfoliated graphene flakes with thickness of 4.84 nm are identified (Fig. 2.1b). Based on the statistical AFM mapping of exfoliated graphene flakes, approximately 32% of the graphene flakes have thicknesses in the range of 4–6 nm while nearly 80% of them are located in the thickness range of 4–8 nm (Fig. 2.1d). In addition, the total yield of graphene flakes is nearly ~50%, which is two folds of that of the control design.

FT-IR, XPS, and Thermogravimetric analysis (TGA) were employed to shed more light on the element information of the resultant samples. The presence of various functional groups including C–O (at 1060 cm^{-1}), C–O–C (1250 cm^{-1}), C=O/COO (at 1690–1710 cm^{-1}), and COO–H/CO–H (1365 cm^{-1}) [14] was observed (Fig. 2.2a). These functional groups can be eliminated by heating. The weight loss at ~100 °C in TGA (Fig. 2.2b) is due to the vaporization of adsorbed moisture or water. There is a major weight loss that starts at ~150 °C and continues up to 800 °C, which certainly results from the decomposition of functional groups. More significant loss for "MEE" graphene than "SEE" one (30% wt. vs. 20% wt.) indicates there are less functional groups on the "SEE" sample [15]. The presence of oxygen functional groups is further verified by XPS C1 s spectra

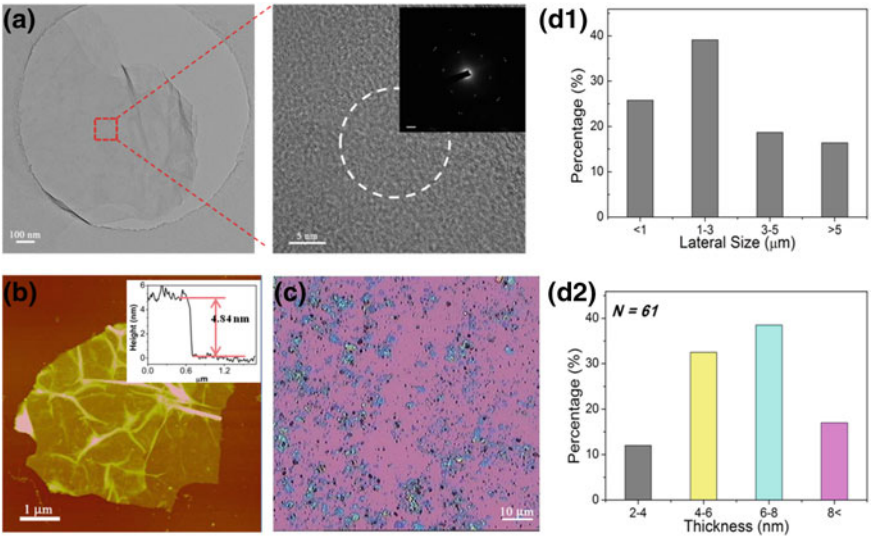

Fig. 2.1 **a** TEM image and corresponding selected area electron diffraction pattern of the multiple electrochemical exfoliation (MEE) graphene flakes. **b** AFM image of exfoliated graphene flakes spin-coated onto a SiO_2 (285 nm)/Si substrate. The thickness is ~4.84 nm, corresponding to 10–15 layers. **c** The low-magnification optical microscopy image of the MEE graphene flakes on SiO_2/Si substrate. **d** Lateral size and thickness distribution histograms of the MEE graphene sheets, as estimated from corresponding AFM images. The graphene flakes are mainly distributed in the range of 2–8 nm thickness (~80%) with lateral size about 1–5 μm. Figure reproduced from Ref. [12]

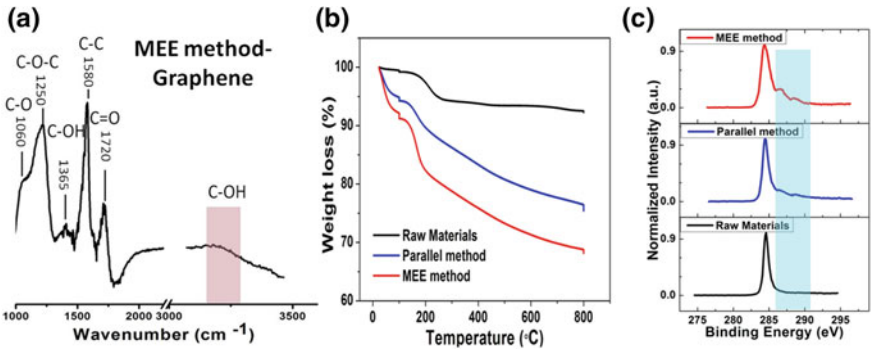

Fig. 2.2 **a** FTIR spectrum, **b** TGA plots and XPS C1 s spectra **c** for raw materials, parallel configuration graphene flakes and MEE graphene flakes

(Fig. 2.2c). In which, the peaks at 286, 287 and 289 eV in XPS C1 s spectra (blue area), which are assigned to C–O, C=O and carboxyl groups, respectively, were identified. This corroborates the significant oxidization of MEE graphene [16].

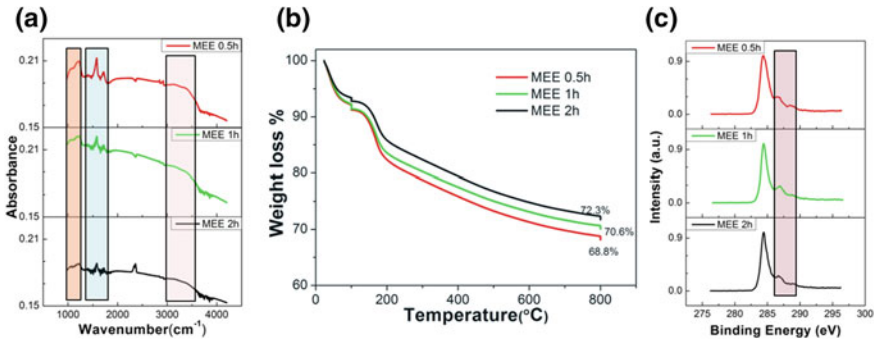

Fig. 2.3 FT-IR spectra **a**, TGA curves **b** and XPS C1 s spectra **c** of MEE GO prepared with different reaction time

The electrolysis time is found to be important for controlling the quality of graphene, including oxidization state, thickness/lateral size distribution and production efficiency. Specially, the FTIR intensity of typical functional groups peaks, such as C–O (at 1060 cm^{-1}) and C–O–C (1250 cm^{-1}), C=O stretch in carboxylic acid (1690–1710 cm^{-1}), and COO–H/CO–H (1365 cm^{-1}) remarkably decrease with the increase of exfoliation time (Fig. 2.3a). This is attributed to the remove of function groups upon heating with prolonging the reaction time [17]. This phenomenon is further confirmed by TGA results, in which slightly decrease in the total weight loss are observed (Fig. 2.3b), i.e. 31.2%, 29.4% and 27.7% for MEE 0.5 h, MEE 1 h and MEE 2 h, respectively. Particularly, a remarkable decrease in hydroxyl content (C–O, 286.6–286.8 eV) was observed from MEE 0.5 to MEE 2 h (Fig. 2.3c).

Electrolyte plays an important in efficient electrochemical exfoliation of graphene precursors. Various aqueous protonic acids including phosphoric acid, oxalic acid, sulfuric acid, acetic acid and formic acid were explored. These acids with bulky anions, such as phosphoric acid, sulfuric acid, and oxalic acid were proven to be effective in the exfoliation of spent graphite rod. The diverse choices of aqueous electrolyte provide us with more freedom to adjust the oxidization states of exfoliated graphene and reduce the production cost further. Oxalic acid solution is of particular interest due to: (i) the exfoliation process is faster; (ii) the oxalic acid exfoliated graphene exhibit better solubility in DI water, and (iii) the post-treatment is much easier. Poor performance have been observed for formic acid and acetic acid. This probably results from the weak anion salvation and weak expansion of graphite sheets upon the intercalation of HCOO– or H_3CCOO–, due to the their smaller size [18].

Previously reports indicated that the successful electrochemical exfoliation of graphite was strongly dependent on the graphite structure, and hence exfoliation

was observable only on high quality crystalline graphite such as HOPG, natural graphite flakes or paper [19, 20]. In our design, there is no special requirement on the quality and morphology of graphite source. Recycled graphite rod obtained from spent Zn–C primary batteries and pencil core could be equally well exfoliated without the need of special pre-treatment or cleaning. This design would no doubt pave the way for the commercialization of graphene, and also open up a wide opportunity for recycling of spent graphite in future.

2.3.2 *The Mechanism for Electrochemical Exfoliation*

Upon a high potential (~6–8 V) is applied across the two electrodes, the electrolyte anions such as OH^-, HSO_4^- and SO_4^{2-} and their solvated complexes (in the case of dilute H_2SO_4 being used as the electrolyte) are driven to graphite anode (Fig. 2.4). Electrochemical oxidation reactions (Eqs. 2.1–2.4) including the anodic

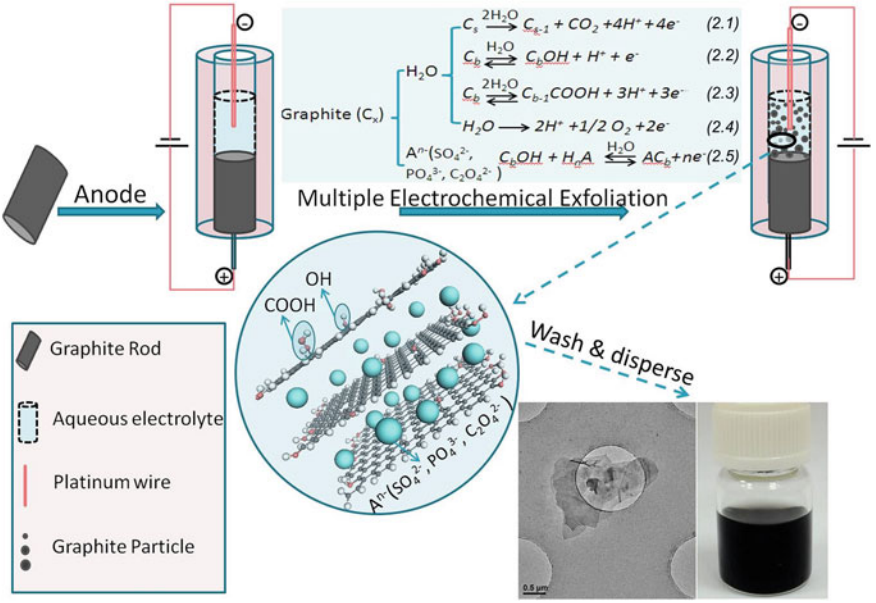

Fig. 2.4 Schematics of multiple electrochemical exfoliation (MEE) process. The digital photograph of the dispersed exfoliated graphene sheets in DMF solution, and the corresponding typical TEM images are shown. The mechanism of electrochemical exfoliation that consisting of anodic oxidation of graphite (Eqs. 2.1–2.3) and water (Eq. 2.4), and the intercalation of anions into graphite rod (C_s−surface of graphite rod, C_b−bulk of graphite rod) (Eq. 2.5), is illustrated. Schematic of graphite intercalation compound (GIC) with both hydroxyl and carboxyl groups formed is shown. Figure reproduced from Ref. [12]

oxidation, hydroxylation and carboxylation of graphite (as well as water oxidation), were triggered by the current flow accompanying with the remove of the electrons from anode (Fig. 2.4). These processes take place initially at the surface, grain boundary or structural defect sites, generating •OH, •COC, CO•, and COO• functional groups on the graphite surface. During these processes, CO_2 and O_2 can be produced as the electrolysis products (Eqs. 2.1 and 2.4) [21, 22]. The release of gaseous bubbles was obviously observed during the electrochemical process, which became vigorous with increasing exfoliation time, as if water boiled. The anodic corrosion/etching as well as the violent gas release open up the edge sheets of the graphite rod and facilitate the intercalation of bulky anions (as well as their solvated moieties) into the graphite layers, forming graphite-intercalation-compounds (GIC) ($C + A^- \rightarrow CA + e^-$) (Eq. 2.5). The intercalation and the hydrolysis of the intercalated complex ($CA + H_2O \rightarrow COH + H^+ + e^-$) [18, 23] lead to the expansion of graphene sheets and the cleavage/exfoliation of functional graphene sheets. Here, a mixture of GIC and graphite oxide is obtained. The exfoliated particles can be pushed up by the gas bubbles if they are small in size or light in weight. Or they would sink if the exfoliated particles are large and heavy. Nevertheless the precipitating big GIC particles can continue the electrochemical exfoliation when they have electric contact with anode. Multiple exfoliation process would proceed until smaller graphene sheets form and suspend in the solution. Therefore, the exfoliated graphene sheets produced in vertical design are thinner and better distributed in layer numbers.

2.3.3 *Electrochemical Performance of Resulted Graphene Flakes*

The graphene flakes were used as electrocatalysts for oxygen reduction reaction (ORR). To optimize their electrocatalytic performance further, nitrogen-doping was performed *via* annealing as-prepared MEE-Graphene in Ar/NH_3 atmosphere. The appearance of N1 s peaks and a sharp decrease in the intensity of O1 s peaks in XPS spectra corroborate the incorporation of N, and the reduction/remove of functional groups. The calculated N/C atomic ratio is 5.4 atomic %, similar to the values of N-doped graphene [24, 25]. The high resolution XPS N1s spectrum reveals the presence of pyridinic N (398.2 eV), pyrrolic N (400.5 eV), quantury N (401.1 eV) and N-oxides of pyridinc N (402.1 eV). These nitrogen-doped active sites are of particular interest for improving ORR electrocatalytic performance of carbon materials [24, 25].

The ORR catalytic activities of the MEE graphene before and after N-doped were investigated using rotating disk electrode (RDE) measurements in O_2−saturated 0.1 M KOH electrolyte (Fig. 2.5). A clear two-step process with

onset potentials at 0.82 V and 0.40 V, respectively, has been identified for the as-prepared MEE graphene, consisting well with previous reports on pure CNT [26] and graphene [27] (Fig. 2.5a). On the other hand the N-doped graphene electrode exhibits a well-defined, one-step process, suggesting a four-electron pathway for ORR on N-doped graphene (Fig. 2.5b). Furthermore, a much more positive ORR onset potential (0.92 V, *vs.* RHE) and higher cathodic currents are identified, corroborating the enhanced ORR catalytic performance [28]. The increase in electrocatalytic sites during N-doping process and the reduction of graphene are responsible for the enhanced ORR activities. Moreover, the corresponding Koutecky-Levich plots at different potential exhibit good linearity, and their slops were nearly the same over the potential range of 0.65–0.80 V, indicating the first-order reaction kinetics with almost constant electron-transfer numbers for ORR over a wide electrode potential (inset in Fig. 2.5b) [29]. The electron-transfer number n was calculated to be 3.9 according to the slopes of Koutecky-Levich plots, suggesting that nearly four-electron transfer process taken place in this potential range.

The stability tests were conducted in order to confirm the feasibility of MEE N-doped graphene for ORR application. There is only slightly decrease in limiting current, and the onset potential remains the same (Fig. 2.5c). The good catalytic stability was further confirmed by the overlap of CV curves before and after 20,000

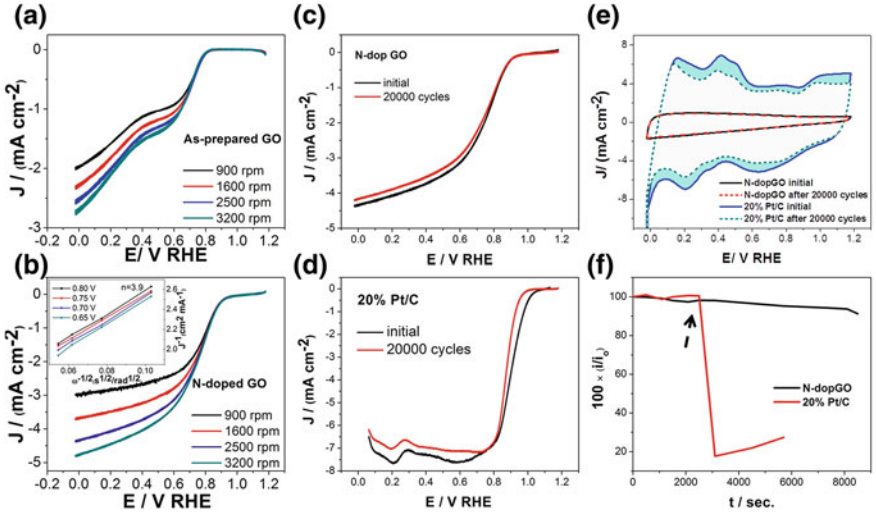

Fig. 2.5 ORR curves for as-prepared graphene **a** and N-doped graphene **b** in O_2−saturated 0.1 M KOH solution. The inset in **b** shows corresponding Koutecky-Levich plots derived from the ORR measurements. Polarization curves of N-doped G **c** and 20% Pt/C catalysts **d**, before and after 20,000 potential cycles. (Sweep rate, 100 mV/s; rotating rate, 2500 rpm.) **e** Cyclic Voltammerty curves of N-doped GO and 20% Pt/C catalysts before and after 20,000 cycles. **f** Current (i)-time (t) chronoamperometric responses to methanol. The arrow indicates the addition of 2% (weight ratio) methanol. Figure reproduced from Ref. [12]

cycling (Fig. 2.5e). Unlike N-doped graphene electrode, negative shifts in onset potential, reduction in limiting current as well as loss of surface area of CV curves were observed for 20% Pt/C electrode (Fig. 2.5d and e).

The N-doped graphene was further subjected to test the poisoning effect in the presence of methanol. As illustrated in Fig. 2.5f, the current response decreases sharply upon the addition of 2 wt% methanol for 20% Pt/C electrode. In contrast, the N-doped graphene electrode displays a strong and stable amperometric response, indicating a high selectivity due to the much lower ORR potential than that required for oxidization of methanol molecules [27, 30].

2.4 Conclusion

In conclusion, a simple, green and cost effective multiple electrochemical exfoliation approach has been proposed for synthesizing graphene in high quality and quantity. The mechanism of multiple electrochemical exfoliation of graphite was elucidated in detail. The experiment conditions are optimized. The nitrogen-doped graphene sheets have been demonstrated to deliver good electrocatalytic activity, stability and toxicity tolerance for alkaline electrolyte-based oxygen reduction reaction. Our present findings pave the way for scaled-up preparation, and further commercialization of graphene in a low cost and environmentally friendly way.

References

1. K.S. Novoselov, A.K. Geim, S.V. Morozov, D. Jiang, Y. Zhang, S.V. Dubonos, I.V. Grigorieva, A.A. Firsov, Electric field effect in atomically thin carbon films. Science **306**, 666–669 (2004)
2. S. Bae, H. Kim, Y. Lee, X.F. Xu, J.S. Park, Y. Zheng, J. Balakrishnan, T. Lei, H.R. Kim, Y.I. Song, Y.J. Kim, K.S. Kim, B. Ozyilmaz, J.H. Ahn, B.H. Hong, S. Iijima, Roll-to-roll production of 30-inch graphene films for transparent electrodes. Nat. Nanotechnol. **5**, 574–578 (2010)
3. X.S. Li, W.W. Cai, J.H. An, S. Kim, J. Nah, D.X. Yang, R. Piner, A. Velamakanni, I. Jung, E. Tutuc, S.K. Banerjee, L. Colombo, R.S. Ruoff, Large-area synthesis of high-quality and uniform graphene films on copper foils. Science **324**, 1312–1314 (2009)
4. K.V. Emtsev, A. Bostwick, K. Horn, J. Jobst, G.L. Kellogg, L. Ley, J.L. McChesney, T. Ohta, S.A. Reshanov, J. Rohrl, E. Rotenberg, A.K. Schmid, D. Waldmann, H.B. Weber, T. Seyller, Towards wafer-size graphene layers by atmospheric pressure graphitization of silicon carbide. Nat. Mater. **8**, 203–207 (2009)
5. S. Park, R.S. Ruoff, Chemical methods for the production of graphenes. Nat. Nanotechnol. **4**, 217–224 (2009)
6. X.L. Li, H.L. Wang, J.T. Robinson, H. Sanchez, G. Diankov, H.J. Dai, Simultaneous nitrogen doping and reduction of graphene oxide. J. Am. Chem. Soc. **131**, 15939–15944 (2009)
7. N. Liu, F. Luo, H.X. Wu, Y.H. Liu, C. Zhang, J. Chen, One-step ionic-liquid-assisted electrochemical synthesis of ionic-liquid-functionalized graphene sheets directly from graphite. Adv. Funct. Mater. **18**, 1518–1525 (2008)

8. J. Lu, J.X. Yang, J.Z. Wang, A.L. Lim, S. Wang, K.P. Loh, One-pot synthesis of fluorescent carbon nanoribbons, nanoparticles, and graphene by the exfoliation of graphite in ionic liquids. ACS Nano **3**, 2367–2375 (2009)
9. J.Z. Wang, K.K. Manga, Q.L. Bao, K.P. Loh, High-yield synthesis of few-layer graphene flakes through electrochemical expansion of graphite in propylene carbonate electrolyte. J. Am. Chem. Soc. **133**, 8888–8891 (2011)
10. O. Shornikova, N. Sorokina, N. Maksimova, V. Avdeev, Graphite intercalation in the graphite-H_2SO_4-R (R = H_2O, C_2H_5OH, C_2H_5COOH) systems. Inorg. Mater. **41**, 120–126 (2005)
11. C.Y. Su, A.Y. Lu, Y.P. Xu, F.R. Chen, A.N. Khlobystov, L.J. Li, High-quality thin graphene films from fast electrochemical exfoliation. ACS Nano **5**, 2332–2339 (2011)
12. J. Liu, C.K. Poh, D. Zhan, L. Lai, S.H. Lim, L. Wang, X. Liu, N. Gopal Sahoo, C. Li, Z. Shen, J. Lin, Improved synthesis of graphene flakes from the multiple electrochemical exfoliation of graphite rod. Nano Energy **2**, 377–386 (2013)
13. F.B. Su, Z.Q. Tian, C.K. Poh, Z. Wang, S.H. Lim, Z.L. Liu, J.Y. Lin, Pt Nanoparticles supported on nitrogen-doped porous carbon nanospheres as an electrocatalyst for fuel cells. Chem. Mater. **22**, 832–839 (2010)
14. Y. Si, E.T. Samulski, Synthesis of water soluble graphene. Nano Lett. **8**, 1679–1682 (2008)
15. D.C. Marcano, D.V. Kosynkin, J.M. Berlin, A. Sinitskii, Z.Z. Sun, A. Slesarev, L.B. Alemany, W. Lu, J.M. Tour, Improved synthesis of graphene oxide. ACS Nano **4**, 4806–4814 (2010)
16. D.V. Kosynkin, A.L. Higginbotham, A. Sinitskii, J.R. Lomeda, A. Dimiev, B.K. Price, J.M. Tour, Longitudinal unzipping of carbon nanotubes to form graphene nanoribbons. Nature **458**, 872–U875 (2009)
17. H.K. Jeong, Y.P. Lee, M.H. Jin, E.S. Kim, J.J. Bae, Y.H. Lee, Thermal stability of graphite oxide. Chem. Phys. Lett. **470**, 255–258 (2009)
18. M. Bottomley, A.R. Ubbelohde, G.S. Parry, D.A. Young, Electrochemical preparation of salts from well-oriented graphite. J. Chem. Soc. 5674–5680 (1963)
19. G.M. Morales, P. Schifani, G. Ellis, C. Ballesteros, G. Martinez, C. Barbero, H. J. Salavagione, High-quality few layer graphene produced by electrochemical intercalation and microwave-assisted expansion of graphite. Carbon **49**, 2809–2816 (2011)
20. D. Wei, L. Grande, V. Chundi, R. White, C. Bower, P. Andrew et al., Graphene from electrochemical exfoliation and its direct applications in enhanced energy storage devices. Chem. Commun. (2012)
21. F. Beck, H. Krohn, E. Zimmer, Corrosion of graphite-intercalation compounds. Electrochim. Acta **31**, 371–376 (1986)
22. F. Beck, H. Krohn, Reversible electrochemical intercalation of anions from aqueous-solutions in polymer bound graphite-electrodes. Synth. Met. **7**, 193–199 (1983)
23. F. Beck, H. Krohn, W. Kaiser, Galvanostatic cycling of graphite-intercalation electrodes with anions in aqueous acids. J. Appl. Electrochem. **12**, 505–515 (1982)
24. L.F. Lai, J.R. Potts, D. Zhan, L. Wang, C.K. Poh, C.H. Tang, H. Gong, Z.X. Shen, L.Y. Jianyi, R.S. Ruoff, Exploration of the active center structure of nitrogen-doped graphene-based catalysts for oxygen reduction reaction. Energy Environ. Sci. **5**, 7936–7942 (2012)
25. Z.Q. Luo, S.H. Lim, Z.Q. Tian, J.Z. Shang, L.F. Lai, B. MacDonald, C. Fu, Z.X. Shen, T. Yu, J.Y. Lin, Pyridinic N doped graphene: synthesis, electronic structure, and electrocatalytic property. J. Mater. Chem. **21**, 8038–8044 (2011)
26. K.P. Gong, F. Du, Z.H. Xia, M. Durstock, L.M. Dai, Nitrogen-doped carbon nanotube arrays with high electrocatalytic activity for oxygen reduction. Science **323**, 760–764 (2009)
27. L.T. Qu, Y. Liu, J.B. Baek, L.M. Dai, Nitrogen-doped graphene as efficient metal-free electrocatalyst for oxygen reduction in fuel cells. ACS Nano **4**, 1321–1326 (2010)

28. Y.Y. Liang, Y.G. Li, H.L. Wang, J.G. Zhou, J. Wang, T. Regier, H.J. Dai, Co(3)O(4) nanocrystals on graphene as a synergistic catalyst for oxygen reduction reaction. Nat. Mater. **10**, 780–786 (2011)
29. R.L. Liu, D.Q. Wu, X.L. Feng, K. Mullen, Nitrogen-doped ordered mesoporous graphitic arrays with high electrocatalytic activity for oxygen reduction. Angew. Chem.-Int. Edit. **49**, 2565–2569 (2010)
30. J. Liu, H. Yang, S.G. Zhen, C.K. Poh, A. Chaurasia, J. Luo, X. Wu, E.K.L. Yeow, N.G. Sahoo, J. Lin, Z. Shen, A green approach to the synthesis of high-quality graphene oxide flakes via electrochemical exfoliation of pencil core. RSC Adv. **3**, 11745–11750 (2013)

Chapter 3
High-Performance Graphene Foam/Fe_3O_4 Hybrid Electrode for Lithium Ion Battery

The development of deformable electrodes with good electrochemical performance in addition to ultrathin, lightweight and flexible, is one key challenge in flexible electrochemical energy storage devices. Graphene foam (GF), is a three-dimensional (3D) interconnected network of high-quality chemical vapour deposition-grown graphene. It processes high porosity, good electric conductivity and mechanical integrity, and is a good scaffold for flexible electrodes. In this chapter, thin, lightweight, and flexible Fe_3O_4/GF electrode has been designed based on the 3D interconnected current collector via a bottom up approach assisted by atomic layer deposition. The 3D interconnect feature of GF provides a highly conductive pathway for ions and electrons. Benefiting from the unique design, the electrode delivers high reversible capacity and fast charge/discharge capability.

3.1 Introduction

The prosperity of hybrid electric vehicles (HEV), portable electronics and micro-electro-mechanical systems (MEMS) has promoted increasing demand for high-performance lithium ion batteries (LIB) [1, 2]. The achievements are strongly dependent on scrupulous selection of active materials and unique nanostructures design that ensuring fast pathway for electron/ions diffusion. Fe_3O_4 has been demonstrated to be an attractive anode material due to high theoretical energy capacity, low cost, low toxicity, and ease of fabrication [3, 4]. However, Fe_3O_4 always suffers from poor cyclability caused by drastic volume expansion during Li^+ ion intercalation/de-intercalation process [4]. Particularly, the loss of electrical connection of Fe_3O_4 from current collectors resulting from high volume changes during continuous charge–discharge process has been reported, which significantly limits its practical application [5]. Many approaches have been proposed to address this challenge, such as fabricating Fe_3O_4 nanomaterials into optimized nanostructure

J. Liu, *Graphene-Based Composites for Electrochemical Energy Storage*,
Springer Theses, DOI 10.1007/978-981-10-3388-9_3

and shapes [6–9] or embed the active materials in a cushioning medium including conductive medium [10–15] or other stable metal oxides [16, 17].

Building nanostructures is considered as an effective strategy to improve the electrochemical performance of the LIB electrode benefiting from several advantages over their bulk counterparts [6, 15, 18–20]. (i) The nanostructure processes a short transport path for Li^+ diffusion. (ii) The well electric/mechanical contact at electrode/electrolyte interface ensures facile charge transport. (iii) The nanostructure could accommodate the large volume expansion during charge/discharge process, and maintain the structural integrity of the electrode. Indeed various nanostructures including solid/hollow nanoparticle [21, 22], nanotube [7], nanowire [23], porous nanosheet [24], and nanowall [25], have been designed to improve the performance of iron oxide-based electrodes. In addition, through combining with other conductive additives, such as metal nanostructures [10], polymers [26], carbon materials [12, 13, 15] and other stable materials [17], the electric conductivity of iron oxide-based electrode could be further optimized via reducing the diffusion length. Particularly, the hybridization of Fe_3O_4 with carbon allotropes including porous carbon, carbon nanotubes and graphene, provides great opportunity in improving the performance of Fe_3O_4 as the LIB electrodes [11, 24, 27].

Although intense efforts have been made, the improvement in electrochemical performance of Fe_3O_4 LIB electrode is still marginal. The fabrication of Fe_3O_4 based electrodes with good rate performance and long cycle life is still challengeable but highly desirable. In this work, GF/Fe_3O_4 hybrid electrode was prepared via a novel and facile bottom up approach. The unique hybrid electrode delivers several characteristics: (i) good electric contact and facile electron/ions transportation [28, 29]; (ii) good mechanical contact and integrity ensures long cycle time; (iii) adjustable and large active material loading; (iv) lightweight, flexible features ensures that the GF/Fe_3O_4 hybrid electrode used directly without the employing of binder or other conducting additive. Benefiting from this unique design, the GF/Fe_3O_4 hybrid electrode demonstrates good cycling performance (up to 500 cycles) and fast charge/discharge feature (10 C) [30].

3.2 Experiment and Characterization

3.2.1 Materials Synthesis

Synthesis of graphene foams. The 3D graphene foams were prepared via chemical vapour deposition [28, 31].

Synthesis of ZnO. Prior to ALD deposition, GF was treated with oxygen plasma (March PX-250 plasma etching system). The diethyl zinc (DEZ, 99.99%, Sigma Aldrich) and H_2O were adopted as the Zn and O precursors for the deposition of ZnO (Beneq TFS 200 system) at 200 °C. The thickness was controlled by the deposition cycles. Samples with thickness of 10, 30, and 50 nm, were prepared in this work.

Formation of Fe_3O_4 nanostructure. The GF/Fe_3O_4 electrode is achieved via (i) bathing ZnO-coated GF into a mixture of $FeCl_3$ (30 mM) and glucose solution (30 mM) for 24 h, and followed with (ii) annealing in Ar atmosphere at 400 °C for 2 h.

3.2.2 Material Characterization

Structure and Morphology Characterization. The morphology of the samples were characterized with JEOL JSM 6700F field emission scanning electron microscopy (SEM) and JEOL JEM-2010 transmission electron microscopy (TEM). The element chemical information is collected via X-ray photoelectron spectroscopy (XPS) [VG ESCALAB 220i-XL system, monochromatic Al Ka1 source (1486.6 eV)] and Thermogravimetric analysis (TGA) (TGA Q500, Thermal Analysis Instruments, Burlington, MA).

Electrochemical Performance Evaluation. Electrochemical performance was evaluated on CR2032-coin-type cells using the free-standing GF/Fe_3O_4 as working electrode and lithium foil as the counter electrode. The electrolyte was 1 M $LiPF_6$ in a mixture organic solvent consisting of ethylene carbonate (EC) and diethyl carbonate (DEC) (1:1 v/v). The assembled cells were assembled and aged in the glove box prior to the electrochemical measurements. Galvanostatical discharge/charge testing were performed over the voltage range of 0.01–3.0 V (vs. Li^+/Li) using a NEWARE cell tester. The cyclic voltammetry (CV) and electrochemical impedance spectroscopy (EIS) were carried out using a CHI 660D workstation (CHI instrument Co. Shanghai).

3.3 Results and Discussions

3.3.1 The Synthesis of GF/Fe_3O_4 Hybrid Films

Three steps are involved for the synthesis of the GF/Fe_3O_4 nanostructure electrodes (Fig. 3.1). Firstly, self-supported graphene foam was achieved via (i) catalytic decomposition of CH_4 on Ni foam, and (ii) the etching away of Ni backbone (Fig. 3.1a) [28]. Secondly, ALD-deposited ZnO coated onto the graphene foam, forming a thin layer (Fig. 3.1b). ALD is a thin film deposition technique that lead to uniform and conformal films with precise thickness control via self-limiting surface reactions [32, 33]. GF was treated by oxygen plasma prior to ALD to introduce hydroxyl bonds on the surface, and ensure the conformal coating of ZnO [34, 35]. Thirdly, ZnO was converted into FeOOH via bathing GF/ZnO into the mixed solution of $FeCl_3$ solution with glucose. The bicontinuous/mesoporous GF/Fe_3O_4 was then obtained after annealed in Ar atmosphere (Fig. 3.1c). The glucose is

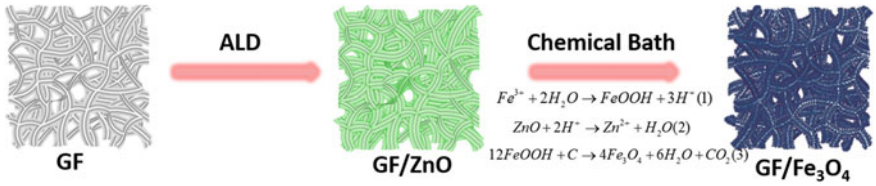

Fig. 3.1 Schematic illustration of the indirect ALD approach. Figure reproduced from Ref. [30]

converted into amorphous carbon that surrounding around the Fe_3O_4 nanoparticles accompanying with pyrolysis process [15]. The indirect ALD approach for the synthesis of GF/Fe_3O_4 in this work is superior over the direct ALD coating method in terms of high growth rate, large active materials loading, and flexible/low requirements for temperature and ozone atmosphere [36, 37]. More importantly, different from the compact thin film formed in traditional ALD approach, unique bicontinuous/mesoporous-nanostrucure could be generated, which is particularly favorable for the fast charge/discharge electrode.

The morphology of the GF/Fe_3O_4 hybrid structure is characterized via SEM and TEM. GF inherits the 3D structure of the Ni foam backbone well, with porous feature (Fig. 3.2a, d). GF is ultrathin and lightweight, and its thickness or the areal density (0.1–0.8 mg cm^{-1}) could be tuned via controlling the carbon source amount and growth time. There is no obvious change in the morphology of graphene foam after ZnO coating, corroborating the conformal coating of ZnO (Fig. 3.2b). More details about the tiny particle of ZnO could be found in Fig. 3.2e and h. The uniform coating of ZnO is the key prerequisite for the good coverage of Fe_3O_4 on GF. By adjusting the deposition amount of ZnO, the mass loading of the Fe_3O_4 can be easily controlled. The graphene foam surface becomes rough, covered by small particles, after the replacement reaction of ZnO into Fe_3O_4 (Fig. 3.2f and i). The formation of bicontinuous/mesoporous nanostructure with Fe_3O_4 nanocrystallites interconnected with each other was clearly observed (Fig. 3.3a). The HRTEM image (Fig. 3.3b) and corresponding SAED image (Fig. 3.3c) reveal that the nanoparticle is single crystalline with an average diameter of 30 nm. The lattice fringe distance of 0.25 nm, corresponding to the (311) plane of Fe_3O_4, is also identified.

To learn more about the structure and composition of the GF/Fe_3O_4 electrodes, X-ray diffraction (XRD), Raman spectroscopy and X-ray photoelectron spectroscopy (XPS) measurements were conducted. Two typical diffraction peaks at 26.5 and 54.6° are observed for GF, corresponding to the (002) and (004) reflection planes of graphitic carbon (JCPDS card 75-1621), respectively (Fig. 3.3d) [38]. More diffraction peaks appear for GF/ZnO composites, result from the hexagonal structure of ZnO (JCPDS card 36-1451). The high deposition temperature ensures that ALD ZnO is crystalline. After the replacement of ZnO with Fe_3O_4, the characteristic peaks of ZnO disappear accompanying with the appearance of the typical peaks of magnetite Fe_3O_4 (JCPDS, card 19-0629) (Fig. 3.3d). In Rama spectra (Fig. 3.3e), three typical peaks of graphene, centering at 1580 cm^{-1} (G), 2550 cm^{-1} (G′), and 2720 cm^{-1}(2D) are identified [28, 31, 38]. The absence of

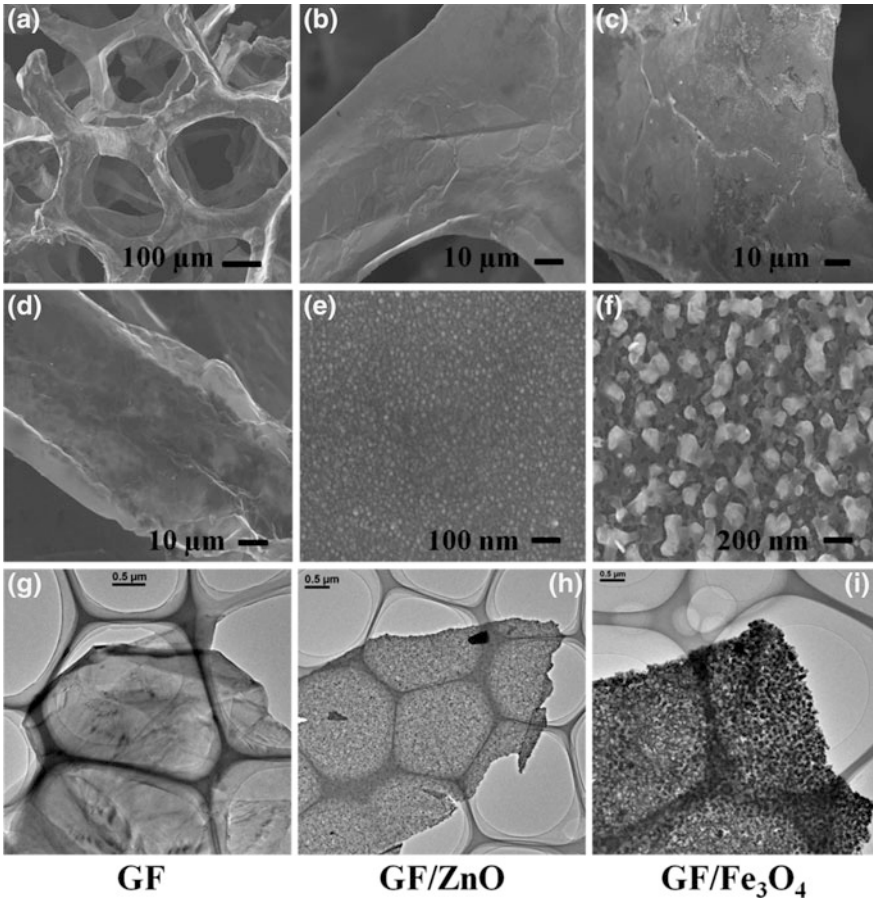

Fig. 3.2 SEM images of GF (**a**, **d**), GF/ZnO (**b**, **e**) and GF/Fe_3O_4 (**c**, **f**). TEM images of GF (**g**), GF/ZnO (**h**), and GF/Fe_3O_4 (**i**). Figure reproduced from Ref. [30]

the defect-related D band at 1350 cm^{-1} corroborates the high quality of the GF. The Raman intensity of the 2D band is much smaller than the 2D band, indicating that the GF is multilayer [31, 38]. These features make GF to be promising scaffold for electrodes. Three more Raman peaks appear at 438, 496, and 569 cm^{-1} after the ZnO deposition, corresponding to ZnO E_2 and A_1 phonons, respectively [39]. Some defects were introduced after the ZnO deposition, accompanying with the appearance of the D band. The typical Raman modes of Fe_3O_4 can be clearly identified at 667 cm^{-1} for GF/Fe_3O_4 composite, corresponds to the A_{1g} mode (Fig. 3.3e) [11]. In addition, an enhanced D band and a broadened but decreased 2D band are observed. The former is attributed to the introduction of more defects, while the latter may originates from the amorphous carbon layer that surrounding around Fe_3O_4 surface [40]. Corresponding XPS results were illustrated in Fig. 3.3f and g. Two typical

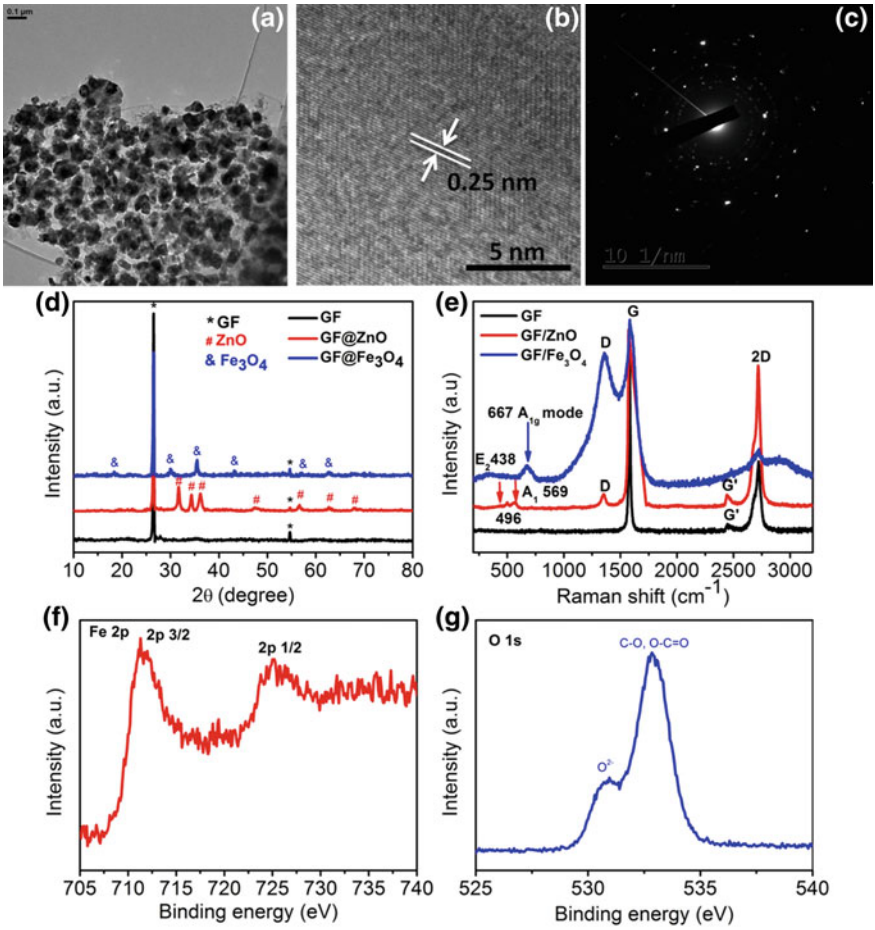

Fig. 3.3 HRTEM image of GF/Fe_3O_4 (**a**), an individual Fe_3O_4 nanoparticle (**b**) and SAED patterns of GF/Fe_3O_4 (**c**). **d** X-ray diffraction patterns and **e** Raman spectra of the GF, GF/ZnO and GF/Fe_3O_4 nanostructures. XPS of the Fe 2p states (**f**) and the O 1s state (**g**) of Fe_3O_4

characteristics of Fe_3O_4 located at 710.9 and 724.2 eV that are corresponding to the Fe $2p_{3/2}$ and $2p_{1/2}$ states, respectively, are found [41]. There is no satellite peak detected, corroborating the final product is Fe_3O_4 rather than Fe_2O_3 [41].

3.3.2 *Electrochemical Performance of GF/Fe_3O_4*

Cyclic voltammetry (CV) and galvanostatic charge/discharge curves were collected to evaluate the electrochemical property of the GF/Fe_3O_4 electrodes systematically. There are two well defined reduction peaks located at 0.67 and 0.27 V in the 1st

discharge process (Fig. 3.4a), corresponding to the structure transition ($Fe_3O_4 + xLi^+ + xe^- \rightarrow Li_xFe_3O_4$) and the further reduction of $Li_xFe_3O_4$ to Fe(0) by conversion reaction [$Li_xFe_3O_4 + (8 - x)\ Li^+ + (8 - x)\ e^- \rightarrow 4Li_2O + 3Fe$] [8, 42, 43]. Note that these two cathodic peaks positively shifted to 1.1 and 0.75 V, with the anodic peaks located at 1.6 and 2.3 V, respectively, for the subsequent cycles. These two redox pairs were attributed to the reversible reduction/oxidation ($Fe_3O_4 \leftrightarrow Fe$) reactions during lithiation/delithiation process [42, 43].

Apart from the reaction peaks for Fe_3O_4, one more redox pair is found at 0.1 V (cathodic) and 0.27 V (anodic), indicating that GF taken part in electrochemical reactions [29, 44]. This redox pair exhibits lower peaks' intensity than those of Fe_3O_4. This is probably because of the high loading of Fe_3O_4 (80% of weight percentage) as also confirmed by the TGA result. The 2nd and 3rd CV curves almost overlap with each other, suggesting the good reversibility of GF/Fe_3O_4 electrode. There are two voltage plateaus located at 0.4 and 0.65 V in the 1st discharge curve (Fig. 3.4b), corresponding to irreversible reactions induced by the formation of SEI. They disappear since the 2nd cycle, consisting well with the CV curves. The GF/Fe_3O_4 hybrid electrode has demonstrated a high initial capacity of 1192 mAh g^{-1} in the 1st cycle and a lower capacity of 785 mAh g^{-1} in the 2nd cycle, giving rise to a columbic efficiency of 66%. The irreversible reactions

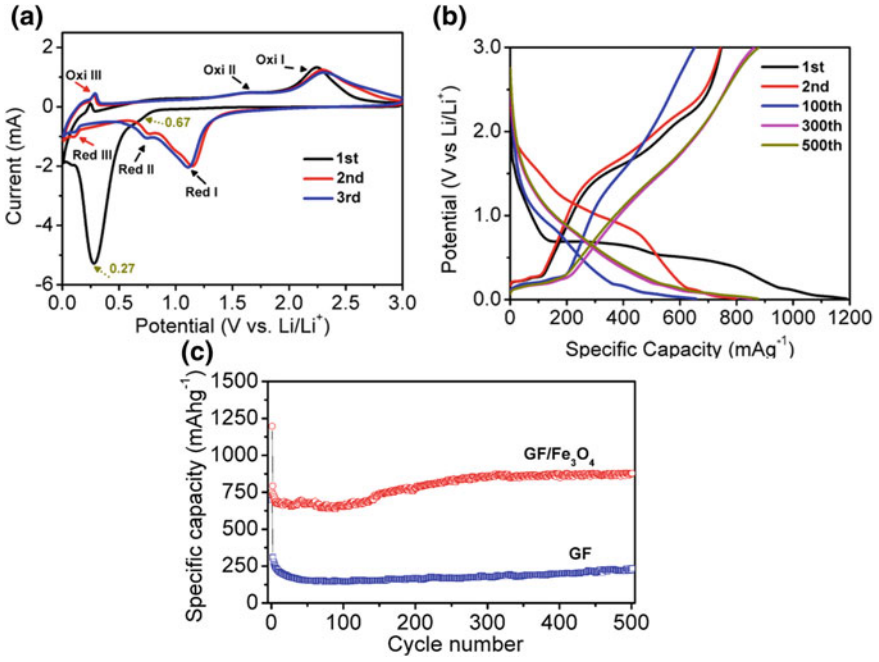

Fig. 3.4 **a** Cyclic voltammetry (CV) curves, and **b** discharge/charge profiles of the GF/Fe_3O_4 electrode. **c** Cycling profiles of the GF and GF/Fe_3O_4 electrodes at 1C rate. Figure reproduced from Ref. [30]

involved in the formation of the SEI layer account for the 34% capacity loss [13, 15, 27]. The discharge/charge measurements were carried out up to 500 cycles to evaluate the cycle performance. After deep cycling to 300 and 500 cycles, the plateaus of the discharge–charge profiles are not so evident as in the initial stage (Fig. 3.4b), which are in agreement with the previous reports [43, 45]. The good cyclic performance is revealed in Fig. 3.4c. The capacity decreases slightly for the initial 100 cycles, and then increases gradually. The hybrid electrode could deliver a capacity of 870 mAh/g up to 500 charge/discharge cycles, which is better than that of previous reports [11, 12, 43]. In summary, the electrode displays relatively stable performance and high capacity retention (Fig. 3.4c). On the other hand, pure Fe_3O_4 electrode always displays much shorter cycle life (<100 cycles) even at a much smaller charge/discharge rate (i.e., 0.5 C).

Galvanostatic discharge/charge measurements were conducted at various C rates to evaluate the rate performance of GF/Fe_3O_4. The specific capacity deceases with increasing C rates (Fig. 3.5a and b). A specific capacity of 190 mAh g^{-1} was achieved at 60 C, suggesting that the full charge could complete in one minutes. The GF/Fe_3O_4 hybrid electrode still delivers a high capacity of 800 mAh g^{-1} even

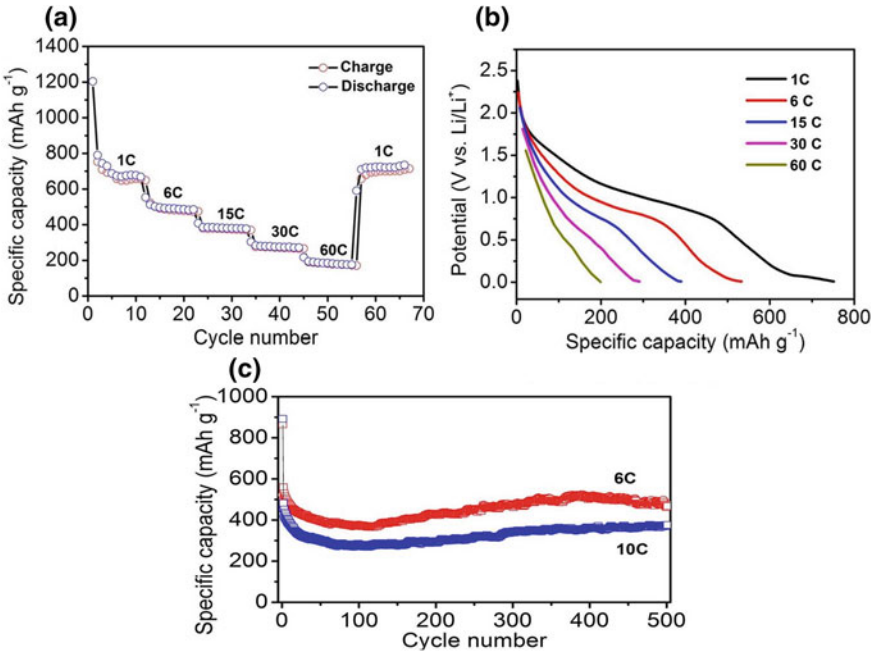

Fig. 3.5 Rate capability of the GF/Fe_3O_4 LIB electrode. **a** Specific capacity of the GF/Fe_3O_4 electrode under different discharge/charge rates. **b** Discharge profiles of the GF/Fe_3O_4 electrode at different current rates. **c** Cycling profiles of the GF/Fe_3O_4 electrodes at 6 and 10 C rates. Figure reproduced from Ref. [30]

when the C rate reduces back to 1 C, corroborating the high stability and good reversibility. The retained capacities of ~400 and 300 mAh g^{-1} could be identified at 6 and 10 C charge/discharge rates, respectively, till 500 cycles (Fig. 3.5c).

3.3.3 *Underlying Mechanism for the Enhanced Electrochemical Performance*

In order to reveal the underlying mechanism for the enhanced electrochemical performance, the composite electrodes were characterized after 500 charge/discharge cycles at 1 C (Fig. 3.6). Despite somewhat pulverization, the Fe_3O_4 layer still keeps good electric and mechanical contact with GF, and the individual Fe_3O_4 nanocrystallites can still be well maintained (Fig. 3.6a–c). Corresponding electrochemical impedance spectroscopy (EIS) results (Fig. 3.6d) reveal an evidently decrease in the charge transfer resistance of GF/Fe_3O_4 after cycling, which is partly attributed to the reduction of Fe_3O_4 into Fe during the irreversible reactions.

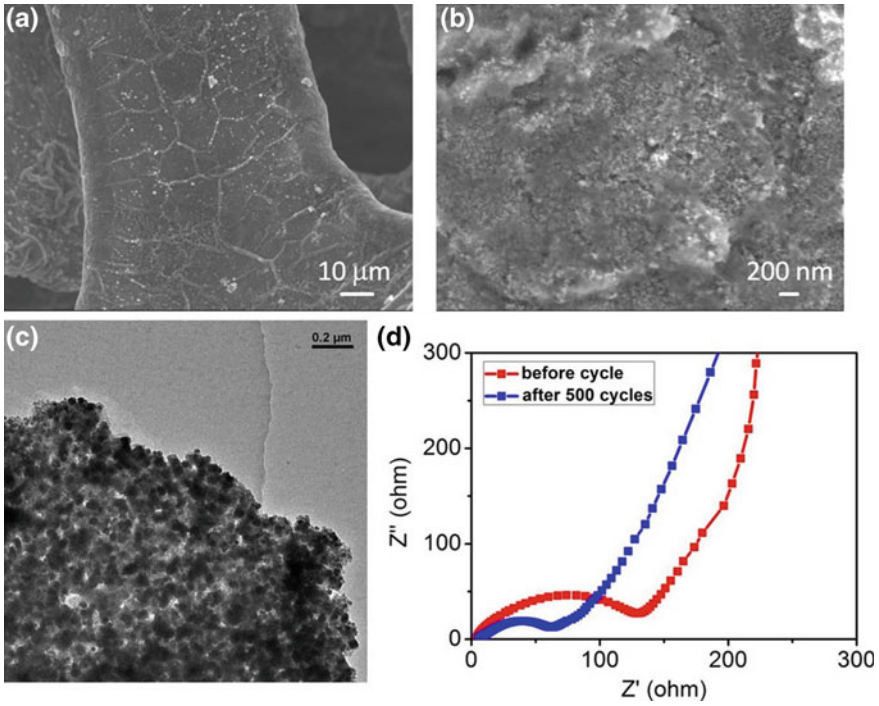

Fig. 3.6 SEM images under low magnification (**a**), high magnification (**b**) and TEM image (**c**) of GF/Fe_3O_4 after 500 cycles at 1 C. **d** Electrochemical impedance spectroscopy results for GF/Fe_3O_4 before and after 500 cycles at 1 C

Note that the specific capacity increases with prolonged cycling gradually. Similar trend has been observed for many other metal oxide-based electrodes previously [46–49]. However there is no consensus on the reason until now. There are three possibilities that may take responsible for it: (i) more active sites would be released for lithium storage resulting from the pulverization of the electrode, and thus result in the increase in capacity. (ii) Fe nanoparticles would be generated resulting from the irreversible reactions (SEI formation). The formation of metallic Fe will improve the overall conductivity of the electrode, as evidenced by the EIS results (Fig. 3.6d) [38]. Therefore, the specific capacity would increase benefiting from the enhanced charge-transfer kinetics. (iii) The organic/gel-like SEI layer would form on the electrode surface [12, 46, 49]. It could improve the mechanical cohesion of the active materials without hindering the ion transfer and provide excess lithium ion storage sites by a so-called "pseudo-capacitive-type" behavior, especially in the low potential region.

The good performance of the GF/Fe_3O_4 electrodes is attributed to the unique mesoscale structure design that takes advantages of both high electrical conductivity and good structural stability. More importantly, this ALD approach for Fe_3O_4 is general and is suitable for other carbon substrates (Fig. 3.7). As mentioned above, the deposition of ZnO is determinant via affecting the homogeneity and mass loading of the resulting active materials. It is foreseeable that, the method we reported here is possible to scale up and push the iron oxide-based LIB electrodes into real applications, given the compatibility with reduced graphene oxide/CNTs, and industry-scale ALD. Note that the total loading amount of the active materials

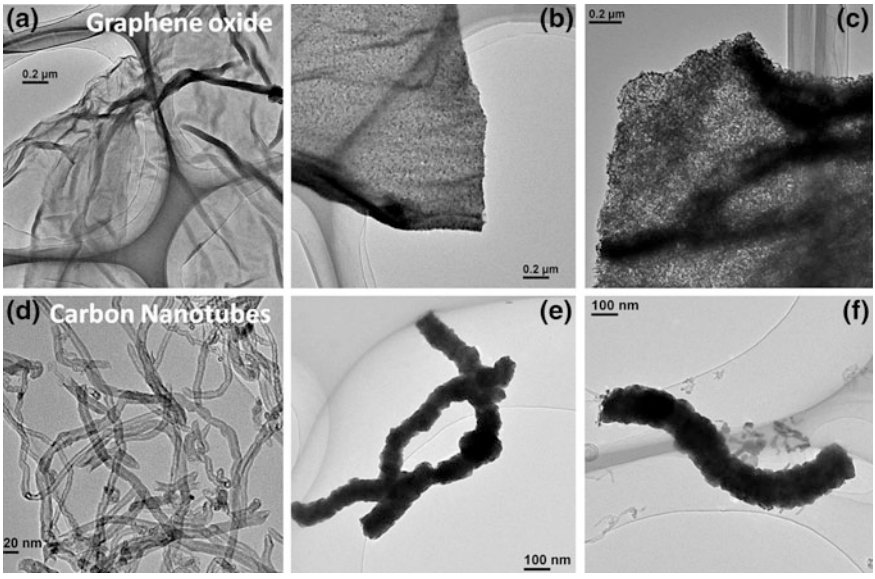

Fig. 3.7 TEM images for graphene oxide (**a**–**c**) and carbon nanotubes (**d**–**f**): **a** GO, **b** GO/ZnO and **c** GO/Fe_3O_4, **d** CNTs, **e** CNTs/ZnO and **f** CNTs/Fe_3O_4. Figure reproduced from Ref. [30]

is not high in our work, which also retards the practical application. This issue could be addressed by stacking the as fabricated GF supported active material electrodes together to form a multilayer film [30].

3.4 Conclusion

In conclusion, a novel approach to prepare bicontinous-mesoporous Fe_3O_4 nanostructures on 3D GF has been demonstrated. Benefiting from the rational design and the unique mesoscale structure, a high capacity of 785 mAh g^{-1} (1 C) could be collected and maintained up to 500 cycles. Even at the high rate of 60 C, the electrode could deliver a capacity of 190 mAh g^{-1}. The good electrochemical performance is attributed to the tightly grafting of Fe_3O_4 onto GF that benefits from the uniform ALD coating of ZnO. Particularly, this fabrication method is general and suitable for many other conductive substrates.

References

1. M. Armand, J.M. Tarascon, Building better batteries. Nature **451**, 652–657 (2008)
2. B. Kang, G. Ceder, Battery materials for ultrafast charging and discharging. Nature **458**, 190–193 (2009)
3. J.M. Tarascon, M. Armand, Issues and challenges facing rechargeable lithium batteries. Nature **414**, 359–367 (2001)
4. L. Taberna, S. Mitra, P. Poizot, P. Simon, J.M. Tarascon, High rate capabilities Fe_3O_4-based Cu nano-architectured electrodes for lithium-ion battery applications. Nat. Mater. **5**, 567–573 (2006)
5. I.T. Kim, A. Magasinski, K. Jacob, G. Yushin, R. Tannenbaum, Synthesis and electrochemical performance of reduced graphene oxide/maghemite composite anode for lithium ion batteries. Carbon **52**, 56–64 (2013)
6. P. Poizot, S. Laruelle, S. Grugeon, L. Dupont, J.M. Tarascon, Nano-sized transition-metal oxides as negative-electrode materials for lithium-ion batteries. Nature **407**, 496–499 (2000)
7. J. Chen, L. Xu, W. Li, X. Gou, α-Fe2O3 nanotubes in gas sensor and lithium-ion battery applications. Adv. Mater. **17**, 582–586 (2005)
8. M.V. Reddy, T. Yu, C.H. Sow, Z.X. Shen, C.T. Lim, G.V. Subba Rao, B.V.R. Chowdari, α-Fe_2O_3 nanoflakes as an anode material for Li-ion batteries. Adv. Funct. Mater. **17**, 2792–2799 (2007)
9. D. Larcher, C. Masquelier, D. Bonnin, Y. Chabre, V. Masson, J.-B. Leriche, J.-M. Tarascon, Effect of particle size on lithium intercalation into α-Fe_2O_3. J. Electrochem. Soc. **150**, A133–A139 (2003)
10. P.L. Taberna, S. Mitra, P. Poizot, P. Simon, J.M. Tarascon, High rate capabilities Fe_3O_4-based Cu nano-architectured electrodes for lithium-ion battery applications. Nat. Mater. **5**, 567–573 (2006)
11. G. Zhou, D.-W. Wang, F. Li, L. Zhang, N. Li, Z.-S. Wu, L. Wen, G.Q. Lu, H.-M. Cheng, Graphene-wrapped Fe_3O_4 anode material with improved reversible capacity and cyclic stability for lithium ion batteries. Chem. Mater. **22**, 5306–5313 (2010)

12. Y. Wu, Y. Wei, J. Wang, K. Jiang, S. Fan, Conformal Fe_3O_4 sheath on aligned carbon nanotube scaffolds as high-performance anodes for lithium ion batteries. Nano Lett. **13**, 818–823 (2013)
13. E. Kang, Y.S. Jung, A.S. Cavanagh, G.-H. Kim, S.M. George, A.C. Dillon, J.K. Kim, J. Lee, Fe_3O_4 nanoparticles confined in mesocellular carbon foam for high performance anode materials for lithium-ion batteries. Adv. Funct. Mater. **21**, 2430–2438 (2011)
14. C. Ban, Z. Wu, D.T. Gillaspie, L. Chen, Y. Yan, J.L. Blackburn, A.C. Dillon, Nanostructured Fe_3O_4/SWNT electrode: binder-free and high-rate Li-ion anode. Adv. Mater. **22**, E145–E149 (2010)
15. C.K. Chan, H. Peng, G. Liu, K. McIlwrath, X.F. Zhang, R.A. Huggins, Y. Cui, High-performance lithium battery anodes using silicon nanowires. Nat. Nano. **3**, 31–35 (2008)
16. Y. Luo, J. Luo, J. Jiang, W. Zhou, H. Yang, X. Qi, H. Zhang, H.J. Fan, D.Y.W. Yu, C.M. Li, T. Yu, Seed-assisted synthesis of highly ordered TiO_2@[small alpha]-Fe_2O_3 core/shell arrays on carbon textiles for lithium-ion battery applications. Energy Environ. Sci. **5**, 6559–6566 (2012)
17. J. Luo, X. Xia, Y. Luo, C. Guan, J. Liu, X. Qi, C.F. Ng, T. Yu, H. Zhang, H.J. Fan, Rationally designed hierarchical TiO_2@Fe_2O_3 hollow nanostructures for improved lithium ion storage. Adv. Energy Mater. **3**, 737–743 (2013)
18. A.S. Arico, P. Bruce, B. Scrosati, J.-M. Tarascon, W. van Schalkwijk, Nanostructured materials for advanced energy conversion and storage devices. Nat. Mater. **4**, 366–377 (2005)
19. A. Magasinski, P. Dixon, B. Hertzberg, A. Kvit, J. Ayala, G. Yushin, High-performance lithium-ion anodes using a hierarchical bottom-up approach. Nat. Mater. **9**, 353–358 (2010)
20. L.Q. Liu, W.J. Ma, Z. Zhang, Macroscopic carbon nanotube assemblies: preparation, properties, and potential applications. Small **7**, 1504–1520 (2011)
21. B. Koo, H. Xiong, M.D. Slater, V.B. Prakapenka, M. Balasubramanian, P. Podsiadlo, C.S. Johnson, T. Rajh, E.V. Shevchenko, Hollow iron oxide nanoparticles for application in lithium ion batteries. Nano Lett. **12**, 2429–2435 (2012)
22. B. Wang, J.S. Chen, H.B. Wu, Z. Wang, X.W. Lou, Quasiemulsion-templated formation of α-Fe_2O_3 hollow spheres with enhanced lithium storage properties. J. Am. Chem. Soc. **133**, 17146–17148 (2011)
23. Y. Song, S. Qin, Y. Zhang, W. Gao, J. Liu, Large-scale porous hematite nanorod arrays: direct growth on titanium foil and reversible lithium storage. J. Phys. Chem. C **114**, 21158–21164 (2010)
24. S. Yang, Y. Sun, L. Chen, Y. Hernandez, X. Feng, K. Müllen, Porous iron oxide ribbons grown on graphene for high-performance lithium storage. Sci. Rep. **2**, 427 (2012)
25. D. Lei, M. Zhang, B. Qu, L. Chen, Y. Wang, E. Zhang, Z. Xu, Q. Li, T. Wang, [small alpha]-Fe_2O_3 nanowall arrays: hydrothermal preparation, growth mechanism and excellent rate performances for lithium ion batteries. Nanoscale **4**, 3422–3426 (2012)
26. J. Liu, W. Zhou, L. Lai, H. Yang, S. Hua Lim, Y. Zhen, T. Yu, Z. Shen, J. Lin, Three dimensionals α-Fe_2O_3/polypyrrole (Ppy) nanoarray as anode for micro lithium ion batteries. Nano Energy **2**, 726–732 (2013)
27. X. Zhu, Y. Zhu, S. Murali, M.D. Stoller, R.S. Ruoff, Nanostructured reduced graphene oxide/Fe_2O_3 composite as a high-performance anode material for lithium ion batteries. ACS Nano **5**, 3333–3338 (2011)
28. Z. Chen, W. Ren, L. Gao, B. Liu, S. Pei, H.-M. Cheng, Three-dimensional flexible and conductive interconnected graphene networks grown by chemical vapour deposition. Nat. Mater. **10**, 424–428 (2011)
29. N. Li, Z. Chen, W. Ren, F. Li, H.-M. Cheng, Flexible graphene-based lithium ion batteries with ultrafast charge and discharge rates. Proc. Natl. Acad. Sci. **109**, 17360–17365 (2012)
30. J. Luo, J. Liu, Z. Zeng, C.F. Ng, L. Ma, H. Zhang, J. Lin, Z. Shen, H.J. Fan, Three-dimensional graphene foam supported Fe_3O_4 lithium battery anodes with long cycle life and high rate capability. Nano Lett. **13**, 6136–6143 (2013)

31. X. Cao, Y. Shi, W. Shi, G. Lu, X. Huang, Q. Yan, Q. Zhang, H. Zhang, Preparation of novel 3D graphene networks for supercapacitor applications. Small **7**, 3163–3168 (2011)
32. S.K. Karuturi, J. Luo, C. Cheng, L. Liu, L.T. Su, A.I.Y. Tok, H.J. Fan, A novel photoanode with three-dimensionally, hierarchically ordered nanobushes for highly efficient photoelectrochemical cells. Adv. Mater. **24**, 4157–4162 (2012)
33. C. Marichy, M. Bechelany, N. Pinna, Atomic layer deposition of nanostructured materials for energy and environmental applications. Adv. Mater. **24**, 1017–1032 (2012)
34. X. Wang, S.M. Tabakman, H. Dai, Atomic layer deposition of metal oxides on pristine and functionalized graphene. J. Am. Chem. Soc. **130**, 8152–8153 (2008)
35. S. Jandhyala, G. Mordi, B. Lee, G. Lee, C. Floresca, P.-R. Cha, J. Ahn, R.M. Wallace, Y.J. Chabal, M.J. Kim, L. Colombo, K. Cho, J. Kim, Atomic layer deposition of dielectrics on graphene using reversibly physisorbed ozone. ACS Nano **6**, 2722–2730 (2012)
36. A.B.F. Martinson, M.J. DeVries, J.A. Libera, S.T. Christensen, J.T. Hupp, M.J. Pellin, J.W. Elam, Atomic layer deposition of Fe_2O_3 using ferrocene and ozone. J. Phys. Chem. C **115**, 4333–4339 (2011)
37. X. Li, N.C. Fan, H.J. Fan, A micro-pulse process of atomic layer deposition of iron oxide using ferrocene and ozone precursors and Ti-doping. Chem. Vap. Deposition **19**, 104–110 (2013)
38. X.-C. Dong, H. Xu, X.-W. Wang, Y.-X. Huang, M.B. Chan-Park, H. Zhang, L.-H. Wang, W. Huang, P. Chen, 3D graphene-cobalt oxide electrode for high-performance supercapacitor and enzymeless glucose detection. ACS Nano **6**, 3206–3213 (2012)
39. J.M. Calleja, M. Cardona, Resonant Raman scattering in ZnO. Phys. Rev. B **16**, 3753–3761 (1977)
40. A.C. Ferrari, J. Robertson, Interpretation of Raman spectra of disordered and amorphous carbon. Phys. Rev. B **61**, 14095–14107 (2000)
41. T. Fujii, F.M.F. de Groot, G.A. Sawatzky, F.C. Voogt, T. Hibma, K. Okada, In situ XPS analysis of various iron oxide films grown by NO_2-assisted molecular-beam epitaxy. Phys. Rev. B **59**, 3195–3202 (1999)
42. X. Jia, Z. Chen, X. Cui, Y. Peng, X. Wang, G. Wang, F. Wei, Y. Lu, Building robust architectures of carbon and metal oxide nanocrystals toward high-performance anodes for lithium-ion batteries. ACS Nano **6**, 9911–9919 (2012)
43. C. He, S. Wu, N. Zhao, C. Shi, E. Liu, J. Li, Carbon-encapsulated Fe_3O_4 nanoparticles as a high-rate lithium ion battery anode material. ACS Nano **7**, 4459–4469 (2013)
44. E. Frackowiak, F. Béguin, Electrochemical storage of energy in carbon nanotubes and nanostructured carbons. Carbon **40**, 1775–1787 (2002)
45. J. Jiang, J. Luo, J. Zhu, X. Huang, J. Liu, T. Yu, Diffusion-controlled evolution of core-shell nanowire arrays into integrated hybrid nanotube arrays for Li-ion batteries. Nanoscale **5**, 8105–8113 (2013)
46. Z. Wang, D. Luan, S. Madhavi, Y. Hu, X.W. Lou, Assembling carbon-coated alpha-Fe_2O_3 hollow nanohorns on the CNT backbone for superior lithium storage capability. Energy Environ. Sci. **5**, 5252–5256 (2012)
47. X. Huang, J. Chen, Z. Lu, H. Yu, Q. Yan, H.H. Hng, Carbon inverse opal entrapped with electrode active nanoparticles as high-performance anode for lithium-ion batteries. Sci. Rep. **3**, 1–9 (2013)
48. Y. Yu, C.H. Chen, J.L. Shui, S. Xie, Nickel-foam-supported reticular CoO-Li_2O composite anode materials for lithium ion batteries. Angew. Chem. Int. Edit. **44**, 7085–7089 (2005)
49. S. Laruelle, S. Grugeon, P. Poizot, M. Dolle, L. Dupont, J.M. Tarascon, On the origin of the extra electrochemical capacity displayed by MO/Li cells at low potential. J. Electrochem. Soc. **149**, A627–A634 (2002)

Chapter 4
Graphene Foam (GF)/Carbon Nanotubes (CNTs) Hybrid Film-Based High-Performance Flexible Asymmetric Supercapacitors

In Chap. 3, graphene foam (GF) has been described to be an attractive scaffold for flexible electrodes. However, bearing in mind that high active material loading with good electric/mechanical contact in electrodes is critically important for high-performance flexible devices, the relatively low active material loading results from insufficient surface area of GF limits the practical applications of GF as efficient electrode support for flexible and lightweight energy storage devices. In order to further increase active material loading, a facile approach was developed for fabricating a novel 3D electrode support consisting of graphene foam (GF) with covalently bonded carbon nanotubes (CNTs) in this chapter. This hybrid structure extends the 2D plane of Graphene into 3D directions without sacrificing electric conductivity and mechanical integrity. The asymmetric supercapacitors (ASCs) based on the unique GF/CNTs hybrid films deliver high energy/power density and good cycling stability in addition to good mechanical flexibility.

4.1 Introduction

Carbon is a fascinating material that exists in various structural forms by different hybridization ways of atomic orbitals (sp^2 and sp^3). There are many different kinds of low-dimensional carbon allotropes, such as zero-dimensional fullerenes, one-dimensional carbon nanotubes and two-dimensional graphene, in addition to bulk phases of carbon (graphite, diamond) [1, 2]. The diversity of microstructures and bonding types ensures versatility in properties and applications for various carbon allotropes [3, 4]. The hybrid structures of different carbon materials would no doubt further extend the diversity of carbon-based micro-/macrostructures, with integrated properties inheriting from the each constituent structure. Indeed hybrid

J. Liu, *Graphene-Based Composites for Electrochemical Energy Storage*,
Springer Theses, DOI 10.1007/978-981-10-3388-9_4

structures such as CNTs/fullerenes [5], CNTs/carbon film [6], graphene/CNTs [7–10], and graphene/fullerenes [11], have displayed improved physical/chemical performance over their single component, benefiting from the synergistic effects. These hybrid structures have found wide applications in sensors, drug delivery, nanoelectronics, and energy storage and conversion [12–18]. Theoretical calculation [19, 20] predicated that covalently bonded carbon nanotubes and graphene could lead to superior properties in three dimensions without sacrificing inherited properties in the planer and axial directions. Such hybrid structures would be of particular interest for many applications, especially for implementation in microelectronics and microelectrochemical devices because of good electrical conductivity [21], large specific surface area [22], unique heterogeneous electron transfer and charge carrier rates, and good electrochemical stability [23].

Many approaches, including solution-based processes [9, 12, 24], microwave irradiation [25], and chemical vapor deposition [4, 7, 26–28], have been attempted to prepare high-quality graphene/CNTs hybrid electrodes. You et al. [24] and Yu and Dai [29] synthesized Graphene/CNTs hybrid films with improved electrochemical performance as supercapacitor electrodes via simple liquid phase mechanical mixing approach. However, these kinds of hybrid films exhibit poor electric/mechanic connection between CNTs and graphene, which limits their application in fast charge/discharge power devices. The synthesis of high-quality graphene/CNTs hybrid materials with strong bonding connection among them is therefore highly desirable. *In situ* growth by chemical vapor deposition has been proved to be an effective approach to achieve this. For example, graphene/CNTs hybrid films with good flexibility and electrical conductivity have been synthesized via vertically growing CNTs arrays on catalyst-patterned graphene films [8]. Recently, Zhu and coworkers [26] have demonstrated the covalently-bonded graphene/CNTs hybrid films. Similar results were also reported via the CVD growth of CNTs on nickel-supported graphene [30]. Noted that CNTs are grown only on the graphene surfaces where the catalyst particles are deposited by e-beam evaporation or dip-coating in the above-mentioned studies. The insufficient surface area of these graphene/CNTs hybrid films makes them challenging to achieve high mass loading of electroactive materials per unit area. Therefore, it is highly desirable to design graphene/CNTs hybrid films with strongly electric/mechanical connected and large quantity of CNTs that could substantially extend the porous architecture and enlarge the surface area.

Herein, a unique 3D architecture that consists of carbon nanotubes (CNTs) and graphene foam (GF) has been designed, aiming to increase the amount of CNTs and the subsequent mass loading of electroactive materials while maintaining the good electric/mechanic contact between CNTs and graphene. The catalytic chemical vapor deposition is chosen for the growth of CNTs onto GF. A hydrothermal method is adopted to deposit catalysts onto GF to improve the subsequent loading of CNTs substantially. Asymmetric supercapacitors (ASCs) based on GF/CNTs/MnO_2 positive electrode and GF/CNTs/Ppy negative electrode have been fabricated and demonstrated good electrochemical performance.

4.2 Experiment

4.2.1 Material Synthesis and Device Fabrication

Synthesis of Graphene Foam (GF). Chemical vapor deposition was chosen for the growth of GF on nickel foam [31].

Synthesis of Graphene Foam (GF)/Carbon nanotubes (CNTs) Hybrid Films. GF severs as the template for the subsequent growth of CNTs. A hydrothermal method is adopted for the deposition of the NiCo catalyst. The CNT growth is carried out at 750 °C. The gas flow rate of C_2H_4, H_2 and Ar is 20, 40 and 100 sccm, respectively.

Synthesis of GF/CNTs/MnO_2 Hybrid Films. MnO_2 nanosheets is prepared via hydrothermal method [32]. The samples are denoted as GF/CNTs/MnO_2-n, where n is the loading amount of MnO_2 (mg/cm^2).

Synthesis of GF/CNTs/Polypyrrole (Ppy) Hybrid Films. A chemical polymerization method is adopted for the synthesis of the GF/CNTs/Ppy hybrid films [33]. The samples are referred as GF/CNTs/Ppy-m. m is the amount of pyrrole monomer (μl) used during the synthesis.

Assemble of GF/CNTs/MnO_2//GF/CNTs/Polypyrrole (Ppy) Asymmetric Supercapacitors (ASCs). ASCs were assembled using an electrolyte-soaked (0.5 M Na_2SO_4) separator sandwiched between a piece of GF/CNTs/MnO_2 (1×4 cm^2) and a piece of GF/CNTs/Ppy (1×4 cm^2). The ASC devices are denoted as ASC-n, where n is the loading amount of MnO_2 (mg/cm^2).

4.2.2 Material Characterization

Structure and Morphology Characterization. Field-emission scanning electron microscopy (FESEM, JEM-6700F, 10.0 kV), Transmission electron microscopy (TEM, JEM-2010, 200 kV), Raman spectroscopy (Renishaw, 532 nm excitation laser).

Electrochemical Performance Evaluation. Cyclic voltammetry (CV) curves, Galvanostatic charge/discharge profiles, and electrochemical impedance spectroscopy (EIS, 100 kHz–0.01 Hz) were collected using CHI 760D workstation. Three-electrode system (working electrode: GF/CNTs/MnO_2 or GF/CNTs/Ppy; reference electrode: saturated Ag/AgCl; Counter electrode: Pt plate) was chosen for individual electrodes' testing. The EIS results are fitted via the software Z-View. Two-electrode system is adopted for the ASCs' testing.

The areal capacitance of the individual electrode is calculated from the corresponding CV curves:

$$C = \frac{1}{s\,v\Delta V} \int_{V_0}^{V_0+\Delta V} IdV$$

where I(A) is the response current, v is the scan rate (V/s), s is the apparent surface area (cm^2), V_0 is the lower potential limit, and ΔV is potential window (V).

The areal capacitance (C_s, F/cm^2) and specific capacitance (C_m, F/g) of ASCs are calculated from corresponding charge/discharge curves:

$$C_s = 4\frac{I}{s}\frac{dt}{dV} \quad or \quad C_m = 4\frac{I}{m}\frac{dt}{dV}$$

The equation: $C_- V_- = C_+ V_+$, is used for the charge match between two electrodes. The energy density (E) and power density (P) are calculated according to the equations [18]:

$$E = CV_{\max}^2/8$$

$$P = V_{max}^2/(4m R_{ESR})$$

$$R_{ESR} = V_{drop}/(2I)$$

where V_{max} is the maximum voltage of the ASC, R_{ESR} is the equivalent series resistances.

4.3 Results and Discussions

4.3.1 Fabrication of GF/CNTs Hybrid Films

Figure 4.1 schematically illustrates the synthesis procedure of the GF/CNTs hybrid film. Three steps are involved: (i) GF is deposited on nickel foam via catalytic decomposing of CH_4 at 1000 °C (Fig. 4.1a, b). Self-supported GF with intact 3D microstructure is collected via etching nickel substrate (Fig. 4.1c). The areal density of GF could be controlled easily via adjusting growth conditions. (ii) The uniform coating of NiCo-catalyst precursor on GF is achieved via a facile hydrothermal process (Fig. 4.1d). The high loading of NiCo catalysts ensures the large quantity growth of CNTs subsequently, and hence the large surface-to-volume ratio of the GF/CNTs hybrid film. Little defects are introduced, suggesting that the high quality of GF could be well maintained during hydrothermal method process. (iii) GF/NiCo-precursor is converted to GF/$NiCo_2O_4$ by heated in air at 350 °C prior to the growth of CNTs (Fig. 4.1e). This could effectively prevent NiCo catalyst particles from agglomeration at high temperatures, and provide more catalytic sites for the growth of CNTs. The $NiCo_2O_4$ nanoneedles are then reduced to form well dispersed catalyst islands in the presence of H_2, and further catalyze the decomposition of C_2H_4 to form 3D GF/CNTs framework (Fig. 4.1f). During the synthesis process, apparent color change could be detected, while the macroscopic 3D framework is well preserved.

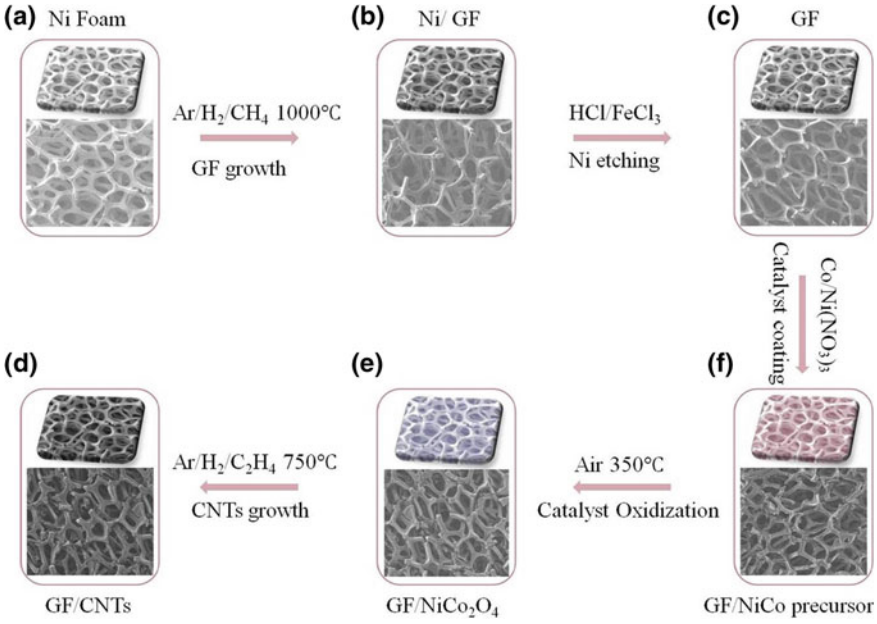

Fig. 4.1 Illustration of the growth procedure of GF/CNTs hybrid films

Large sized GF/CNTs hybrid film with good flexibility were prepared based on the above approach (Fig. 4.2a1–a2). The well-defined interconnected network structure of GF/CNTs hybrid film, with a layer of entangled CNTs that surrounding around graphene tightly is detected in Fig. 4.2b and c. The multi-walled CNTs, displays about 15–20 walls, 20–25 nm in diameter and a few hundred nanometers to several micrometers in length (Fig. 4.2d, e, f). A bamboo-like structure with complete knots (indicated by the white arrow) is clearly observed from the inset in Fig. 4.2e, because of the growth of a complete inner graphene layer prior to contraction of the catalyst particle [34, 35]. SEM image (Fig. 4.2d) and TEM images (Fig. 4.2e, f) reveal that most of catalyst particles located at the top of CNTs, corroborating a tip-growth mechanism for the CNTs growth [36]. This feature also further verifies the excellent electric/mechanical interconnection between GF and CNTs. Moreover, there are CNTs on the outer and inner surfaces of GF backbones (Fig. 4.2g). This provides large surface-to-volume ratio for the subsequent electroactive materials deposition. The absence of the D peak at 1350 cm^{-1} in the spectrum of GF corroborates the high quality of GF (Fig. 4.2h) [37]. A sharp D peak appears after CNTs growth, resulting from the generation of defects during growth process. The introduce of defects was also verified via the corresponding SAED patterns [38]. Nevertheless, GF/CNTs hybrid film exhibits a sheet resistance of 191 Ω/sq (178 S/m), which is much smaller than that of pure GF (352 Ω/sq, 101 S/m), corroborating the good electrical conductivity of GF/CNTs hybrid film. As expected, the 3D architecture of GF is well extended by the densely grown CNTs.

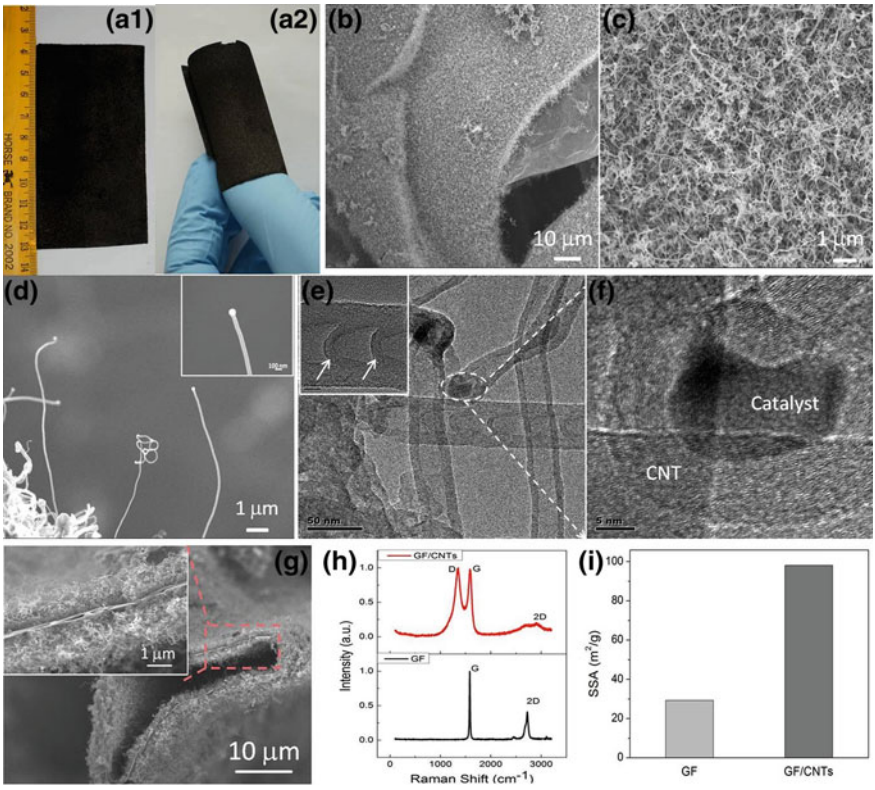

Fig. 4.2 **a**1–**a**2 Representative photograph of the film. **b**–**d** Typical FESEM images. **e**, **f** TEM images. **g** Cross-sectional images. **h** Raman spectra. **i** Comparative specific surface area (SSA). Inset of (**d**) suggests the tip-growth mechanism for CNTs. The bamboo-like structure is identified in the inset of (**e**). The uniform growth of CNTs on both *outer* and *inner* surfaces of GF branches is illustrated in inset of (**g**). Figure reproduced from Ref. [32]

The GF/CNTs hybrid film exhibits significant increase in surface area (98 m^2/g *vs.* 30 m^2/g for GF) (Fig. 4.2i) [37]. It should be stressed that, the GF/CNTs hybrid films with different CNTs mass loading could be easily prepared by adjusting the growth conditions, offering the possibility to further optimize this kind of hybrid film.

4.3.2 *Fabrication of GF/CNTs/MnO_2 and GF/CNTs/Ppy Hybrid Films*

Figure 4.3a and c reveal the nanostructure of the GF/CNTs/MnO_2 hybrid film, where CNTs are uniformly surrounded by flower-like MnO_2 nanosheets, forming

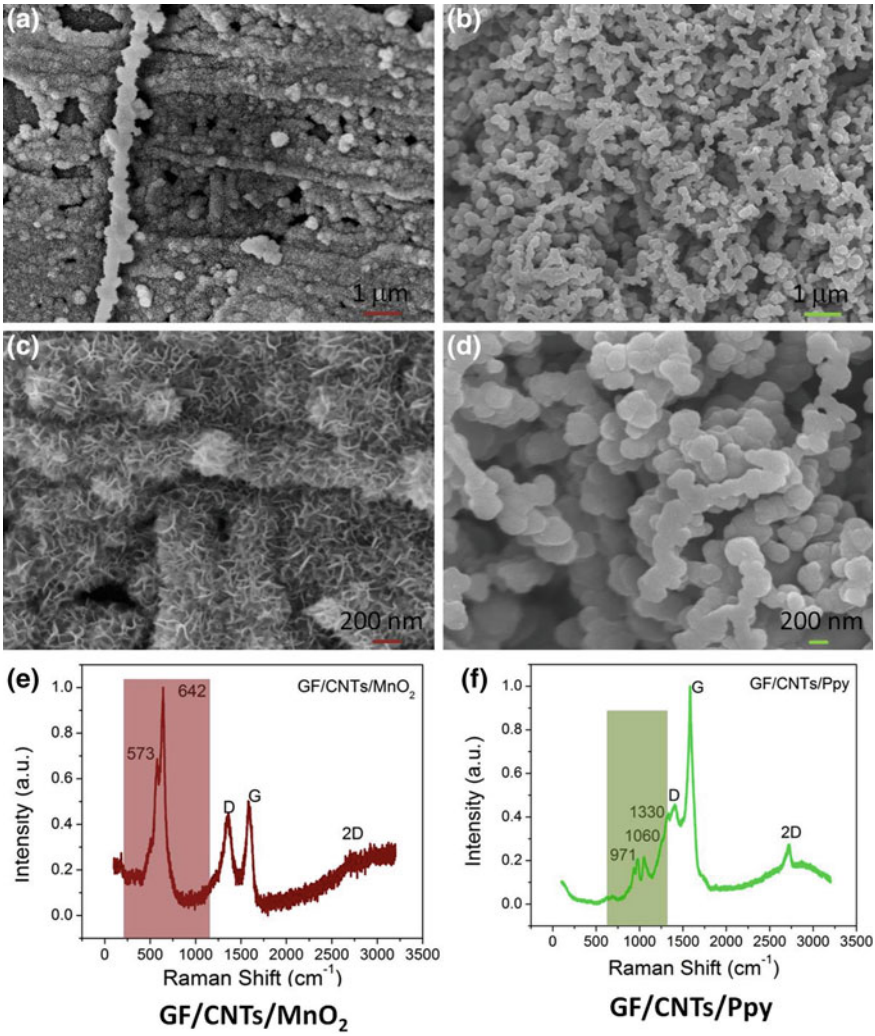

Fig. 4.3 Representative FESEM images of GF/CNTs/MnO_2 (**a**, **c**) and GF/CNTs/Ppy (**b**, **d**). Raman spectra of GF/CNTs/MnO_2 (**e**) and (**f**) GF/CNTs/Ppy

unique CNTs (core)-MnO_2 (shell) nanostructure. A highly porous network was assembled by the flower-like MnO_2 nanosheets with thickness of a few nanometers (Fig. 4.3a, c). The successful deposition of MnO_2 is further verified by the appearance of typical MnO_2 Raman peaks at 568 cm^{-1}, 640 cm^{-1} as well as the decrease in intensity of G peak (Fig. 4.3e) [39]. This hybrid electrode design provides better current collector/active materials contact, and ensures large accessible surface area and fast mass transfer for electrolyte. It is also found that the introduction of CNTs in the GF is crucial to achieve high loading of active

materials. For example, the areal density of MnO_2 of GF/CNTs/MnO_2 film is 6.2 mg/cm^2 (at 0.6 mM manganese source), which is 6 folds of that of GF/MnO_2 film. The relatively high and adjustable mass loading of electroactive MnO_2 on GF/CNTs hybrid film offers the opportunity to optimize the electrochemical performance of the assembled ASC devices further.

Conducting polymers/graphene composites have been investigated intensively as promising electrode materials for supercapacitors [40, 41]. GF/CNTs/Polypyrrole (Ppy) hybrid film was prepared, and used as the negative electrode to match with the GF/CNTs/MnO_2 hybrid film positive electrode here. The in situ chemical polymerization is chosen for achieving the conformal coating of Ppy on GF/CNTs film (Fig. 4.3b, d) [33]. Corresponding Raman spectrum corroborates the synthesis of Ppy with characteristic peaks at 971, 1060 and 1330 cm^{-1} (Fig. 4.3f). A series of samples with different polypyrrole loading amounts were prepared to optimize the electrochemical performance of GF/CNTs/Ppy hybrid film.

4.3.3 *Electrochemical Performance of GF/CNTs/MnO_2 and GF/CNTs/Ppy Hybrid Electrodes*

The electrochemical performance of individual electrode is investigated in a three-electrode system. The electrolyte is 0.5 M Na_2SO_4 aqueous solution. The self-supported hybrid film is used as the working electrode directly because of its good electric conductivity and mechanical integrated structure. To investigate the contribution of MnO_2 to the capacitance in the hybrid electrode and optimize the mass loading of MnO_2, a series of CV curves are collected at different sweep rates (Fig. 4.4a, b). The current response increases with the increase in MnO_2 mass loading density from 0.6 to 6.2 mg/cm^2, indicating an increase in the total capacitance [42]. However, the total capacitance decreases when the mass loading density of MnO_2 further increases to 8.4 mg/cm^2. The areal capacitance *vs.* mass density plots in Fig. 4.4e further support the presence of optimal mass loading density. In which the GF/CNTs/MnO_2-8.4 sample displays a lower areal capacitance compared to the sample GF/CNTs/MnO_2-6.2, especially at low sweep rates. Electrochemical impedance spectroscopy (EIS) measurements were conducted to understand the inferior performance of GF/CNTs/MnO_2-8.4 mg/cm^2 (Fig. 4.4f). The impedance data is fitted with an equivalent electrical circuit consisting of the electrolyte resistance (R_s), charge transfer resistance (or polarization resistance, R_{ct}), Warburg element (W) and constant phase element (CPE) (inset in Fig. 4.4f) [43, 44]. The charge transfer resistance (R_{ct}) is found to increase with the increase of mass loading density. There are two factors accounting for this trend: (i) the poor intrinsic electrical conductivity of MnO_2, and (ii) the increase in the thickness of MnO_2 layer that impedes the ion diffusion and migration process. Interestingly, R_{ct} increases slightly

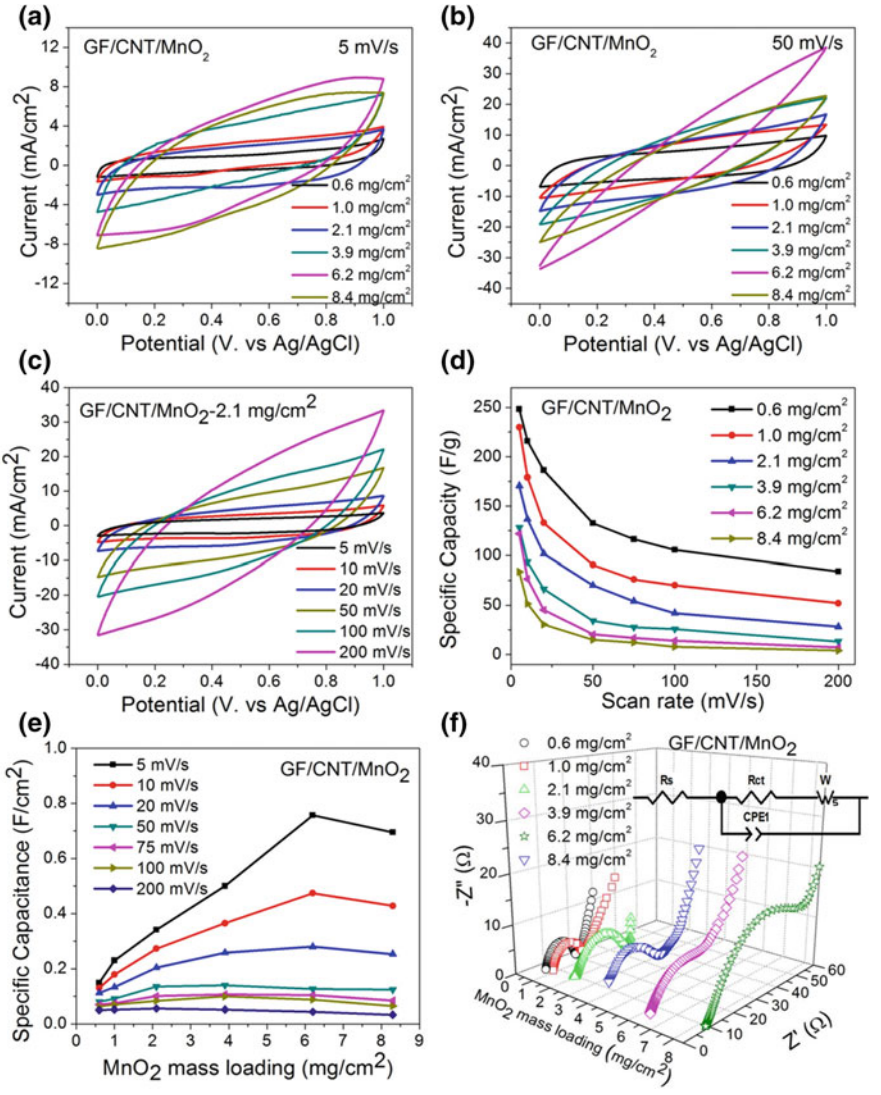

Fig. 4.4 CV curves of GF/CNTs/MnO_2 hybrid films with different loading of MnO_2 (from 0.6 to 8.4 mg/cm^2) at the sweep rate of 5 mV/s (**a**) and 50 mV/s (**b**). **c** Rate-dependent CV curves of GF/CNTs/MnO_2-2.1 hybrid film. **d** Specific capacitance versus sweep rate for GF/CNTs/MnO_2 hybrid films with different loading of MnO_2. **e** Areal capacitance versus mass loading for GF/CNTs/MnO_2 hybrid films at different sweep rates. **f** Corresponding Nyquist plots of GF/CNTs/MnO_2 hybrid films. An equivalent electrical circuit consisting of the electrolyte resistance (R_s), interface charge transfer resistance (R_{ct}), Warburg element (W) and constant phase element (CPE), is illustrated in the inset of (**f**). Figure reproduced from Ref. [32]

with the increase of MnO_2 mass loading from 0.6 to 6.2 mg/cm^2, but jumps sharply from 31.6 Ω (for GF/CNTs/MnO_2-6.2) to 56.2 Ω (for GF/CNTs/MnO_2-8.4). This phenomenon excludes the effect of factor i) to some extent, and the factor ii) takes the main responsibility for the sharp increase in R_{ct} when the thickness of MnO_2 layer is close to the diffusion length of Na^+ at these sweep rates [45]. Typically, the ion diffusion length in GF/CNTs/MnO_2 hybrid films decreases as the sweep rate increases, thus giving rise to the decrease in the optimal mass loading density. For example, the optimal mass loading density at 75 mV/s is 3.9 mg/cm^2 whereas it is 2.1 mg/cm^2 at 200 mV/s.

A series of rate-dependent CV curves of GF/CNTs/MnO_2-2.1 hybrid film are plotted to investigate the effect of sweep rates on electrochemical performance (Fig. 4.4c). The CV curves deviate from a rectangular shape of ideal double-layer capacitors, resulting from the relatively large resistance and overpotential [42]. The specific capacitance and areal capacitance of the GF/CNTs/MnO_2 hybrid films are calculated and plotted (Fig. 4.4d, e). The high specific capacitance of 215 F/g (Fig. 4.4d), which corresponds to 130 mF/cm^2 (Fig. 4.4e), is obtained for sample GF/CNTs/MnO_2-0.6 at a sweep rate of 10 mV/s. The value is higher than those of MnO_2-based electrodes in previous reports, such as 62 mF/cm^2 at 5 mA/cm^2 for PEDOT/MnO_2 [46], 70 mF/cm^2 at 2 mA/cm^2 for TiO_2/MnO_2 [47], 64 mF/cm^2 at 0.08 mA/cm^2 for SnO_2/MnO_2 [48], 41 mF/cm^2 at 0.12 mA/cm^2 for TiN/MnO_2 coaxial arrays [49], 105 mF/cm^2 at 0.06 mA/cm^2 for WO_{3-x}/Au/MnO_2 nanowire [50] and comparable to that of hydrogenated ZnO/MnO_2/Carbon cloth (138.7 mF/cm^2 at 1 mA/cm^2) [51]. A high capacitance of 106 F/g (63 mF/cm^2) could be retained, even at a high sweep rate of 100 mV/s. Moreover, the GF/CNTs/MnO_2 hybrid film displays good cycling performance with nearly overlapped CV curves after 5000 cycles.

Similar to GF/CNTs/MnO_2 hybrid films, the current responses in the CV curves of GF/CNTs/Ppy hybrid films increase when more Ppy were deposited, resulting from the increased amount of active materials that contribute to the total capacitance (Fig. 4.5a, b). Typical CV curves deviate from an ideal rectangular shape, especially with high Ppy loading and at high sweep rates (Fig. 4.5c, d). Interestingly the difference in the areal capacitance for GF/CNTs/Ppy hybrid films is smaller particularly at high sweep rates (Fig. 4.5e), due to the reduced ion diffusion length and increased R_{ct}, as discussed for the case of GF/CNTs/MnO_2 hybrid films. The EIS results of GF/CNTs/Ppy hybrid films (Fig. 4.5f) shows slight decrease initially, and followed with the increase in R_{ct} when Ppy loading increase gradually. The theoretic calculation indicates that the resistance of CNTs network usually comes from CNT/CNT junctions [52]. The slight decrease in R_{ct} is probably resulting from the uniform coating of Ppy onto the GF/CNTs film that improves the electric conductivity between CNT/CNT junctions [53]. However, further increasing the Ppy loading blocks the ion diffusion and migration process eventually, giving rise to the increase of R_{ct} from 10.7 Ω for GF/CNTs/Ppy-1000 to 28.6 Ω for GF/CNTs/Ppy-2000.

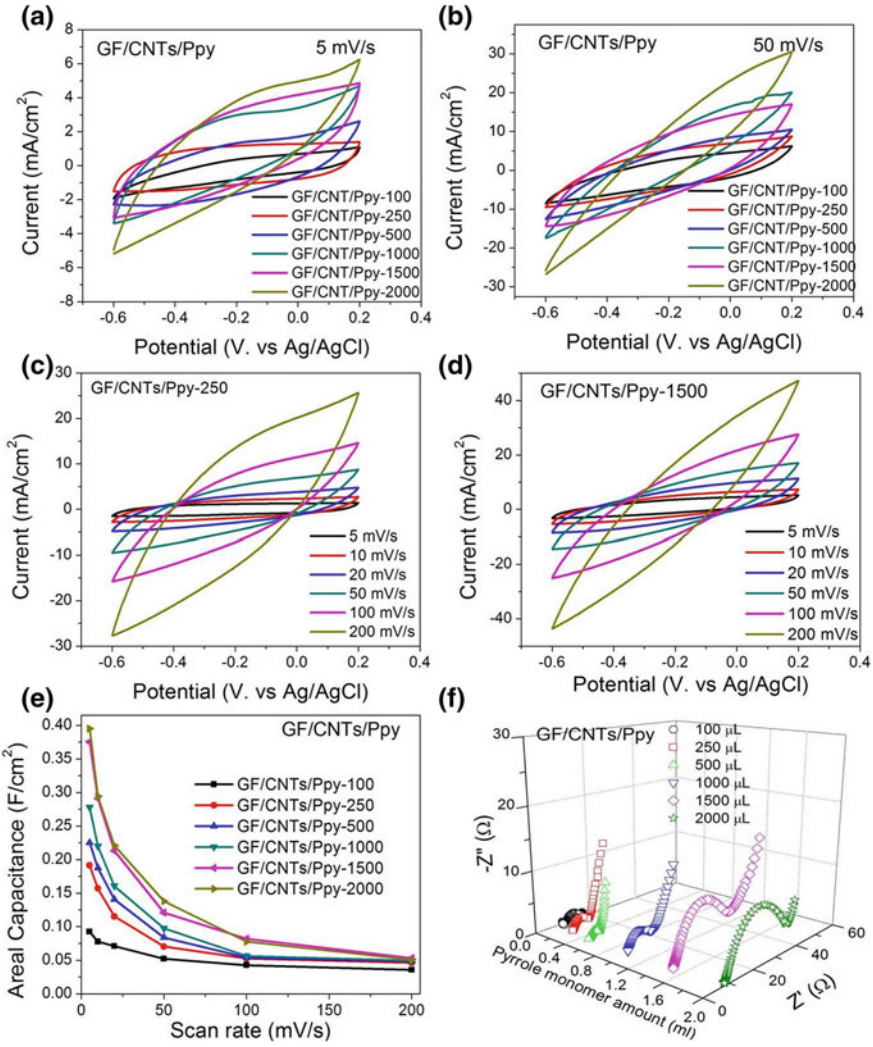

Fig. 4.5 Comparative CV curves of GF/CNTs/Ppy hybrid films at sweep rates of **a** 5 mV/s and **b** 50 mV/s. CV curves of **c** GF/CNTs/Ppy-250 and **d** GF/CNTs/Ppy-1500 measured at different sweep rates. **e** The plot of Areal capacitance versus sweep rate and Nyquist plot (**f**) of GF/CNTs/Ppy hybrid films

4.3.4 Electrochemical Performance of GF/CNTs/MnO_2// GF/CNTs/Ppy ASCs

The charge balance between positive electrode and negative electrode is crucial to maximize the energy density of ASCs [54]. Based on the results above, two couples of electrodes that exhibiting close total amount of charge in a wide range of sweep

rates, were chosen for the fabrication of ASC-0.6 and ASC-2.1, respectively. The weight ratio of positive electrode (MnO_2) and negative electrode (Ppy) is 1.2:1 for ASC-0.6 and 1.3:1 for ASC-2, respectively.

The ASC device, consisting of an electrolyte-soaked separator sandwiched by positive and negative electrodes, is illustrated schematically in Fig. 4.6a. Two pieces of poly(ethylene terephthalate) (PET) sheets were used as the flexible substrates. Considering the working window of GF/CNTs/MnO_2 and GF/CNTs/Ppy hybrid films are 0–1.0 V and −0.6–0.2 V, respectively (Fig. 4.6b), the ASC device is expected to work stably over a voltage window of 0–1.6. Figure 4.6c illustrates the CV curves with different working windows. Note that the maximal voltage window of 1.6 V exceeds the theoretical decomposition voltage of water (1.23 V), resulting from the high overpotential of hydrogen evolution on the GF/CNTs/Ppy hybrid electrode. CV curves of ASC-2.1 were plotted in Fig. 4.6d. The assembled full cell exhibits quasi-rectangular CV curves at low sweep rates, agreeing with a

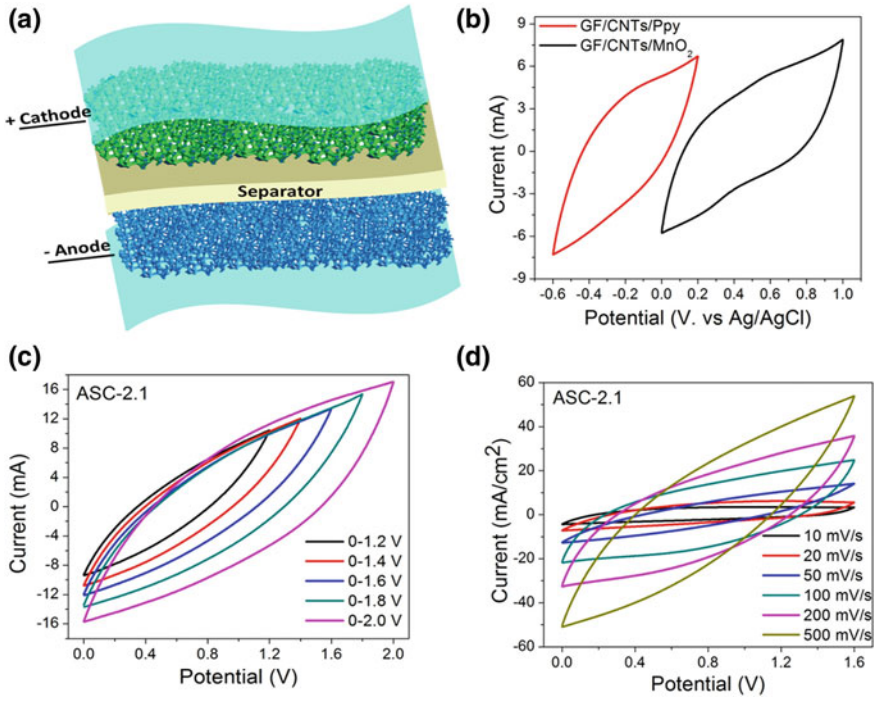

Fig. 4.6 **a** Schematic illustration of an ASC that consists of GF/CNTs/MnO_2 positive electrode, electrolyte-soaked separator and GF/CNTs/Ppy negative electrode. **b** CV curves of GF/CNTs/MnO_2 and GF/CNTs/Ppy half cells in 0.5 M Na_2SO_4 solution at a sweep rate of 20 mV/s. **c** CV curves of ASC-2.1 measured with different potential windows (at 50 mV/s). CV curves of ASC-2.1 (**d**) measured between 0 and 1.6 V with sweep rates ranging from 10 to 500 mV/s. Figure reproduced from Ref. [32]

good capacitive behavior [55]. The CV curves remain symmetrical even at a high sweep rate of 500 mV/s, corroborating the good reversibility of electrochemical processes.

Figure 4.7a illustrates the typical galvanostatic charge/discharge curves of the fabricated full cell. The charge-discharge curves deviate from the linear voltage-time relation, suggesting pseudo-capacitive behavior involved in the hybrid electrodes [56]. The ASC-2.1 exhibits a Coulombic efficiency of 74-85%, while the value for ASC-0.6 is above 95% at the current density of 1–3 mA/cm^2. There are two possibilities that may contribute to the relatively low Coulombic efficiency: (i) ASC-2.1 exhibits large resistance with high mass loading; and ii) some unavoidable electrolysis of water take place because of the high working voltage. The Ragone plots of the ASCs, showing energy and power density of the devices, are shown in Fig. 4.7b. ASC-2.1 exhibits a maximum energy density of 22.8 Wh/kg at 860 W/kg and a high power density of 2.7 kW/kg at 6.2 Wh/kg. ASC-0.6 delivers better rate performance, with a maximum energy density of 22.2 Wh/kg at

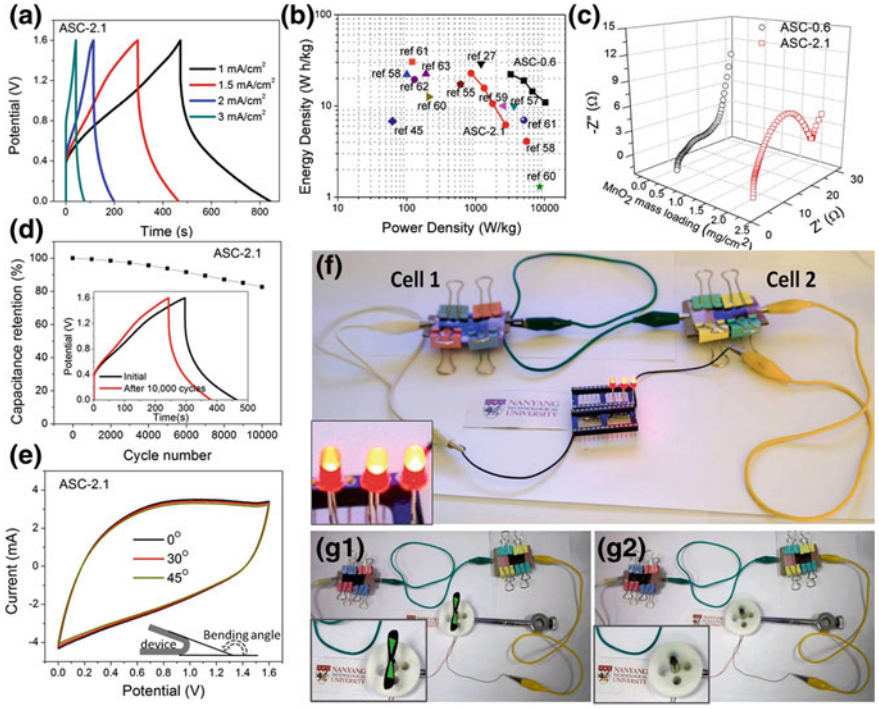

Fig. 4.7 **a** Galvanostatic charge/discharge curves of ASC-2.1 at different current densities. **b** Ragone plot of the ASCs and some other reported devices. **c** Nyquist plots for ASC-2.1 and ASC-0.6. **d** Cycling performance of ASC-2.1 at a current density of 1.5 mA/cm^2 for 10,000 cycles. Inset of **d** shows the charge/discharge curves for the 1st and 10,000th cycles. **e** CV curves of ASC-2.1 at different bending angles. Optical images show two ASCs connected in series powering **f** LEDs and **g** a small rotation motor. Figure reproduced from Ref. [32]

a power density of 3.2 kW/kg. Even at a high power density of 10.3 kW/kg, ASC-0.6 still displays an energy density of 10.9 Wh/kg. This is superior to that of many other MnO_2-based symmetric or asymmetric supercapacitors [45, 55, 57–63], as given in the same plot for comparison. The fast charge transport and lower resistance of ASC-0.6 may account for its superior rate performance over ASC-2.1, as revealed by the EIS results in Fig. 4.7c. In which, a typical diffusion-controlled Warburg capacitive behavior with a diagonal line in the low frequency region and small depressed semicircle in the high frequency region [43, 44], have been observed. The series resistance of the devices is estimated to be 17. 7 Ω (R_s, 1.6 Ω; R_{ct}, 16.1Ω) for ASC-0.6 and 26.4 Ω for ASC-2.1 (R_s, 6.4 Ω; R_{ct}, 20.0 Ω). The relatively small values of the serial resistances also corroborate the compact fabrication that ensures fast charge transfer in the cell. The overall volumetric and gravimetric energy and power densities were calculated based on the packaged cell configuration. The ASC-2.1 and ASC-0.6 deliver a maximum volumetric energy density of 8.7 and 2.7 Wh/L, respectively, based on the fully packaged cell. The value is quite satisfactory, and higher than reported MnO_2-based ASCs [63] and Ni $(OH)_2$-based ASCs [64]. In addition, decent volumetric power densities of 1.2 kW/L for ASC-0.6 and 1.0 kW/L for ASC-2.1 have been delivered. The ASCs also display good cycling stability. Specially, high capacitance retentions of 90.2% for ASC-0.6 and 83.5% for ASC-2.1 (Fig. 4.7d) were reported, even after 10,000 charge/discharge cycles, which are comparable with or better than those of previously reported ASCs [65–67].

The development of multifunctional flexible electronics promotes increasing demands for power sources that are lightweight and flexible in addition to good electrochemical performance. To explore the practical application of our ASCs as flexible power source, the assembled cell was mechanically bended during the CV measurements (Fig. 4.7e). Under different bending angles, perfectly overlapped CV curves and similar specific capacitance are reported. This suggests that the device could be bent to a large extent without degrading the performance, benefiting from the flexible feature and good integrity of the hybrid electrodes. By connecting two pieces of packaged cells in series, output voltage window of 3.2 V was achieved. The ASC could power three red LEDs (1.8 V, 20 mA, 5 mm diameter) after charging for only 30 s (Fig. 4.7f) or even drive a small rotation motor (3 V, 0.45 W) with charging for only a few seconds (Fig. 4.7g).

4.3.5 Underlying Mechanism for Enhanced Electrochemical Performance

The performance of the ASCs designed in this work is quite satisfactory, especially considering the relatively high and tunable loading density of electroactive materials. The unique design of the 3D interconnected nanostructure of the flexible electrodes may account for the enhanced performance. Specifically, the densely grown CNTs extend the 3D architecture of GF to offer a large surface-to-volume

ratio that allows high active materials loading, and also provides good electric/mechanical contact within the hybrid films. Serving as current collector and mechanical supports, the GF/CNTs hybrid films ensures short diffusion length for ions, facile transfer pathways for electrons, and good integrity for active materials. Moreover, relative large mass fraction of electroactive materials is achieved, benefiting from the lightweight and highly porous feature of the GF/CNTs film and the additive-free design of the electrodes. Such electrodes would surely lead to a high energy density of real ASCs in practice, and show apparent advantages over those conventionally prepared with additives (e.g., carbon black and binder) and planar or 3D metallic current collectors. Additionally, the proper selection of positive/negative electrode materials as well as the well charge balance between the two electrodes also contribute to the good performance of ASCs [32].

4.4 Conclusion

In conclusion, novel GF/CNTs hybrid films with unique 3D architecture and large surface-to-volume ratio, and are flexible and lightweight were prepared. Using the hybrid films as electrode supports for the deposition of pseudo-capacitive materials, lightweight and flexible asymmetric supercapacitors (ASCs) have been fabricated. The good performance in terms of energy/power densities, cycling stability and flexibility have been demonstrated by the ASCs. This is attributed to the unique 3D nanostructure of the integrated electrodes, which allows high loading of electroactive materials and ensures facile charge transport. Such ASCs would be promising high-performance power source for flexible electronics.

References

1. X. Li, X.B. Zang, Z. Li, X.M. Li, P.X. Li, P.Z. Sun, X. Lee, R.J. Zhang, Z.H. Huang, K.L. Wang, D.H. Wu, F.Y. Kang, H.W. Zhu, Large-area flexible core-shell graphene/porous carbon woven fabric films for fiber supercapacitor electrodes. Adv. Funct. Mater. **23**, 4862–4869 (2013)
2. Y.P. Zhai, Y.Q. Dou, D.Y. Zhao, P.F. Fulvio, R.T. Mayes, S. Dai, Carbon materials for chemical capacitive energy storage. Adv. Mater. **23**, 4828–4850 (2011)
3. C.N.R. Rao, A.K. Sood, K.S. Subrahmanyam, A. Govindaraj, Graphene: the new two-dimensional nanomaterial. Angew. Chem. Int. Edit. **48**, 7752–7777 (2009)
4. F. Du, D.S. Yu, L.M. Dai, S. Ganguli, V. Varshney, A.K. Roy, Preparation of tunable 3D pillared carbon nanotube-graphene networks for high-performance capacitance. Chem. Mater. **23**, 4810–4816 (2011)
5. M. Vizuete, M. Barrejon, M.J. Gomez-Escalonilla, F. Langa, Endohedral and exohedral hybrids involving fullerenes and carbon nanotubes. Nanoscale **4**, 4370–4381 (2012)
6. X.M. Liu, K.H.R. Baronian, A.J. Downard, Direct growth of vertically aligned carbon nanotubes on a planar carbon substrate by thermal chemical vapour deposition. Carbon **47**, 500–506 (2009)

7. Z. Fan, J. Yan, L. Zhi, Q. Zhang, T. Wei, J. Feng, M. Zhang, W. Qian, F. Wei, A three-dimensional carbon nanotube/graphene sandwich and its application as electrode in supercapacitors. Adv. Mater. **22**, 3723–3728 (2010)
8. D.H. Lee, J.E. Kim, T.H. Han, J.W. Hwang, S. Jeon, S.Y. Choi, S.H. Hong, W.J. Lee, R.S. Ruoff, S.O. Kim, Versatile carbon hybrid films composed of vertical carbon nanotubes grown on mechanically compliant graphene films. Adv. Mater. **22**, 1247–1252 (2010)
9. Q. Cheng, J. Tang, J. Ma, H. Zhang, N. Shinya, L.-C. Qin, Graphene and carbon nanotube composite electrodes for supercapacitors with ultra-high energy density. Phys. Chem. Chem. Phys. **13**, 17615–17624 (2011)
10. R.K. Paul, M. Ghazinejad, M. Penchev, J. Lin, M. Ozkan, C.S. Ozkan, Synthesis of a pillared graphene nanostructure: a counterpart of three-dimensional carbon architectures. Small **6**, 2309–2313 (2010)
11. D.S. Yu, K. Park, M. Durstock, L.M. Dai, Fullerene-grafted graphene for efficient bulk heterojunction polymer photovoltaic devices. J. Phys. Chem. Lett. **2**, 1113–1118 (2011)
12. M. Beidaghi, C.L. Wang, Micro-supercapacitors based on interdigital electrodes of reduced graphene oxide and carbon nanotube composites with ultrahigh power handling performance. Adv. Funct. Mater. **22**, 4501–4510 (2012)
13. C.Y. Li, Z. Li, H.W. Zhu, K.L. Wang, J.Q. Wei, X.A. Li, P.Z. Sun, H. Zhang, D.H. Wu, Graphene nano-"patches" on a carbon nanotube network for highly transparent/conductive thin film applications. J. Phys. Chem. C **114**, 14008–14012 (2010)
14. Y.W. Cheng, S.T. Lu, H.B. Zhang, C.V. Varanasi, J. Liu, Synergistic effects from graphene and carbon nanotubes enable flexible and robust electrodes for high-performance supercapacitors. Nano Lett. **12**, 4206–4211 (2012)
15. H. Chang, H. Wu, Graphene-based nanocomposites: preparation, functionalization, and energy and environmental applications. Energy Environ. Sci. **6**, 3483–3507 (2013)
16. C. Xu, B. Xu, Y. Gu, Z. Xiong, J. Sun, X.S. Zhao, Graphene-based electrodes for electrochemical energy storage. Energy Environ. Sci. **6**, 1388–1414 (2013)
17. X. Yang, C. Cheng, Y. Wang, L. Qiu, D. Li, Liquid-mediated dense integration of graphene materials for compact capacitive energy storage. Science **341**, 534–537 (2013)
18. X. Wang, Y. Zhang, C. Zhi, X. Wang, D. Tang, Y. Xu, Q. Weng, X. Jiang, M. Mitome, D. Golberg, Y. Bando, Three-dimensional strutted graphene grown by substrate-free sugar blowing for high-power-density supercapacitors. Nat. Commun. **4** (2013)
19. F.D. Novaes, R. Rurali, P. Ordejon, Electronic transport between graphene layers covalently connected by carbon nanotubes. ACS Nano **4**, 7596–7602 (2010)
20. V. Varshney, S.S. Patnaik, A.K. Roy, G. Froudakis, B.L. Farmer, Modeling of thermal transport in pillared-graphene architectures. ACS Nano **4**, 1153–1161 (2010)
21. X. Wang, L.J. Zhi, K. Mullen, Transparent, conductive graphene electrodes for dye-sensitized solar cells. Nano Lett. **8**, 323–327 (2008)
22. M. Pumera, Electrochemistry of graphene: new horizons for sensing and energy storage. Chem. Rec. **9**, 211–223 (2009)
23. D.A.C. Brownson, D.K. Kampouris, C.E. Banks, An overview of graphene in energy production and storage applications. J. Power Sources **196**, 4873–4885 (2011)
24. B. You, L.L. Wang, L. Yao, J. Yang, Three dimensional N-doped graphene-CNT networks for supercapacitor. Chem. Commun. **49**, 5016–5018 (2013)
25. V. Sridhar, H.J. Kim, J.H. Jung, C. Lee, S. Park, I.K. Oh, Defect-engineered three-dimensional graphene-nanotube-palladium nanostructures with ultrahigh capacitance. ACS Nano **6**, 10562–10570 (2012)
26. Y. Zhu, L. Li, C. Zhang, G. Casillas, Z. Sun, Z. Yan, G. Ruan, Z. Peng, A.-R.O. Raji, C. Kittrell, R.H. Hauge, J.M. Tour, A seamless three-dimensional carbon nanotube graphene hybrid material. Nat. Commun. **3**, 1225 (2012)
27. G. Zhu, Z. He, J. Chen, J. Zhao, X. Feng, Y. Ma, Q. Fan, L. Wang, W. Huang, Highly conductive three-dimensional MnO2-carbon nanotube-graphene-Ni hybrid foam as a binder-free supercapacitor electrode. Nanoscale **6**, 1079–1085 (2014)

28. X. Dong, J. Chen, Y. Ma, J. Wang, M.B. Chan-Park, X. Liu, L. Wang, W. Huang, P. Chen, Superhydrophobic and superoleophilic hybrid foam of graphene and carbon nanotube for selective removal of oils or organic solvents from the surface of water. Chem. Commun. **48**, 10660–10662 (2012)
29. D.S. Yu, L.M. Dai, Self-assembled graphene/carbon nanotube hybrid films for supercapacitors. J. Phys. Chem. Lett. **1**, 467–470 (2010)
30. Z. Yan, L. Ma, Y. Zhu, I. Lahiri, M.G. Hahm, Z. Liu, S. Yang, C. Xiang, W. Lu, Z. Peng, Z. Sun, C. Kittrell, J. Lou, W. Choi, P.M. Ajayan, J.M. Tour, Three-dimensional metal–graphene–nanotube multifunctional hybrid materials. ACS Nano **7**, 58–64 (2012)
31. Z.P. Chen, W.C. Ren, L.B. Gao, B.L. Liu, S.F. Pei, H.M. Cheng, Three-dimensional flexible and conductive interconnected graphene networks grown by chemical vapour deposition. Nat. Mater. **10**, 424–428 (2011)
32. J. Liu, L. Zhang, H.B. Wu, J. Lin, Z. Shen, X.W. Lou, High-performance flexible asymmetric supercapacitors based on a new graphene foam/carbon nanotube hybrid film. Energy Environ. Sci. **7**, 3709–3719 (2014)
33. J.L. Liu, W.W. Zhou, L.F. Lai, H.P. Yang, S.H. Lim, Y.D. Zhen, T. Yu, Z.X. Shen, J.Y. Lin, Three dimensionals alpha-Fe_2O_3/Polypyrrole (Ppy) nanoarray as anode for micro lithium ion batteries. Nano Energy **2**, 726–732 (2013)
34. J. Zhu, J. Jia, F.-L. Kwong, D.H.L. Ng, Synthesis of bamboo-like carbon nanotubes on a copper foil by catalytic chemical vapor deposition from ethanol. Carbon **50**, 2504–2512 (2012)
35. M. Lin, J.P.Y. Tan, C. Boothroyd, K.P. Loh, E.S. Tok, Y.L. Foo, Dynamical observation of bamboo-like carbon nanotube growth. Nano Lett. **7**, 2234–2238 (2007)
36. A. Gohier, C.P. Ewels, T.M. Minea, M.A. Djouadi, Carbon nanotube growth mechanism switches from tip- to base-growth with decreasing catalyst particle size. Carbon **46**, 1331–1338 (2008)
37. J. Liu, C.K. Poh, D. Zhan, L. Lai, S.H. Lim, L. Wang, X. Liu, N. Gopal Sahoo, C. Li, Z. Shen, J. Lin, Improved synthesis of graphene flakes from the multiple electrochemical exfoliation of graphite rod. Nano Energy **2**, 377–386 (2013)
38. B. Wu, D. Geng, Z. Xu, Y. Guo, L. Huang, Y. Xue, J. Chen, G. Yu, Y. Liu, Self-organized graphene crystal patterns. NPG Asia Mater. **5**, e36 (2013)
39. T. Gao, H. Fjellvåg, P. Norby, A comparison study on Raman scattering properties of α- and β-MnO_2. Anal. Chim. Acta **648**, 235–239 (2009)
40. C.H. Xu, J. Sun, L. Gao, Synthesis of novel hierarchical graphene/polypyrrole nanosheet composites and their superior electrochemical performance. J. Mater. Chem. **21**, 11253–11258 (2011)
41. Y. Zhao, J. Liu, Y. Hu, H. Cheng, C. Hu, C. Jiang, L. Jiang, A. Cao, L. Qu, Highly compression-tolerant supercapacitor based on polypyrrole-mediated graphene foam electrodes. Adv. Mater. **25**, 591–595 (2013)
42. L.B. Hu, W. Chen, X. Xie, N.A. Liu, Y. Yang, H. Wu, Y. Yao, M. Pasta, H.N. Alshareef, Y. Cui, Symmetrical MnO_2-carbon nanotube-textile nanostructures for wearable pseudocapacitors with high mass loading. ACS Nano **5**, 8904–8913 (2011)
43. M.V. Reddy, T. Yu, C.H. Sow, Z.X. Shen, C.T. Lim, G.V.S. Rao, B.V.R. Chowdari, α-Fe_2O_3 nanoflakes as an anode material for Li-ion batteries. Adv. Funct. Mater. **17**, 2792–2799 (2007)
44. A. Parthasarathy, B. Davé, S. Srinivasan, A.J. Appleby, C.R. Martin, The platinum microelectrode/Nafion interface: an electrochemical impedance spectroscopic analysis of oxygen reduction kinetics and Nafion characteristics. J. Electrochem. Soc. **139**, 1634–1641 (1992)
45. Y.M. He, W.J. Chen, X.D. Li, Z.X. Zhang, J.C. Fu, C.H. Zhao, E.Q. Xie, Freestanding three-dimensional graphene/MnO_2 composite networks as ultra light and flexible supercapacitor electrodes. ACS Nano **7**, 174–182 (2013)

46. R. Liu, J. Duay, S.B. Lee, Electrochemical formation mechanism for the controlled synthesis of heterogeneous MnO_2/Poly(3,4-ethylenedioxythiophene) nanowires. ACS Nano **5**, 5608–5619 (2011)
47. X. Lu, M. Yu, G. Wang, T. Zhai, S. Xie, Y. Ling, Y. Tong, Y. Li, H-TiO_2@MnO_2// H-TiO_2@C core-shell nanowires for high performance and flexible asymmetric supercapacitors. Adv. Mater. **25**, 267–272 (2013)
48. J. Yan, E. Khoo, A. Sumboja, P.S. Lee, Facile coating of manganese oxide on tin oxide nanowires with high-performance capacitive behavior. ACS Nano **4**, 4247–4255 (2010)
49. S. Dong, X. Chen, L. Gu, X. Zhou, L. Li, Z. Liu, P. Han, H. Xu, J. Yao, H. Wang, X. Zhang, C. Shang, G. Cui, L. Chen, One dimensional MnO_2/titanium nitride nanotube coaxial arrays for high performance electrochemical capacitive energy storage. Energy Environ. Sci. **4**, 3502–3508 (2011)
50. X. Lu, T. Zhai, X. Zhang, Y. Shen, L. Yuan, B. Hu, L. Gong, J. Chen, Y. Gao, J. Zhou, Y. Tong, Z.L. Wang, WO_{3-x}@Au@MnO_2 core-shell nanowires on carbon fabric for high-performance flexible supercapacitors. Adv. Mater. **24**, 938–944 (2012)
51. P. Yang, X. Xiao, Y. Li, Y. Ding, P. Qiang, X. Tan, W. Mai, Z. Lin, W. Wu, T. Li, H. Jin, P. Liu, J. Zhou, C.P. Wong, Z.L. Wang, Hydrogenated ZnO core-shell nanocables for flexible supercapacitors and self-powered systems. ACS Nano **7**, 2617–2626 (2013)
52. M. Stadermann, S.J. Papadakis, M.R. Falvo, J. Novak, E. Snow, Q. Fu, J. Liu, Y. Fridman, J. J. Boland, R. Superfine, S. Washburn, Nanoscale study of conduction through carbon nanotube networks. Phys. Rev. B **69** (2004)
53. J.L. Liu, J. Sun, L.A. Gao, A promising way to enhance the electrochemical behavior of flexible single-walled carbon nanotube/polyaniline composite films. J. Phys. Chem. C **114**, 19614–19620 (2010)
54. J.P. Zheng, The limitations of energy density of battery/double-layer capacitor asymmetric cells. J. Electrochem. Soc. **150**, A484–A492 (2003)
55. T. Cottineau, M. Toupin, T. Delahaye, T. Brousse, D. Belanger, Nanostructured transition metal oxides for aqueous hybrid electrochemical supercapacitors. Appl. Phys. A Mater. Sci. Process **82**, 599–606 (2006)
56. L.B. Kong, M. Liu, J.W. Lang, Y.C. Luo, L. Kang, Asymmetric supercapacitor based on loose-packed cobalt hydroxide nanoflake materials and activated carbon. J. Electrochem. Soc. **156**, A1000–A1004 (2009)
57. T. Brousse, M. Toupin, D. Belanger, A hybrid activated carbon-manganese dioxide capacitor using a mild aqueous electrolyte. J. Electrochem. Soc. **151**, A614–A622 (2004)
58. Z. Lei, J. Zhang, X.S. Zhao, Ultrathin MnO2 nanofibers grown on graphitic carbon spheres as high-performance asymmetric supercapacitor electrodes. J. Mater. Chem. **22**, 153–160 (2012)
59. L.J. Deng, G. Zhu, J.F. Wang, L.P. Kang, Z.H. Liu, Z.P. Yang, Z.L. Wang, Graphene-MnO_2 and graphene asymmetrical electrochemical capacitor with a high energy density in aqueous electrolyte. J. Power Sources **196**, 10782–10787 (2011)
60. J. Duay, E. Gillette, R. Liu, S.B. Lee, Highly flexible pseudocapacitor based on freestanding heterogeneous MnO_2/conductive polymer nanowire arrays. Phys. Chem. Chem. Phys. **14**, 3329–3337 (2012)
61. Z.-S. Wu, W. Ren, D.-W. Wang, F. Li, B. Liu, H.-M. Cheng, High-Energy MnO_2 nanowire/graphene and graphene asymmetric electrochemical capacitors. ACS Nano **4**, 5835–5842 (2010)
62. Q.T. Qu, Y. Shi, S. Tian, Y.H. Chen, Y.P. Wu, R. Holze, A new cheap asymmetric aqueous supercapacitor: activated carbon//$NaMnO_2$. J. Power Sources **194**, 1222–1225 (2009)
63. M. Huang, Y. Zhang, F. Li, L. Zhang, R.S. Ruoff, Z. Wen, Q. Liu, Self-assembly of mesoporous nanotubes assembled from interwoven ultrathin birnessite-type MnO_2 nanosheets for asymmetric supercapacitors. Sci. Rep. **4** (2014)
64. J. Ji, L.L. Zhang, H. Ji, Y. Li, X. Zhao, X. Bai, X. Fan, F. Zhang, R.S. Ruoff, Nanoporous Ni (OH) thin film on 3D ultrathin-graphite foam for asymmetric supercapacitor. ACS Nano **7**, 6237–6243 (2013)

65. K.C. Ng, S. Zhang, G.Z. Chen, An asymmetrical supercapacitor based on CNTs/SnO_2 and CNTs/MnO_2 nanocomposites working at 1.7 V in aqueous electrolyte. ECS Trans. **16**, 153–162 (2008)
66. H. Jiang, C.Z. Li, T. Sun, J. Ma, A green and high energy density asymmetric supercapacitor based on ultrathin MnO_2 nanostructures and functional mesoporous carbon nanotube electrodes. Nanoscale **4**, 807–812 (2012)
67. T. Brousse, P.-L. Taberna, O. Crosnier, R. Dugas, P. Guillemet, Y. Scudeller, Y. Zhou, F. Favier, D. Belanger, P. Simon, Long-term cycling behavior of asymmetric activated carbon/MnO_2 aqueous electrochemical supercapacitor. J. Power Sources **173**, 633–641 (2007)

Chapter 5
Graphene Foam/Carbon Nanotubes Hybrid Film Based Flexible Alkaline Rechargeable Ni/Fe Battery

The proliferation of wearable and portable electronics requires high-performance power sources that are lightweight, ultrathin, flexible and low cost in addition to high performance features. Here, a new type of flexible Ni/Fe cell is designed and fabricated by employing $Ni(OH)_2$ nanosheets and porous Fe_2O_3 nanorods grown on lightweight and flexible graphene foam (GF)/carbon nanotubes (CNTs) hybrid films as electrodes. The assembled f-Ni/Fe cells are able to deliver high energy/power densities (100.7 Wh/kg at 287 W/kg and 70.9 Wh/kg at 1.4 kW/kg) and outstanding cycling stability (retention 89.1% after 1000 charge/discharge cycles). Benefiting from the use of ultra-light and thin GF/CNTs hybrid films as current collectors, the f-Ni/Fe cell can exhibit a volumetric energy density of 16.6 Wh/l (based on the total volume of full cell). This value is comparable to that of thin film battery and better than that of typical commercial supercapacitors. Moreover, the f-Ni/Fe cells can retain the electrochemical performance with repeated bendings. These features endow f-Ni/Fe cells highly promising candidates for next generation flexible energy storage systems.

5.1 Introduction

The sharp proliferation of portable electronics and electrical vehicles requires high-performance power sources that process high energy density and power density and with lightweight, ultrathin, flexible, cost-effective and environmental friendly characteristics [1–3]. Among various energy storage devices, aqueous rechargeable batteries have attracted much attentions because of high ionic conductivity, environmental issues, good safety and low cost [4–7]. Many types of aqueous rechargeable batteries including aqueous alkali-ion (Li^+, Na^+, K^+) batteries [8, 9], aqueous metal-ion batteries (Al^{3+}, Zn^{2+}) [10, 11] and aqueous nickel/metal (zinc, cadmium, cobalt and iron) batteries, have been explored [5, 6, 12, 13]. Different from the reversible intercalation/de-intercalation chemistry for aqueous alkali-ion

J. Liu, *Graphene-Based Composites for Electrochemical Energy Storage*,
Springer Theses, DOI 10.1007/978-981-10-3388-9_5

batteries and metal-ion batteries, the nickel/metal battery are mainly based on Faradaic reactions that involve one or multi-electron reactions on electrode materials [5]. Numerous electrochemical redox couples have been explored for alkaline rechargeable nickel/metal batteries, such as nickel/cadmium [6, 7], nickel/zinc [14], nickel/cobalt [5] and nickel/iron [12, 13]. Among these, aqueous Ni/Fe batteries are particularly favorable because (i) both Ni and Fe active materials are insoluble in alkaline solution, and has no requirement for the separator (in contrast with Ni/Zn and Ag/Zn batteries) [15, 16]; (ii) both Ni and Fe are earth-abundant elements and exhibit low toxic or corrosive effect [13, 15, 16]. Nickel-iron battery, which was invented in 1899–1902, has been well developed [15, 16]. More recently, the century-old nickel-iron battery was revisited and re-discovered to explore its potential application for modern energy supply systems. In contrast with traditional Ni/Fe batteries, hybrid materials based on novel inorganic nanoparticles (or rods) and carbon allotropes (carbon fibers [12], carbon nanotubes and graphene [13]) are now used as electrode materials, which indeed have improved the rate performance and energy density of Ni/Fe cells. Nevertheless, in the recent demonstrated high-performance Ni/Fe batteries [13], the active materials are in powder form and carbon black and binders are still required. These additives, together with the heavy Ni foam current collector, will lower the gravimetric specific capacity of the full cells. To push the performance particularly in flexible electronic devices, it is highly desirable to design novel electrode architecture that is binder-free, bendable and durable in long-term cycling.

In Chap. 4, graphene foam/carbon nanotubes (GF/CNTs) hybrid films were prepared and demonstrated to be excellent electrode supports due to their highly conductive, and large surface-to-volume ratio features [17]. They are ideal for depositing nanometer sized active materials without binders or carbon additives towards flexible and high-performance power sources. Herein, aqueous rechargeable Ni/Fe batteries are constructed by direct growth of $Ni(OH)_2$ nanosheets (cathode material) and mesoporous Fe_2O_3 nanroods (anode material) on the GF/CNTs hybrid films. These novel flexible Ni/Fe cells deliver superior energy and power densities stemming from the nanosized feature of active materials and the hierarchical structure of the electrodes. Stable capacities on repeated bending and long-term (up to 1000) cycling are also demonstrated.

5.2 Experiment

5.2.1 Materials Synthesis

Synthesis of Graphene Foam (GF)/Carbon nanotubes (CNTs) hybrid film. The GF/CNTs hybrid films were synthesized via a modified recipe [18].

Synthesis of GF/CNTs/Ni(OH)$_2$ hybrid film. $Ni(OH)_2$ nanosheets were electrochemical deposited on GF/CNTs hybrid film directly in 0.1 M $Ni(NO_3)_2$ aqueous

solution at a sweep rate of 100 mV/s with working windows at −1.2–0 V (*vs*. SCE). The mass loading of $Ni(OH)_2$ was controlled via adjusting the number of cyclic voltammmetry from 50 to 200. The samples are denoted as GF/CNTs/$Ni(OH)_2$-n, where n is the areal mass density of $Ni(OH)_2$ (unit of mg/cm^2).

Synthesis of GF/CNTs/Fe_2O_3 hybrid film. A simple hydrothermal method is used for the synthesis of GF/CNTs/Fe_2O_3 hybrid film. Briefly, a piece of GF/CNTs film was immersed into a mixture solution of $Fe(NO_3)_3{\cdot}9H_2O$ (Merck AR, >99.0%) (monomer amount at 1.5, 3 and 6 mM), DI water (50 mL) and 15 mmol urea (AR, >99.0%), followed by the addition of 5 mL of 30% HCl. The mixture was then transferred into a Teflon-lined autoclave and heated at 150 °C for 15 h. The as-prepared precursor was washed with DI water and annealed at 550 °C for 1.5 h in Ar to obtain GF/CNTs/Fe_2O_3 hybrid films. The samples are denoted as GF/CNTs/Fe_2O_3-n, where n is mass loading amount of Fe_2O_3 (mg/cm^2).

Assemble of GF/CNTs/$Ni(OH)_2$-GF/CNTs/Fe_2O_3 rechargeable batteries (F-Ni/Fe batteries). Flexible Ni/Fe batteries with high performance were assembled using a piece of GF/CNTs/$Ni(OH)_2$ (1 × 4 cm^2) and a piece of GF/CNTs/Fe_2O_3 (1 × 4 cm^2), with an electrolyte-soaked (6 M KOH) separator in between.

5.2.2 Materials Characterization

Structure and Morphology Characterization. Field-emission Scanning Electron Microscopy (FESEM, JEM-6700F, 10.0 kV), Transmission Electron Mmicroscopy (TEM, JEM-2010, 200 kV), X-ray diffraction (XRD, Bruker D-8 Avance), X-ray photoelectron spectroscopy (XPS) on a VG ESCALAB 250 spectrometer (Thermo Electron, Altrincham, UK) [Al Kα X-ray source (1486 eV)] and the N_2 adsorption/desorption [ASAP2020 volumetric adsorption analyzer (Micromeritics, USA) were used to characterize the samples.

Electrochemical Performance Evaluation. Cyclic voltammetry (CV) curves, Galvanostatic charge/discharge curves and electrochemical impedance spectroscopy (EIS, 100 kHz–0.01 Hz) were collected using CHI 760D workstation. The three-electrode system is chosen for individual electrode testing.

Calculations. The specific capacity (C*, mAh/g) of positive or negative electrode in **three-electrode** configuration are calculated according to the equation:

$$C^* = \frac{I}{m}\Delta t$$

where I is the discharging current, m is the mass of the individual electrodes, Δt is the discharge time.

The specific capacity (C*, mAh/g) of f-Ni/Fe cells in **two-electrode** configuration are calculated according to the equation:

$$C^* = \frac{I}{M}\Delta t$$

where I is the discharging current, M is the total mass of the two electrodes, Δt is the discharge time.

The equation: $C_- V_- = C_+ V_+$, is used for the charge match between two electrodes. The energy density (E) and power density (P) are calculated according to the equations below:

$$E = \int IV\, dt/dm$$

$$P = E/\Delta t$$

5.3 Results and Discussions

5.3.1 The Synthesis of GF/CNTs/$Ni(OH)_2$ and GF/CNTs/Fe_2O_3

In situ electrochemical deposition method was employed for the synthesis of GF/CNTs/$Ni(OH)_2$ hybrid electrodes. This method is advantageous due to: (i) it can produces thin nanosheet structure of $Ni(OH)_2$ active material; and (ii) it also allows a fine tuning of mass loading of $Ni(OH)_2$ via modulating the concentrations of electrolyte and deposition time (Fig. 5.1) [19, 20]. The flower-like $Ni(OH)_2$ nano-sheets surround the CNTs uniformly with outer diameters ranging from 150 to 300 nm (depending on the mass loading amount) (Fig. 5.2a). The mass loading

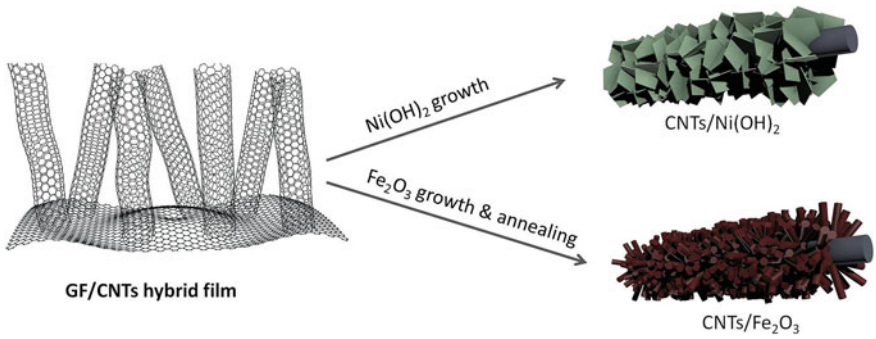

Fig. 5.1 Schematic illustration of the synthesis of GF/CNTs-based electrodes. Figure reproduced from Ref. [41]

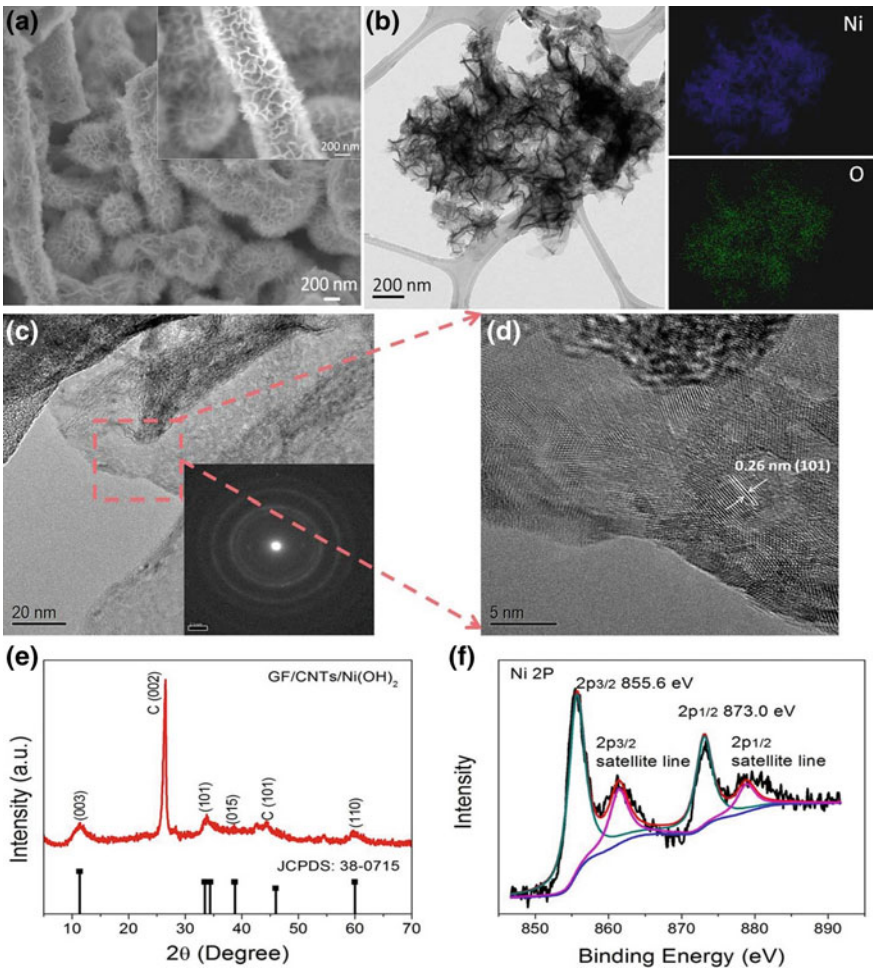

Fig. 5.2 Characterization of the GF/CNTs/$Ni(OH)_2$ hybrid film. **a** Typical FESEM image (inset is magnified SEM image) and **b** Low-magnification TEM image of the hybrid film and corresponding element mappings of Ni and O. **c** TEM image (inset is selected area electron diffraction (SAED) pattern) and correspond HRTEM image (**d**). **e** XRD pattern and **f** XPS spectra

density of $Ni(OH)_2$ is adjustable and well-controlled. More details about the nano-sheet feature of $Ni(OH)_2$ can be found in TEM images (Fig. 5.2b, c). The element mapping images verify the uniform distribution of O and Ni (Fig. 5.2b). The well-defined SAED pattern (inset in Fig. 5.2c) corroborates that the $Ni(OH)_2$ nano-sheets are polycrystalline. Well-resolved lattice fringes of 0.26 nm was observed (Fig. 5.2d), corresponding to the (101) plane of α-$Ni(OH)_2$ (JCPDS #38-0715). X-ray diffraction (XRD) results further confirm the formation of rhombohedral α-$Ni(OH)_2$. All the peaks could be indexed to rhombohedral α-Ni $(OH)_2$ except the crystalline peaks at 26.4° and 44.3° that result from GF/CNTs

substrate (Fig. 5.2e). X-ray photoelectron spectroscopy (XPS) analysis was conducted to shed more light on composition and oxidization stage of $Ni(OH)_2$. Two typical peaks centered at 855.6 and 873.0 eV were observed (Fig. 5.2f), corresponding to Ni $2p_{3/2}$ and Ni $2p_{1/2}$ of $Ni(OH)_2$, respectively [21]. Meanwhile, two satellite lines associated with Ni 2p are also identified.

GF/CNTs/Fe_2O_3 hybrid electrodes were prepared via a facile hydrothermal reaction of FeOOH nanorods followed by thermal annealing (Fig. 5.1). Representative SEM images (Fig. 5.3a) reveal the well-defined interconnected network structure of GF/CNTs/Fe_2O_3, in which the columnar Fe_2O_3 nanorods coated around CNTs uniformly with outer diameter ranging from 200 to 300 nm.

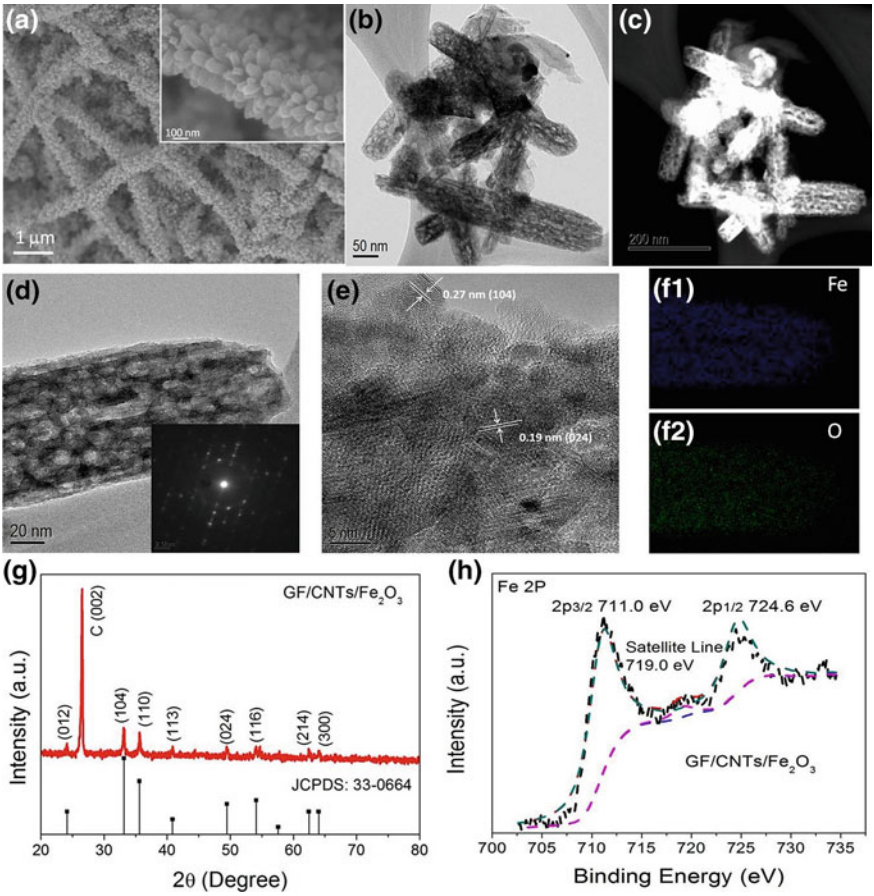

Fig. 5.3 Characterization of the GF/CNTs/Fe_2O_3 hybrid film. **a** Typical FESEM image (inset is magnified SEM image) and **b** Low-magnification bright-field TEM image and **c** *dark field* TEM image of the hybrid film. **d** TEM image (inset is selected area electron diffraction (SAED) pattern), corresponding HRTEM image (**e**), and **f1**–**f2** corresponding element mappings of Fe and O. **g** XRD pattern and **h** XPS spectrum

TEM images (Fig. 5.3b, c) clearly identify the mesoporous nanorod structure of Fe_2O_3 with diameter in the range of 50–150 nm and length ranging from 50 to 500 nm. This feature was further verified by the magnified TEM image in Fig. 5.3d, where the pore size is around 5–10 nm. The specific surface area of the GF/CNTs/Fe_2O_3 hybrid film is around 68 m^2/g. This value is comparable with rGO/Fe_2O_3 composites [22] and higher than that of mesoporous Fe_2O_3 [23]. The good crystallinity nature of Fe_2O_3 nanorods is manifested by the clear SAED pattern (inset of Fig. 5.3d). The well-defined lattice fringes with distances of 0.19 and 0.27 nm (Figs. 5.3e) correspond to the d-spacing of (024) and (104) planes, respectively. The homogeneous distribution of both Fe and O corroborates the uniform coating of Fe_2O_3 (Fig. 5.3f1, f2). The characteristic peaks in XRD can be well indexed as tetragonal α-Fe_2O_3 (JCPDS 33-0664) [24]. XPS result (Fig. 5.3h) exhibits typical Fe 2p spectrum of Fe_2O_3 with two peaks centered at 711.0 and 724.6 eV, corresponding to Fe $2p_{3/2}$ and Fe $2p_{1/2}$, respectively [25]. The presence of satellite line of the main Fe $2p_{3/2}$ located at 719.0 eV further verifies the Fe_2O_3 phase rather than Fe_3O_4.

5.3.2 *Electrochemical Performance of GF/CNTs/Ni(OH)$_2$ and GF/CNTs/Fe$_2$O$_3$*

The electrochemical properties of both GF/CNTs/$Ni(OH)_2$ cathode and GF/CNTs/Fe_2O_3 anode were investigated in a three-electrode configuration containing 6 M KOH solution. Hereby, our discussion start with the charge-matching electrodes, viz., GF/CNTs/$Ni(OH)_2$-0.9 cathode and GF/CNTs/Fe_2O_3-0.6 anode (0.9 and 0.6 denote the areal mass densities of the corresponding active materials in unit of mg/cm^2). Typical cyclic voltammetry (CV) curves of GF/CNTs/$Ni(OH)_2$-0.9 and GF/CNTs/Fe_2O_3-0.6 are shown in Figs. 5.4a, b. Well-defined redox peaks locating at 0.36 (anodic)/0.21 V(cathodic) (*vs.* SCE) are identified in typical cyclic voltammetry (CV) curves of GF/CNTs/$Ni(OH)_2$-0.9 (Fig. 5.4a). This corresponds to the reversible reaction as follows [7, 12, 26]:

$$Ni(OH)_2 + OH^- \leftrightarrow NiOOH + H_2O + e^- \left(E^0 = 0.249\,V\ vs.\ SCE\right). \tag{5.1}$$

Two oxidization peaks around −0.89 and −0.71 V in the anodic scan are observed for the GF/CNTs/Fe_2O_3 electrode (Fig. 5.4b). They are attributed to the formation of $Fe(OH)_2$ (with the oxidization from Fe^0 to Fe^{2+}) and FeOOH (with the oxidization from Fe^{2+} to Fe^{3+}), respectively. One well-defined reduction peak at around 1.05 V is found in the cathodic curve, which is assigned to the reduction from Fe^{3+} to Fe^{2+}. Another cathodic peak (corresponding to the reduction of Fe^{2+} to Fe^0) is missed, probably due to the distortion caused by the H_2 evolution.

The redox peaks are found to be sweep rate dependent with the peak position separation, $\Delta E_{a,c}$, increases with increasing sweep rate [27, 28]. The increase in the

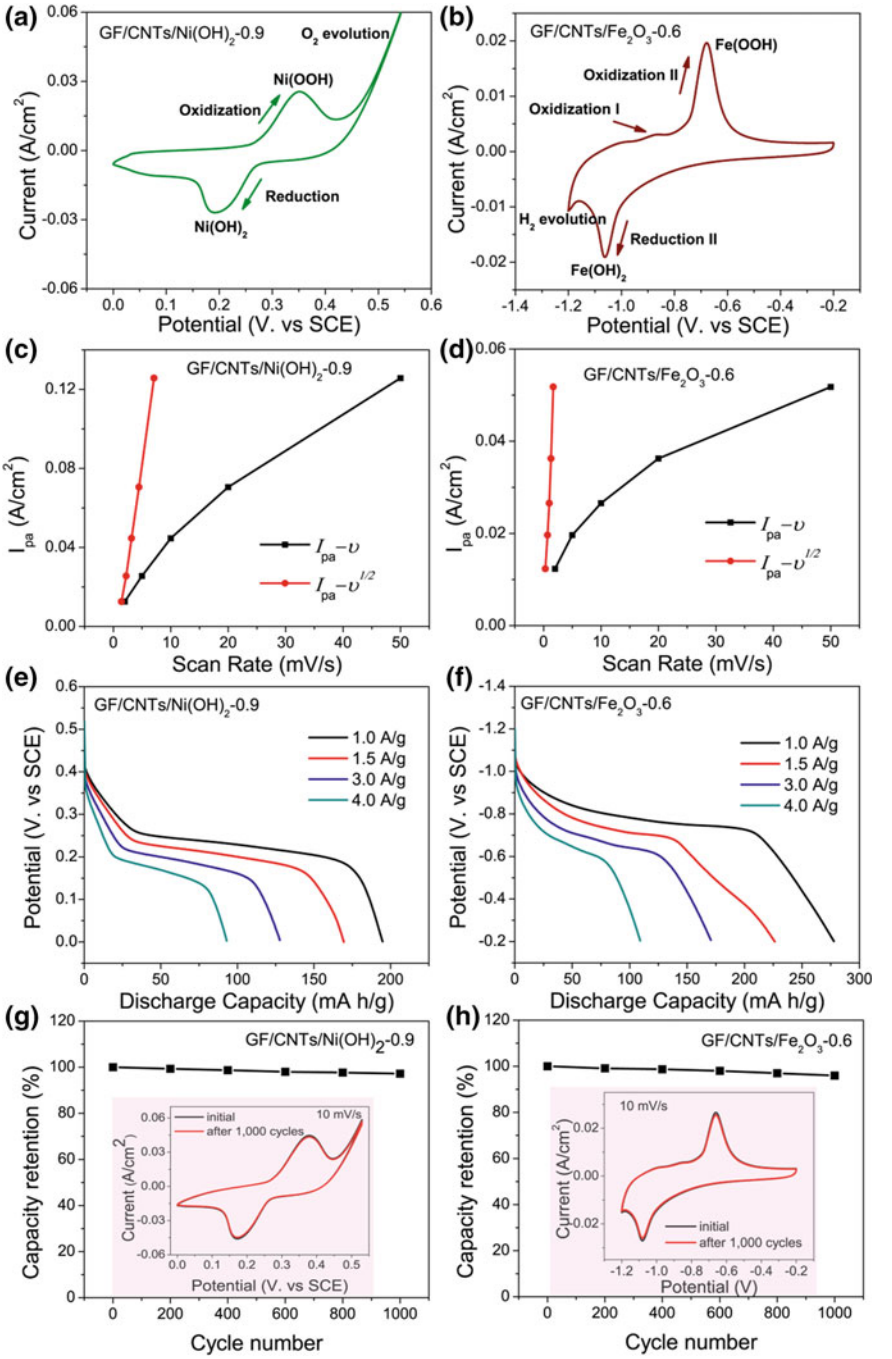
(a)
GF/CNTs/Ni(OH)2-0.9
O2 evolution
Ni(OOH)
Oxidization
Reduction
Ni(OH)2
Current (A/cm2)
Potential (V. vs SCE)
(b)
GF/CNTs/Fe2O3-0.6
Fe(OOH)
Oxidization II
Oxidization I
H2 evolution
Reduction II
Fe(OH)2
Current (A/cm2)
Potential (V. vs SCE)
(c)
GF/CNTs/Ni(OH)2-0.9
Ipa (A/cm2)
Ipa−υ
Ipa−υ1/2
Scan Rate (mV/s)
(d)
GF/CNTs/Fe2O3-0.6
Ipa (A/cm2)
Ipa−υ
Ipa−υ1/2
Scan Rate (mV/s)
(e)
GF/CNTs/Ni(OH)2-0.9
1.0 A/g
1.5 A/g
3.0 A/g
4.0 A/g
Potential (V. vs SCE)
Discharge Capacity (mA h/g)
(f)
GF/CNTs/Fe2O3-0.6
1.0 A/g
1.5 A/g
3.0 A/g
4.0 A/g
Potential (V. vs SCE)
Discharge Capacity (mA h/g)
(g)
GF/CNTs/Ni(OH)2-0.9
initial
after 1,000 cycles
10 mV/s
Current (A/cm2)
Potential (V. vs SCE)
Capacity retention (%)
Cycle number
(h)
GF/CNTs/Fe2O3-0.6
10 mV/s
initial
after 1,000 cycles
Current (A/cm2)
Potential (V)
Capacity retention (%)
Cycle number

◂**Fig. 5.4** Electrochemical characterizations of the hybrid film electrodes. *Left column* GF/CNTs/Ni $(OH)_2$-0.9 cathode. *Right column* GF/CNTs/Fe_2O_3-0.6 anode. **a**, **b** Cyclic voltammetry curves at a sweep rate of 5 mV/s. **c**, **d** Variation of anodic peak current (I_{pa}) with sweep rate. **e**, **f** Galvanostatic discharge curves at various current densities. **g**, **h** Cycling performance. Insets are the corresponding CV curves after 1000 cycles. Figure reproduced from Ref. [41]

charge diffusion polarization within the pseudoactive material upon the increase of sweep rate accounts for this [29]. The peak current (I_{pa}) is plotted as a function of sweep rate (υ) and $\upsilon^{1/2}$ to gain insight into the kinetic information of the involved redox reactions (Figs. 5.4c, d). The linear I_{pa} versus $\upsilon^{1/2}$ plots have been derived. On the other hand, the I_{pa} versus υ plots display a non-linear behavior. Generally, I_{pa} versus $\upsilon^{1/2}$ plot shows linear relationship regardless of the sweep rate for a kinetically uncomplicated redox reaction in semi-infinite diffusion controlled CV, and the I_{pa} versus υ plots is expected to be linear for an adsorption process [30–35]. Therefore, the oxidization processes involved here are diffusion limited, agreeing well with previous reported results about $LiFePO_4$ [33].

Figures 5.4e, f illustrate the typical discharge curves of $Ni(OH)_2$ electrode and Fe_2O_3, respectively, upon various discharge current densities. A well-defined plateau at around 0.25 V was observed for $Ni(OH)_2$ electrode, consisting well with Eq. (5.1). The oxidization reactions of iron anode in alkaline electrolytes could be described as [7, 15, 36–39]:

$$\mathrm{Fe} + 2\mathrm{OH}^- \leftrightarrow \mathrm{Fe(OH)_2} + 2e^- \left(\mathrm{E}^0 = -1.076\,\mathrm{V}\ vs.\ \mathrm{SCE}\right) \tag{5.2}$$

$$3\mathrm{Fe(OH)_2} + 2\mathrm{OH}^- \leftrightarrow \mathrm{Fe_3O_4} + 4\mathrm{H_2O} + 2\mathrm{e}^- \left(\mathrm{E}^0 = -0.859\,\mathrm{V}\ vs.\ \mathrm{SCE}\right) \tag{5.3}$$

or/and

$$\mathrm{Fe(OH)_2} + \mathrm{OH}^- \leftrightarrow \mathrm{FeOOH} + \mathrm{H_2O} + e^- \left(\mathrm{E}^0 = -0.756\,\mathrm{V}\ vs.\ \mathrm{SCE}\right) \tag{5.4}$$

The well-defined plateau around −0.77 V (*vs.* SCE) can be assigned to the reaction (5.4). The plateau corresponding to reaction (5.2) is not evident in either CV or discharge curves, which suggests that the anodic process is dominated by reaction (5.4). Possibly reaction (5.2) takes place synchronously with the hydrogen evolution during the cathodic scan when the H_2 evolution occurs at a more positive potential.

The gravimetric capacitance of GF/CNTs/$Ni(OH)_2$ electrode (Fig. 5.4e) and GF/CNTs/Fe_2O_3 electrode (Fig. 5.4f) were calculated from the corresponding galvanostatic discharge curves. The GF/CNTs/$Ni(OH)_2$-0.9 and GF/CNTs/Fe_2O_3-0.6 deliver a gravimetric capacity of 195 and 278 mAh/g, respectively, at 1 A/g. The gravimetric capacities retain at 93 and 109 mAh/g, respectively, even at a high sweep rate of 4 A/g. These results imply good rate capabilities for both hybrid electrodes. Moreover, good cycle stability with capacity retention at 97.2% for GF/CNTs/$Ni(OH)_2$-0.9 (Fig. 5.4g) and 96% for GF/CNTs/Fe_2O_3-0.6 (Fig. 5.4h) after 1000 cycles have been demonstrated.

The electrochemical performance of hybrid electrodes is strongly affected by mass loading of active materials. Specifically, the gravimetric capacity and rate performance degrade with the increase in active materials loading, although the corresponding current response increases. The decrease in electric conductivity related to the increase in the active materials coating thickness takes responsibility for this. For example, the equivalent series resistance (ESR) increases from 2.9 Ω for GF/CNTs/$Ni(OH)_2$-0.5 to 4.6 Ω for GF/CNTs/$Ni(OH)_2$-1.2. Similar trend was also noted for GF/CNTs/Fe_2O_3 electrodes with different mass loading. The dependence of electrochemical property on mass loading of active materials demonstrates the importance of electrode design to achieve optimized performance of full cells.

5.3.3 *Electrochemical Performance of F-Ni/Fe Battery*

Based on the results above, Ni/Fe full cells were fabricated by using GF/CNTs/Ni$(OH)_2$-0.9 hybrid film as cathode and GF/CNTs/Fe_2O_3-0.6 as anode. These two electrodes were chosen because a good charge match has been achieved. The sweep rate dependent CV curves of the f-Ni/Fe are illustrated in Fig. 5.5a. Well-defined redox couples were observed, originating from the overall reaction in the Ni/Fe cell [12],

$$Ni(OH)_2 + 1/6Fe_2O_3 \leftrightarrow NiOOH + 1/3Fe + 1/2H_2O. \tag{5.5}$$

Similar to the individual electrode, the f-Ni/Fe cell exhibits an increase in the anodic peak and cathodic peak separation ($\Delta E_{a,c}$) with increasing sweep rate. The I_{pa} versus $\upsilon^{1/2}$ plot of f-Ni/Fe cell is also linear, indicating that a diffusion limited oxidization reaction takes place during the charging process [30–33]. The f-Ni/Fe cell delivers high specific capacity of 119 mAh/g at sweep rate of 5 mV/s and 78 mAh/g at sweep rate of 40 mV/s (Fig. 5.5b), implying its good rate capability. Typical galvanostatic discharge curves at different current densities are shown in Fig. 5.5c. Consistent to the CV curves, the discharge profiles exhibit good reversibility with distinct discharge voltage plateau from 0.9 to 1.1 V (depending on current density), demonstrating its application feasibility for energy storage [12, 13, 38]. The specific capacity decreases from 118 to 50 mAh/g when the current density increase from 0.3 to 8 A/g. The discharge process (Fig. 5.5c) completes in short times ranging from 20 min to 30 s, depending on the current density. These discharge time are much shorter than conventional Ni/Fe batteries that usually require hours. These values also outperform the Ni/Fe cell based on carbon fibers [12] with a specific capacity of 80 mAh/g and charge/discharge time of hours. The series resistance of the device is estimated to be 5.9 Ω (R_s = 3.8 Ω; R_{ct} = 2.1 Ω) from the EIS data. The relatively small serial resistances of the f-Ni/Fe cell ensure a fast charge transfer between the electrolyte and electrodes.

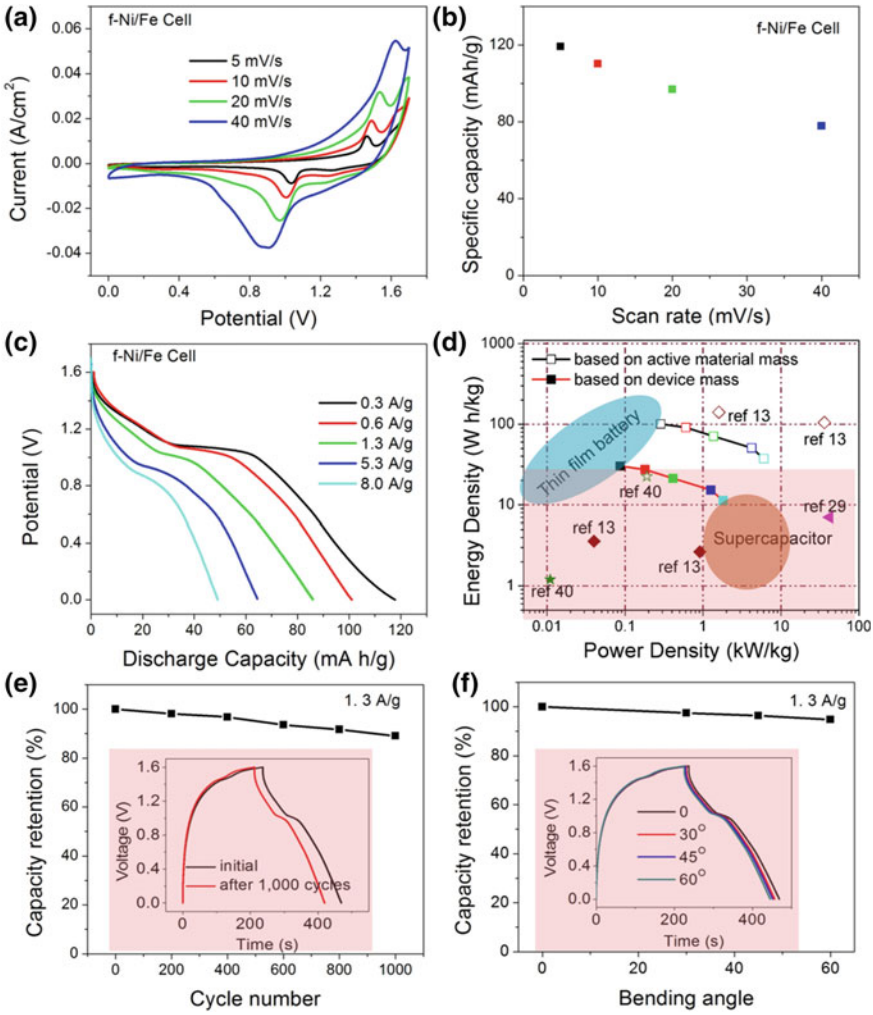

Fig. 5.5 Performance of the flexible Ni/Fe full cells. Cyclic Voltammetry curves (**a**) and corresponding gravimetric capacity (**b**) at different sweep rates. **c** Galvanostatic discharge curves at various current densities and **d** The Ragone plot. Comparisons are made in two ways: based on the active material mass only (*upper half*), and based on the whole device mass (*bottom shaded half*). **e** Cycling performance of the f-Ni/Fe cell at a current density of 1.3 A/g for 1000 cycles. Inset shows the charge/discharge curves for the 1st and 1000th cycles. **f** Cycling performance of f-Ni/Fe cell at different bending angles. Inset shows the charge/discharge curves at different bending angles. Figure reproduced from Ref. [41]

The Ragone plots, showing energy density and power density, are plotted in two ways, viz., one based on the active material mass only (open symbols); and the other based on the whole device mass (solid symbols) (Fig. 5.5d). The f-Ni/Fe cell delivers an energy density of 100.7 Wh/kg at 287 W/kg and 70.9 Wh/kg at

1.4 kW/kg, respectively, based on the total mass of active materials. Even at a high power density of 6.0 kW/kg, an energy density of 37.4 Wh/kg can still be achieved. Considering the total mass of the cell, a gravimetric energy density of 30.3 Wh/kg is achieved, benefiting from the lightweight nature of GF/CNTs hybrid films current collector. This value is three folds that of typical commercial supercapacitors, and higher than that of Ni/Fe cells using nickel foams as the current collector [13]. The maximum power density of 1.8 kW/kg is comparable to that of commercial supercapacitor, and four-folds higher than that of lithium thin film battery.

In order to push the practical applications of the f-Ni/Fe cell, the volumetric energy/power densities based on the whole cell configuration were also calculated (Table 5.1). A maximum volumetric energy density of 16.6 Wh/l has been achieved, which is two-folds higher than the reported MnO_2-based [40] and Ni $(OH)_2$-based asymmetric supercapacitors [29], both are typical high-capacity supercapacitive materials. The maximum volumetric power density is 1.0 kW/l. Moreover, the f-Ni/Fe cell exhibits good cycling stability with capacity retention of 89.1% after 1000 charge/discharge cycles (Fig. 5.5e). This result is better than the recently reported Ni/Fe cells which showed 80% capacity retention after 800 cycles [13]. Moreover, the capacity could retain at 78% when the stability test extended further to 2000 cycles. And the CNTs-supported structures were well maintained although the surfaces of electrodes show some degree of aggregations during the long charge/discharge process.

The development of multifunctional flexible electronics requires power sources that are flexible and lightweight in addition to high performance. For practical

Table 5.1 Parameters for the flexible Ni/Fe cell (f-Ni/Fe Cell) and the calculated gravimetric and volumetric energy/power densities based on the fully packaged cell

		Thickness (μm)	Density (g/cm^3)	Weight percentage (%)	Volume percentage (%)
Ni/Fe cell	Positive electrode (GF/CNTs/Ni $(OH)_2$-0.9)	31	0.50	31.1	34.5
	Negative electrode (GF/CNTs/Fe_2O_3-0.6)	30	0.42	25.1	33.3
	Separator	29	0.39	22.6	32.2
	Electrolyte (6 M KOH)	–	1.23	21.2	–
		E_{max} (Wh/kg)	P_{max} (kW/kg)	E_{max} (Wh/L)	P_{max} (kW/L)
Ni/Fe cell	Active materials ($Ni(OH)_2$ + Fe_2O_3)	100.7	6.0	–	–
	Electrodes (including GF/CNTs films)	53.9	3.2	24.7	1.5
	Full cell	30.3	1.8	16.6	1.0

Remarks The electrolyte is absorbed by the electrodes and thus does not take up any volume in the packaged cell. For f-Ni/Fe Cell: total cell mass is 20.0 mg; total volume is 36.4 μL; density of packaged cell is 0.55 g/cm^3

application consideration, the f-Ni/Fe cells were mechanically bended during the charge/discharge measurements (Fig. 5.5f). Negligible changes in the charge/discharge curves under different bending angles (up to 60°) were identified, corroborating the good flexible feature of the f-Ni/Fe cell. The practical application of our f-Ni/Fe cell was further demonstrated by driving a fan or light-emitting diodes (LEDs) using two f-Ni/Fe cells connected in series. Benefiting from the high power/energy density, the f-Ni/Fe cell could power one red LED (1.8 V, 20 mA, 5 mm diameter) and one yellow LED (1.8 V, 30 mA, 5 mm diameter) simultaneously after charging for only 30 s, or drive a small rotation motor (3 V, 0.45 W) after charging for only a few seconds.

5.3.4 Underlying Mechanism for Enhanced Electrochemical Performance

The high performance Ni/Fe cells demonstrated here bridge the gap between conventional thin film Li-ion batteries and supercapacitors for flexible electronics. The nanostructured active materials are grown directly surrounding the highly-conductive CNTs. This feature contributed the following advantages: (1) It assures a favorable electric contact and facilitates the electron transportation. (2) It promotes good mechanical integrity, accounting for the high cycling stability and flexibility. (3) The lightweight and highly porous features of the GF/CNTs substrate significantly increases the mass loading of active materials as compared to direct growth onto the GF or a planar metallic current collectors [41]. This also eliminates the additives (e.g., carbon black and binder). Benefiting from the unique hierarchical design, the gravimetric energy density and volumetric energy density of the f-Ni/Fe cells are comparable to thin film lithium ion battery and better than typical commercial supercapacitors.

5.4 Conclusion

In conclusion, flexible Ni/Fe cells are designed and fabricated successfully based on lightweight and flexible GF/CNTs current collectors without using any binders or carbon additives. The high volumetric energy/power densities, good cycling stability and flexibility of the f-Ni/Fe cell are clearly demonstrated. Such high-performance alkaline batteries could bridge the energy density gap between supercapacitor and thin film lithium ion battery, and be promising candidate for next generation flexible energy storage systems. The design we proposed is scalable for mass production and could be extended to the fabrication of other binder-free and flexible Ni/Metal alkaline batteries.

References

1. Y. Wang, Y. Xia, Recent progress in supercapacitors: from materials design to system construction. Adv. Mater. **25**, 5336–5342 (2013)
2. X. Yang, C. Cheng, Y. Wang, L. Qiu, D. Li, Liquid-mediated dense integration of graphene materials for compact capacitive energy storage. Science **341**, 534–537 (2013)
3. V.L. Pushparaj, M.M. Shaijumon, A. Kumar, S. Murugesan, L. Ci, R. Vajtai, R.J. Linhardt, O. Nalamasu, P.M. Ajayan, Flexible energy storage devices based on nanocomposite paper. Proc. Natl. Acad. Sci. U.S.A. **104**, 13574–13577 (2007)
4. X.P. Gao, H.X. Yang, Multi-electron reaction materials for high energy density batteries. Energy Environ. Sci. **3**, 174–189 (2010)
5. X.-P. Gao, S.-M. Yao, T.-Y. Yan, Z. Zhou, Alkaline rechargeable Ni/Co batteries: Cobalt hydroxides as negative electrode materials. Energy Environ. Sci. **2**, 502–505 (2009)
6. U. Kohler, C. Antonius, P. Bauerlein, Advances in alkaline batteries. J. Power Sources **127**, 45–52 (2004)
7. A.K. Shukla, S. Venugopalan, B. Hariprakash, Nickel-based rechargeable batteries. J. Power Sources **100**, 125–148 (2001)
8. M. Pasta, C.D. Wessells, R.A. Huggins, Y. Cui, A high-rate and long cycle life aqueous electrolyte battery for grid-scale energy storage. Nat. Commun. **3**, 1149 (2012)
9. L. Chen, Q.W. Gu, X.F. Zhou, S.X. Lee, Y.G. Xia, Z.P. Liu, New-concept batteries based on aqueous Li^+/Na^+ mixed-ion electrolytes. Sci. Rep. **3** (2013)
10. C. Xu, B. Li, H. Du, F. Kang, Energetic zinc ion chemistry: the rechargeable zinc ion battery. Angew. Chem. Int. Ed. **51**, 933–935 (2012)
11. S. Liu, J.J. Hu, N.F. Yan, G.L. Pan, G.R. Li, X.P. Gao, Aluminum storage behavior of anatase TiO_2 nanotube arrays in aqueous solution for aluminum ion batteries. Energy Environ. Sci. **5**, 9743–9746 (2012)
12. Z. Liu, S.W. Tay, X. Li, Rechargeable battery using a novel iron oxide nanorods anode and a nickel hydroxide cathode in an aqueous electrolyte. Chem. Commun. **47**, 12473–12475 (2011)
13. H. Wang, Y. Liang, M. Gong, Y. Li, W. Chang, T. Mefford, J. Zhou, J. Wang, T. Regier, F. Wei, H. Dai, An ultrafast nickel–iron battery from strongly coupled inorganic nanoparticle/nanocarbon hybrid materials. Nat. Commun. **3**, 917 (2012)
14. M. Gong, Y. Li, H. Zhang, B. Zhang, W. Zhou, J. Feng, H. Wang, Y. Liang, Z. Fan, J. Liu, H. Dai, Ultrafast high-capacity NiZn battery with NiAlCo-layered double hydroxide. Energy Environ. Sci. **7**, 2025–2032 (2014)
15. C. Chakkaravarthy, P. Periasamy, S. Jegannathan, K.I. Vasu, The nickel iron battery. J. Power Sources **35**, 21–35 (1991)
16. G. Halpert, Past developments and the future of nickel electrode cell technology. J. Power Sources **12**, 177–192 (1984)
17. J.L. Liu, L.L. Zhang, H.B. Wu, J.Y. Lin, Z.X. Shen, X.W. Lou, High-performance flexible asymmetric supercapacitors based on a new graphene foam/carbon nanotubes hybrid film. Energy Environ. Sci. (2014). doi:10.1039/c1034ee01475h
18. J. Liu, L. Zhang, H.B. Wu, J. Lin, Z. Shen, X.W. Lou, High-performance flexible asymmetric supercapacitors based on a new graphene foam/carbon nanotube hybrid film. Energy Environ. Sci. **7**, 3709–3719 (2014)
19. X. Wang, Y. Wang, C. Zhao, Y. Zhao, B. Yan, W. Zheng, Electrodeposited $Ni(OH)_2$ nanoflakes on graphite nanosheets prepared by plasma-enhanced chemical vapor deposition for supercapacitor electrode. New J. Chem. **36**, 1902–1906 (2012)

20. Y.-M. Wang, D.-D. Zhao, Y.-Q. Zhao, C.-L. Xu, H.-L. Li, Effect of electrodeposition temperature on the electrochemical performance of a $Ni(OH)_2$ electrode. RSC Adv. **2**, 1074–1082 (2012)
21. N.S. McIntyre, M.G. Cook, X-ray photoelectron studies on some oxides and hydroxides of cobalt, nickel, and copper. Anal. Chem. **47**, 2208–2213 (1975)
22. I.T. Kim, A. Magasinski, K. Jacob, G. Yushin, R. Tannenbaum, Synthesis and electrochemical performance of reduced graphene oxide/maghemite composite anode for lithium ion batteries. Carbon **52**, 56–64 (2013)
23. Y. Xu, G. Jian, Y. Liu, Y. Zhu, M.R. Zachariah, C. Wang, Superior electrochemical performance and structure evolution of mesoporous Fe_2O_3 anodes for lithium-ion batteries. Nano Energy **3**, 26–35 (2014)
24. J. Liu, W. Zhou, L. Lai, H. Yang, S. Hua Lim, Y. Zhen, T. Yu, Z. Shen, J. Lin, Three dimensionals α-Fe2O3/polypyrrole (Ppy) nanoarray as anode for micro lithium ion batteries. Nano Energy **2**, 726–732 (2013)
25. T. Fujii, F.M.F. de Groot, G.A. Sawatzky, F.C. Voogt, T. Hibma, K. Okada, In situ XPS analysis of various iron oxide films grown by NO_2-assisted molecular-beam epitaxy. Phys. Rev. B **59**, 3195–3202 (1999)
26. A.K. Shukla, M.K. Ravikumar, T.S. Balasubramanian, Nickel iron batteries. J. Power Sources **51**, 29–36 (1994)
27. P.V. Kamath, M.F. Ahmed, Cyclic voltammetric studies of nickel-hydroxide and cobalt hydroxide thin-films in alkali and alkaline-earth metal-hydroxides. J. Appl. Electrochem. **23**, 225–230 (1993)
28. D.A. Corrigan, R.M. Bendert, Effect of coprecipitated metal-ions on the electrochemistry of nickel-hydroxide thin-films-cyclic voltammetry in 1 M KOH. J. Electrochem. Soc. **136**, 723–728 (1989)
29. J. Ji, L.L. Zhang, H. Ji, Y. Li, X. Zhao, X. Bai, X. Fan, F. Zhang, R.S. Ruoff, Nanoporous Ni (OH) thin film on 3D ultrathin-graphite foam for asymmetric supercapacitor. ACS Nano **7**, 6237–6243 (2013)
30. L. Bing, Y. Huatang, Z. Yunshi, Z. Zuoxiang, S. Deying, Cyclic voltammetric studies of stabilized α-nickel hydroxide electrode. J. Power Sources **79**, 277–280 (1999)
31. D.M. MacArthur, The proton diffusion coefficient for the nickel hydroxide electrode. J. Electrochem. Soc. **117**, 729–733 (1970)
32. R.S. Schrebler Guzmán, J.R. Vilche, A.J. Arvía, Rate processes related to the hydrated nickel hydroxide electrode in alkaline solutions. J. Electrochem. Soc. **125**, 1578–1587 (1978)
33. J. Come, P.L. Taberna, S. Hamelet, C. Masquelier, P. Simon, Electrochemical kinetic study of $LiFePO_4$ using cavity microelectrode. J. Electrochem. Soc. **158**, A1090–A1093 (2011)
34. V. Augustyn, J. Come, M.A. Lowe, J.W. Kim, P.-L. Taberna, S.H. Tolbert, H.D. Abruna, P. Simon, B. Dunn, High-rate electrochemical energy storage through Li^+ intercalation pseudocapacitance. Nat. Mater. **12**, 518–522 (2013)
35. P. Simon, Y. Gogotsi, B. Dunn, Where do batteries end and supercapacitors begin? Science **343**, 1210–1211 (2014)
36. P. Periasamy, B.R. Babu, S.V. Iyer, Cyclic voltammetric studies of porous iron electrodes in alkaline solutions used for alkaline batteries. J. Power Sources **58**, 35–40 (1996)
37. P. Periasamy, B.R. Babu, S.V. Iyer, Electrochemical behaviour of Teflon-bonded iron oxide electrodes in alkaline solutions. J. Power Sources **63**, 79–85 (1996)
38. G. Huo, X. Lu, Y. Huang, W. Li, G. Liang, Electrochemical performance of α-Fe_2O_3 particles as anode material for aqueous rechargeable batteries. J. Electrochem. Soc. **161**, A1144–A1148 (2014)
39. K. Ujimine, A. Tsutsumi, Electrochemical characteristics of iron carbide as an active material in alkaline batteries. J. Power Sources **160**, 1431–1435 (2006)

40. M. Huang, Y. Zhang, F. Li, L. Zhang, R.S. Ruoff, Z. Wen, Q. Liu, Self-assembly of mesoporous nanotubes assembled from interwoven ultrathin birnessite-type MnO_2 nanosheets for asymmetric supercapacitors. Sci. Rep. **4**, 3878 (2014)
41. J. Liu, M. Chen, L. Zhang, J. Jiang, J. Yan, Y. Huang, J. Lin, H.J. Fan, Z.X. Shen, A flexible alkaline rechargeable Ni/Fe battery based on graphene foam/carbon nanotubes hybrid film. Nano Lett. **14**, 7180–7187 (2014)

Chapter 6
Conclusions, Comments and Future Work

6.1 Conclusions

The synthesis and characterization of low-dimensional carbon materials, including graphene oxide/graphene, graphene foam (GF), GF/carbon nanotubes (CNTs) hybrids, and their composites with nanostructured metal oxides are conducted in this thesis. Their applications in energy storage devices, including lithium-ion battery, aqueous asymmetric supercapacitors and aqueous Ni/Fe battery, are explored.

(1) ***Electrochemical Exfoliation of Graphite***. High-quality graphene flakes is synthesized via a facile electrochemical exfoliation method. The underlying mechanism is discussed in detail. Specifically, electrochemical oxidation reactions triggered by the current flow which removes the electrons from anode may take place, including the anodic oxidation (Eq. 2.1), hydroxylation (Eq. 2.2) and carboxylation (Eq. 2.3) of graphite (as well as water oxidation, Eq. 2.4).

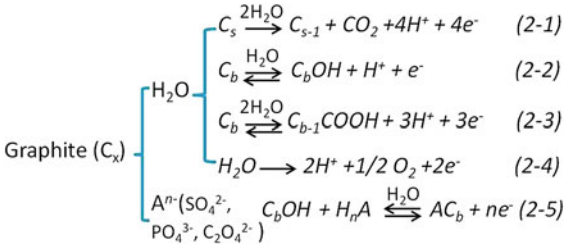

These processes occur initially at surface, grain boundary or structural defect sites, generating ·OH, ·COC, CO·, and COO· functional groups on the graphite surface. CO_2 and O_2 can be produced as the electrolysis products (Eqs. 2.1 and 2.4). Simultaneously, the release of gaseous bubbles was obviously observed during the electrochemical process, and became vigorous with increasing

J. Liu, *Graphene-Based Composites for Electrochemical Energy Storage*,
Springer Theses, DOI 10.1007/978-981-10-3388-9_6

exfoliation time, as if water boiled. The anodic corrosion/etching as well as the violent gas release open up the edge sheets on the graphite rod surface and facilitates the intercalation of bulky anions (as well as their solvated moieties) into the graphite layers, forming graphite-intercalation-compounds (GIC) ($C + A^- \rightarrow CA + e^-$) (Eq. 2.5). The intercalation and the hydrolysis of the intercalated complex ($CA + H_2O \rightarrow COH + H^+ + e^-$) lead to the expansion of graphene sheets and the cleavage/exfoliation of functional graphene sheets.
Various aqueous protonic acids with bulky anions including phosphoric acid, sulfuric acid, oxalic acid, were all proven to be effective during exfoliation process. The diverse choices of aqueous electrolyte provide us with more freedom to adjust the oxidization states of exfoliated graphene and reduce the production cost even further. Our present findings provide deep understanding of the underlying mechanism for electrochemical exfoliation of graphite, effective guides for optimized/controlled synthesis of graphene, and promising approaches for graphene commercialization in future.

(2) ***Design High-Performance GF/Fe_3O_4 composite Anode for Lithium-ion Battery***. GF/Fe_3O_4 hybrid electrodes have been prepare via atomic layer deposition approach. The formed GF/Fe_3O_4 composite exhibits several characteristics: (i) the good electric conductivity and mechanical properties of GF provide efficient ion/electron transportation and mechanical integrity; (ii) the bi-continuous nanostructure Fe_3O_4 formed by interconnected nanoscrystallites are homogeneously distributed on the graphene foam surface with a intact physical contact. The direct contact and interconnection ensure an efficient lithium ion and electron transport between Fe_3O_4 and graphene, as well as ion transport between the electrolyte and the active material. (iii) the binder and conducing agent-free design, as well as atomic layer deposition approach allow a high active material (Fe_3O_4) loading without sacrificing the flexibility of GF/Fe_3O_4 electrodes. Benefiting from the rational design and the unique mesoscale structure, the GF/Fe_3O_4 electrodes display remarkable rate and cycle performance. Our results provide efficient guides for optimized design of flexible electrodes.

(3) ***Design High-Performance Asymmetric Supercapacitors based on GF/CNTs Hybrid Films***. A novel electrode support (GF/CNTs) consisting of carbon nanotubes supported on graphene foam (GF) with covalent bonding has been prepared. The densely grown CNTs extend the 3D architecture of GF without sacrificing the good ohmic and mechanical contact between them, and provide a high surface-to-volume ratio that allows high active materials loading. The GF/CNTs hybrid films show several critical merits, including: (i) good electric conductivity; (ii) large specific surface area; (iii) high active materials mass loading, which could be 4–5 folds higher than pure GF (3–8 mg/cm^2); (iv) Ultrathin and Lightweight with thickness range from 30 to 100 μm; (v) large size, good flexibility and mechanical integrity; and (vi) excellent

electrochemical stability. These features successfully overcome limitation of the insufficient surface area of these graphene/CNTs hybrid films prepared from traditional dip-coating or beam evaporation, and provide GF/CNTs hybrid film with great potential for applications in next-generation flexible energy storage devices. The assembled asymmetric supercapacitors (ASCs) (GF/CNTs/MnO_2// GF/CNTs/Ppy) based on GF/CNTs electrode scaffolds display high energy/power density and are capable of repeated bending without structure failure and degradation in performance. These results presented here would no doubt provide a promising approach for flexible electrode design in future.

(4) ***Design High-Performance Ni/Fe Battery based on GF/CNTs Hybrid Films***. In addition to the development of novel electrode scaffold (Chap. 4), it is equally important to explore the promising applications of traditional energy storage devices in modern energy supply systems. Along this line, the century-old Ni/Fe battery was revisited and re-discovered in this work. By employing $Ni(OH)_2$ nanosheets and porous Fe_2O_3 nanorods grown on light-weight and flexible graphene foam (GF)/carbon nanotubes (CNTs) hybrid films as electrodes, we designed and fabricated a new type of flexible Ni/Fe cell. The assembled f-Ni/Fe cells deliver good electrochemical performance, benefiting from the unique electrode design. Moreover, the f-Ni/Fe cells can retain the electrochemical performance with repeated bendings. These features endow f-Ni/Fe cells a highly promising candidate for next generation flexible energy storage systems.

6.2 Comments and Future Work

6.2.1 Electrochemical Exfoliation of Graphite

Although electrochemical exfoliation of graphite has proved to be an effective method to prepare high-quality graphene flakes in an economical and environmentally-friendly way, several challenges are still remaining to be addressed: (i) the quality of graphene (size, thickness, defects, etc.) is subjected to the raw materials to some extent; (ii) the production is limited to lab-scale at the moment. Therefore, several further justifications are needed: (i) to investigate the effect of raw graphite materials on the quality of resulting graphene in a qualitative way via employing XPS, XRD, Raman spectroscopy and electrochemical characterization methods; (ii) to design and built equipments that are suitable for large-scaled production, optimize the synthesis conditions further, and evaluate the quality of resulting graphene in terms of size and thickness distribution, defects amount and electrochemical performance.

6.2.2 GF and GF/CNTs Hybrid Film Based Flexible Energy Storage Devices

The key challenges for flexible power sources lie in (i) the development of deformable electrodes with high energy density, and (ii) the understanding of underlying mechanism. In this thesis, we have developed a new kind of GF/CNTs hybrid film for flexible electrode scaffolds, and demonstrated its applications in several traditional energy storage systems. Although our designs and results are quite attractive, more research work are required to illustrate the underlying mechanism in a qualitative and quantitative way, and optimize electrochemical performance further.

6.2.2.1 Design Novel GF/CNTs/CNTs Hybrid Films for Flexible Electrode Scaffolds

Our results in Chaps. 3, 4 and 5 indicates that the densely grown CNTs could extend the 3D architecture of GF without sacrificing the good ohmic and mechanical contact between them, which provides a high surface-to-volume ratio that allows high mass loading of active materials. Along this line, we try to design a new kind of GF/CNTs/CNTs hybrid films assisted by ALD method in order to increase the active materials loading further. ALD is a powerful tool to deposit nano-sized catalyst on the surface of GF/CNTs hybrid films, forming GF/CNTs/catalysts composites. The GF/CNTs/CNTs hybrid films is then achieved after the second-growth of CNTs on GF/CNTs/catalysts composites.

6.2.2.2 Explore the Underlying Mechanism of Flexible Energy Systems

The electrochemical properties of active materials (e.g., specific capacity, reversibility, rate capability, cycling behavior, etc.) are strongly dependent on the structure and element changes during electrochemical reaction processes [1–4]. Therefore, the establishment of clear relationships between electrochemical and structural/element data is no doubt one key issue for better understanding and further improving the electrochemical performance of electrode materials.

In situ Raman spectroscopy is a convenient and non-destructive tool for studying electrochemical reaction processes within numerous electrodes in aqueous and non-aqueous energy storage devices [5, 6]. Raman spectroscopy has been found to be very sensitive to the state of metal oxide, with the Raman frequencies being dependent on the metallic oxidization state. Therefore, it is particularly suitable for the investigation of underlying mechanism for redox couples involved in many aqueous electrochemical capacitors, or metal-ion rechargeable batteries. Part of our future work will focus on this area.

References

1. X.H. Liu, J.Y. Huang, In situ TEM electrochemistry of anode materials in lithium ion batteries. Energy Environ. Sci. **4**, 3844–3860 (2011)
2. Q. Su, J. Xie, J. Zhang, Y. Zhong, G. Du, B. Xu, In situ transmission electron microscopy observation of electrochemical behavior of CoS2 in lithium-ion battery. ACS Appl. Mater. Inter. **6**, 3016–3022 (2014)
3. X. Wang, X. Shen, Z. Wang, R. Yu, L. Chen, Atomic-scale clarification of structural transition of MoS2 upon sodium intercalation. ACS Nano. (2014)
4. X.H. Liu, Y. Liu, A. Kushima, S. Zhang, T. Zhu, J. Li, J.Y. Huang, In situ TEM experiments of electrochemical lithiation and delithiation of individual nanostructures. Adv. Energy Mater. **2**, 722–741 (2012)
5. R. Baddour-Hadjean, J.-P. Pereira-Ramos, Raman microspectrometry applied to the study of electrode materials for lithium batteries. Chem. Rev. **110**, 1278–1319 (2010)
6. V. Stancovski, S. Badilescu, In situ Raman spectroscopic-electrochemical studies of lithium-ion battery materials: a historical overview. J. Appl. Electrochem. **44**, 23–43 (2014)